Czech Technical University in Prague
Faculty of Nuclear Sciences and Physical Engineering

DOCTORAL THESIS

Research on cosmic rays on board aircraft using a newly developed PIN diode detector

Prague 2020 Martin Kákona

Bibliografický záznam

Autor	Ing. Martin Kákona, České vysoké učení technické v Praze, Fakulta jaderná a fyzikálně inženýrská, Katedra dozimetrie a aplikace ionizujícího záření

Název práce	Výzkum kosmického záření na palubách letadel za použití nově vyvinutého detektoru s PIN diodou
Studijní program	Aplikace přírodních věd
Studijní obor	Jaderné inženýrství

Školitel	Ing. Ondřej Ploc, Ph.D., Ústav jaderné fyziky Akademie věd České republiky v. v. i., Oddělení dozimetrie záření
Školitel specialista	Ing. Pavel Krist, Ph.D., Ústav jaderné fyziky Akademie věd České republiky v. v. i., Oddělení urychlovačů

Akademický rok	2019 / 2020
Počet stran	146
Klíčová slova	ionizující záření, kosmické záření, směsné radiační pole, dozimetrie směsného radiačního pole, křemíkový diodový detektor, PIN dioda, pevnolátkový detektor ionizujícího záření, dozimetrie na palubách letadel, letecká dozimetrie

Bibliographic Entry

Author	Ing. Martin Kákona, Czech Technical University in Prague, Faculty of Nuclear Sciences and Physical Engineering, Department of Dosimetry and Application of Ionizing Radiation

Title of Dissertation	Research on cosmic rays on board aircraft using a newly developed PIN diode detector
Degree Programme	Applications of Natural Sciences
Field of Study	Nuclear Engineering

Supervisor	Ing. Ondřej Ploc, Ph.D., Nuclear Physics Institute of the Czech Academy of Sciences, Department of Dosimetry
Supervisor specialist	Ing. Pavel Krist, Ph.D., Nuclear Physics Institute of the Czech Academy of Sciences, Department of Accelerators

Academic Year	2019 / 2020
Number of Pages	146
Keywords	Ionizing radiation, cosmic ray, mixed radiation field dosimetry, silicon diode detector, PIN diode, solid-state ionising radiation detector, dosimetry on board aircraft, airborne dosimetry

Acknowledgment

This work is dedicated to my dog Fik, the cleverest dog which attended all the lectures in nuclear physics with me.

My thanks go to the staff of U-120M, Tandetron at the Nuclear Physics Institute of the Czech Academy of Sciences and HIMAC facility at National Institute of Radiological Sciences in Japan for their support of our experiments. Furthermore, I would like to thank Zdeněk Zelenka for giving access to a neutron source, Karel Turek for providing an enriched boron film and Mikhail A. Mikhailov for providing calibrated capacitors and for guiding me through practical detector calibration.

This work was supported by European Structural and Investment Funds project CANAM (CZ.02.1.01/0.0/0.0/16_013/0001812), EU Operational Program Research, Development, and Education project CRREAT (CZ.02.1.01/0.0/0.0/15_003/0000481) and HIMAC project H377. Czech Airlines and Smartwings companies supported measurements on board aircraft.

I would like to thank Iva Ambrožová and Václav Štěpán for their help with the measurements, Petra Lavríková for language corrections, Pavel Krist for listening to my crazy ideas, Ondřej Ploc for protecting me from the daily duties, Karel Kudela for teaching me several data investigation approaches and finally my wife for patience with me and for keeping our home running during my scientific work.

Abstrakt

V této práci je představen nový open source dozimetr AIRDOS postavený na bázi křemíkové PIN diody, který je určen pro měření na palubách letadel. Tento dozimetr má dlouhou výdrž na baterie a nepotřebuje opakovanou kalibraci díky velmi stabilní elektronice. AIRDOS může pracovat nepřetržitě půl roku na baterie a je schopný měřit spektra deponované energie s periodicitou deset sekund. Zároveň je zde prezentován detektor CANDY, který je také vybaven PIN diodou. Na jeho základě jsou zde uvedeny nové poznatky a nové vlastnosti tohoto detektoru. Je zde uvedena inovativní metoda analýzy tvaru pulzu za použití PIN diody s nízkým záporným předpětím. Použití této metody je demonstrováno na praktické realizaci detektoru pro směsné pole, které obsahuje zároveň neutrony a fotony. V práci popsané poznatky ohledně PIN diody umožní vývoj nových detektorů s lepšími vlastnostmi.

Abstract

This work introduces a newly designed open source PIN diode dosimeter AIRDOS intended for measurements on board aircraft. This dosimeter has a long endurance on batteries and its design does not need calibration/recalibration due to very stable front end electronics. AIRDOS can operate for six months on batteries and is capable of measuring spectra of deposited energy with periodicity of ten seconds. Together findings with silicon PIN diode detector CANDY and new properties of this detector are presented. A novel method of pulse-shape analysis of signal with low biased PIN diode is introduced. The use of this method is demonstrated in a practical design of the detector for neutron-photon mixed radiation field. Described findings regarding PIN diode have implications for designs of new featured detectors.

CONTENT

List of Abbreviations

A/D	Analogue to Digital
ADC	A/D Converter
AGP	Malaga Airport
BT	Battery
C	Capacitor
C-V	Capacity - Voltage
CARI	A computer program developed at Civil Aerospace Medical Institute
CANAM	Center of Accelerators and Nuclear Analytical Methods
CERF	CERN-EU high energy Reference Field facility
CME	Coronal Mass Ejection
CR10	Database of measurements of Cosmic Rays above 10 km above sea level
CRREAT	Center of Cosmic Rays and Radiation Events in the Atmosphere
D	Diode
DC	Direct Current
EA	Etalon of Activity
EEPROM	Electrically Erasable Programmable Read-Only Memory
EPCARD	European Program package for the Calculation of Aviation Route Doses
FD	Forbush Decrease
FWHM	Full Width at Half Maximum
GCR	Galactic Cosmic Rays
GLE	Ground Level Enhancement
GNU	GNU's Not Unix!
GPL	General Public License

GPS	Global Positioning System
HDPE	High Density PolyEthylene
HIMAC	Heavy Ion Medical Accelerator in Chiba
ICRP	International Commission on Radiological Protection
ICRU	International Commission on Radiation Units and Measurements
ISO	International Organization for Standardization
ISS	International Space Station
LET	Linear Energy Transfer
MCNPX	Monte Carlo N-Particle eXtended
MDU	Mobile Dosimetry Unit
MLAB	Modular Laboratory Open Hardware Project
NMDB	Neutron Monitor DataBase
PCB	Printed Circuits Board
PIN	A semiconductor device with Positive, Intrinsic and Negative layers
PMMA	Polymethyl methacrylate
PN	A semiconductor device with Positive and Negative layers
PPM	Parts Per Million
PRG	Prague Airport
R	Resistor
RTC	Real Time Clock
SD card	Secure Digital Memory Card
SEP	Solar Energetic Particles
SRIM	Stopping and Range of Ions in Matter
TED	Track Etch Detector

TEPC	Tissue-Equivalent Proportional Counter
TLD	ThermoLuminescent Dosimeter
UART	Universal Asynchronous Receiver/Transmitter
UTC	Coordinated Universal Time
µC	Microcomputer

1. Introduction

1.1. Plot of this dissertation work

This work follows the main goals stated below after a brief introduction to cosmic ray measurement on board aircraft and introduction to PIN diode detectors with a description of the motivation for this work. The chapters that follow focus on the evaluation of historical data, development of new dosimeters and looking for some improvements of PIN diode detectors. Evaluation of historical data is not fully described in this work and chapters concerning this topic mainly refer to the author's publications in this field. Major attention of the thesis is paid to detectors with PIN diodes and issues around them. Finally, some methods for improvements of PIN diode detectors are described.

1.2. Cosmic rays and ionizing radiation on board aircraft

Earth's atmosphere is permanently penetrated by cosmic rays. There are two components of primary cosmic rays - GCR (Galactic Cosmic Rays) and solar wind. 98 % of GCR is made up of nuclei of well-known atoms without electrons and the remaining 2 % are solitary electrons. 87 % of nuclei are protons, 12 % helium ions and 1 % heavier ions (Reitz 1993; Simpson 1983). The solar wind mostly consists of protons with an equal number of electrons (Reitz 1993; Evenson et al. 1981). Primary cosmic rays interact with the atmosphere in altitudes from tens of kilometers up to ones of kilometers and produce secondary cosmic rays. These secondary cosmic rays are mainly responsible for radiation exposure of aircrew and must be considered for radiation protection. The ionizing radiation field on board aircraft contains different types of particles possessing a wide range of energies (Roesler et al. 1998). The contribution to an ambient dose equivalent[1] from individual particle types on board aircraft is as follows: 50 % from neutrons, 15 % from protons, 20 % from electrons and positrons, 10 % from photons and 5 % from muons according to the ICRU (International Commission on Radiation Units and Measurements) (ICRU 2010a).

A flux of the GCR can be considered as constant but the solar wind is strongly dependent on Sun's state and can modulate GCR and Earth's magnetic field. This modulation can produce sudden changes in cosmic ray flux and produces phenomena like GLE (Ground Level Enhancement) (Firoz et al. 2010; Poluianov et al. 2017; Forbush et al. 1993), FD (Forbush Decrease) (Forbush 1993) and other fluctuations of secondary cosmic rays. Many of these fluctuations originate (at the state of knowledge) in unpredictable events like CME (Coronal Mass Ejections) and SEP (Solar Energetic Particles). So far, the modeling of ionizing radiation on board aircraft reveals that a single event can increase a dose significantly (Dyer et al. 2007) and that validation of the models with empirical data is necessary (Tobiska et al. 2015).

[1] Ambient dose equivalent (H*(10)) is the dose equivalent at a point in a radiation field that would be produced by the corresponding expanded and aligned field in the ICRU sphere at a depth of 10 mm on the radius vector opposing the direction of the aligned field.

1.3. Motivation for this work

Secondary cosmic rays are continually monitored by neutron monitors at ground-based stations around the world (Kudela and Langer 2009; NMDB 2020). During more than 60 years of monitoring, these instruments have provided evidence of many phenomena (GLE, FD, SEP,...). Other phenomena studied in recent years are connected with high energy atmospheric processes like lightning and generally electrification of the atmosphere (Dwyer and Uman 2014; Enoto et al. 2017; Chilingarian 2014). Some phenomena could be attenuated by a thick layer of the atmosphere. The initial idea of this work was a utilisation of a huge number of aircraft flying every day in altitudes above 10 km. These flights cover almost the whole Earth all the time. An appropriate detector deployed on board aircraft can measure cosmic rays before major attenuation in the atmosphere or other energetic phenomena producing ionising radiation in the atmosphere. For widespread deployment of such an instrument, a lightweight, cheap and battery operated detector with low power consumption is needed.

Many groups worldwide provide measurements on board aircraft (Lillhök et al. 2007; Tobiska et al. 2016; Meier and Matthiä 2019; Lindborg et al. 2007; Bottollier-Depois et al. 2004) However, there are no publicly available design principles of the instruments they use. Therefore we can only hardly compare their results.

Since 2001, our group performs routine measurements of ionising radiation on board aircraft by Liulin dosimeter (Ploc et al. 2013). The measurements continue up to recent days, see figure 1 and figure 2 for updated flight routes. These measurements were compared with measurements of secondary cosmic rays performed on the ground by neutron monitors (Kákona et al. 2016) and with model of distribution of secondary cosmic rays CARI (Copeland et al. 2017) which is used for estimation of aircrew doses in our country (Kubančák et al. 2019).

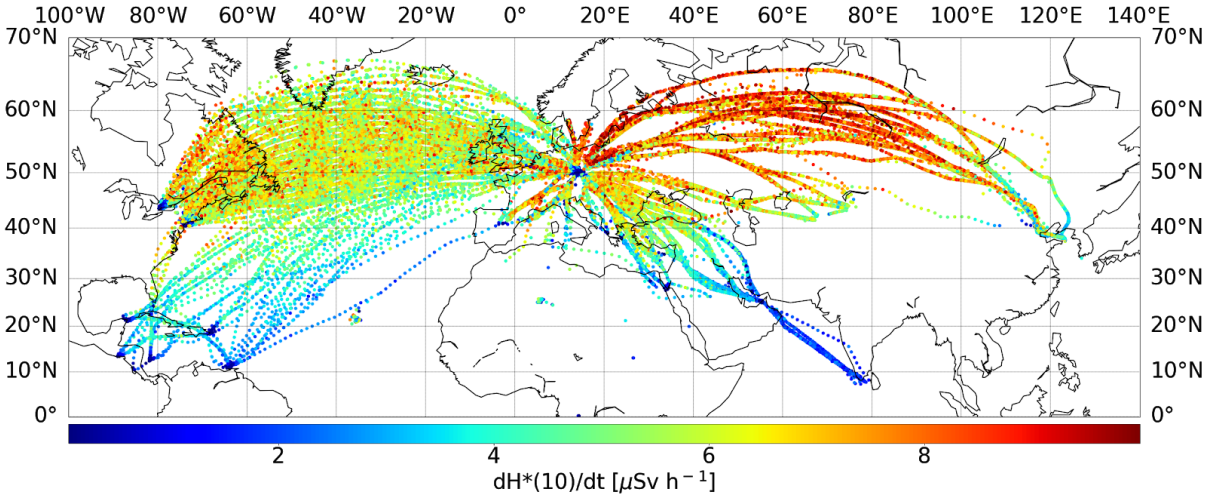

Figure 1*: Long term measurements performed by Liulin dosimeter on board aircraft since 2001. Scatter plot of an ambient dose equivalent depending on geographical position. The data are taken from (Kákona, Kyselová, et al. 2019).*

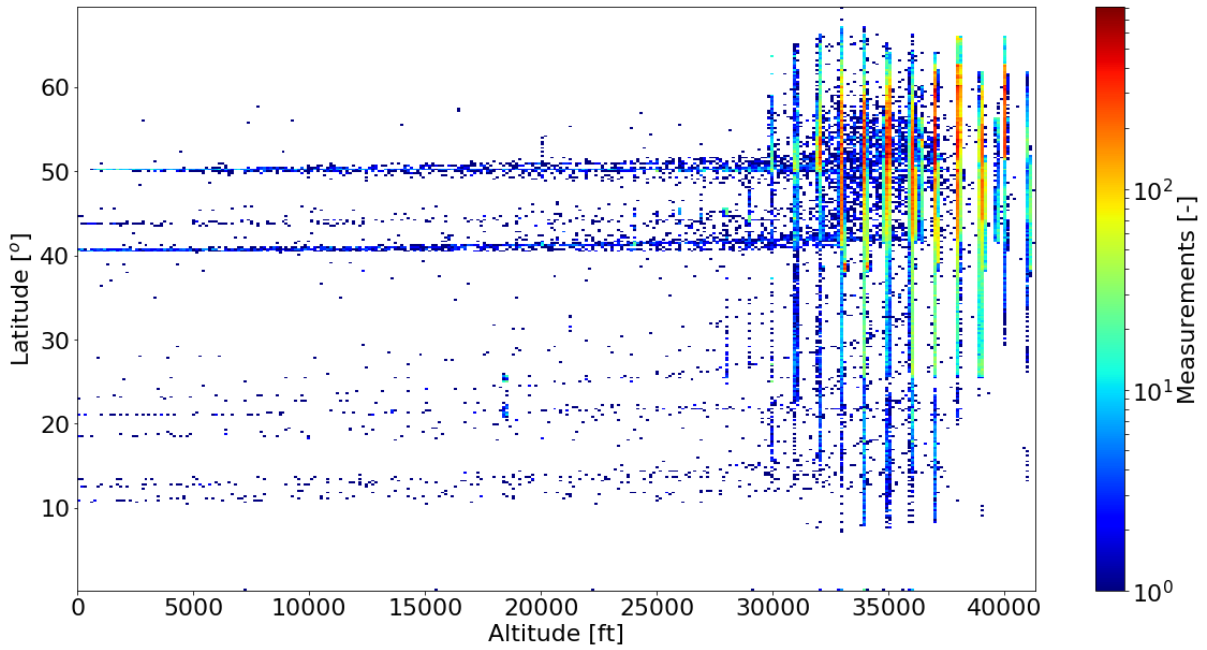

Figure 2*: Long term measurements performed by Liulin dosimeter on board aircraft since 2001. Histogram of flight levels and latitudes. The data are taken from (Kákona, Kyselová, et al. 2019).*

We identified some discrepancies in our long term measurements by Liulin dosimeter. These discrepancies which are characterised in chapter 3.3. Discrepancies in old measurements led us to develop a new dosimeter with fully described design. Our motivation was to better understand the measurement mechanisms of silicon diode detector. Our aim was to introduce an open source fully documented design which can be used as a base platform for future investigation, improvements and modifications for desired deployment. This dosimeter (AIRDOS) has comparable properties as Liulin dosimeter, which enables continuation of our long term measurement on board aircraft.

I discuss in this work whether it is feasible to better characterise quantitatively or qualitatively the radiation field on board aircraft with a usage of a single PIN diode as a sensor. New findings discovered during the design of the new dosimeter and measurements performed with this dosimeter are also presented.

1.4. Airborne dosimeters

1.4.1. Liulin

This work documents investigation into the design and radiation response of solid state radiation detectors based on a single silicon diode. An example of this detector which has found widespread use for measurement of ionizing radiation on board aircraft (Spurný and Dachev 2003; Meier et al. 2016) is the Liulin dosimeter (Dachev et al. 2001). This detector is based on a silicon PIN diode with an area of 2 cm^2 and a thickness of 300 μm. Figure 3 shows

a block diagram of the internal components of this detector (Dachev et al. 2001) and a typical outfit and detector and deployment on board aircraft is shown in figure 4.

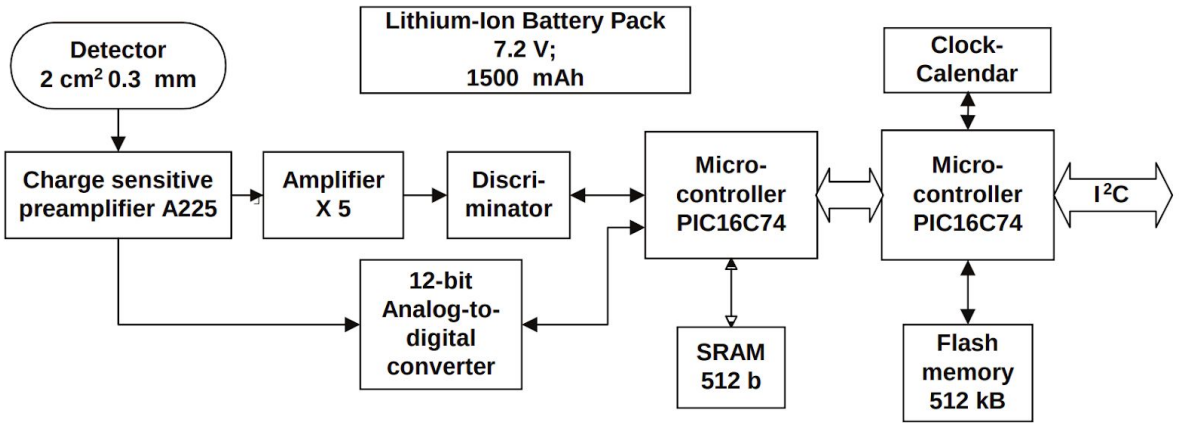

Figure 3*: Block diagram of the Liulin dosimeter. This picture was taken from (Uchihori et al. 2002) .*

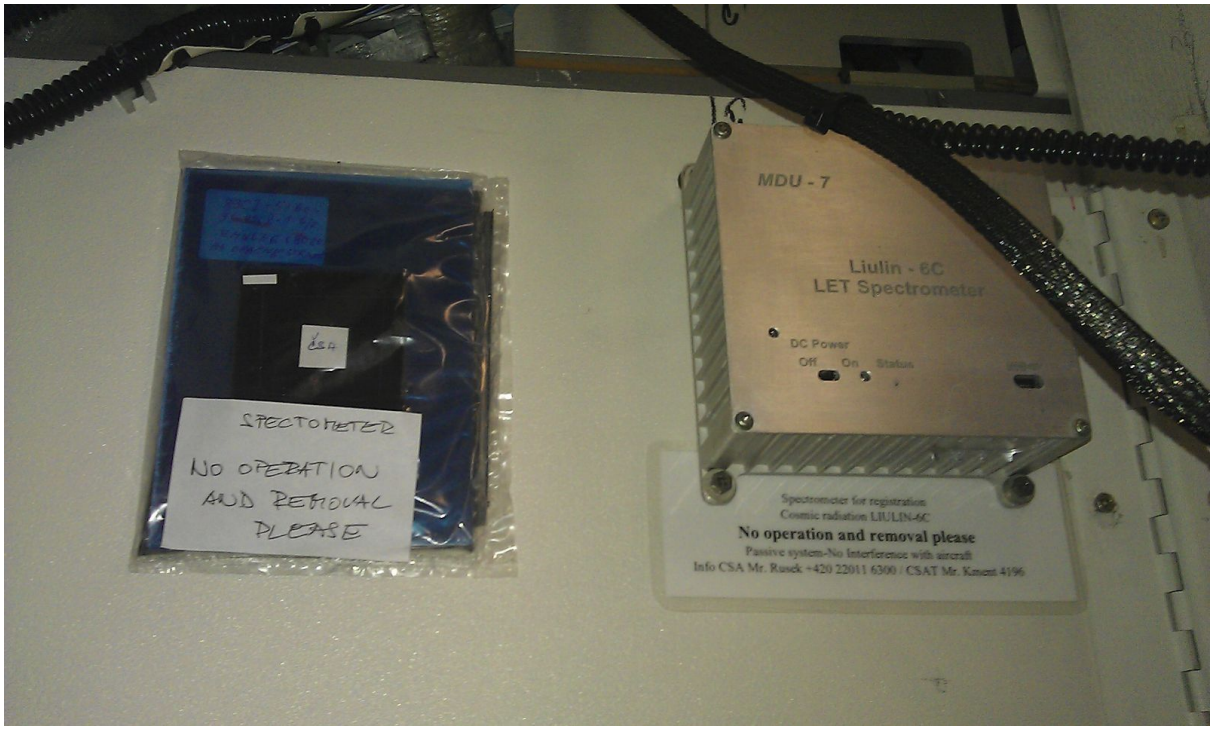

Figure 4*: Liulin dosimeter (right side) deployed on board aircraft together with nuclear emulsions and TLDs (ThermoLuminescent Dosimeters) (left side). Courtesy of Czech Airlines.*

Parameters of the Liulin dosimeter declared in the datasheet (Dachev et al. 2009) are summarized in table 1. Liulin provides dose rates in silicon with tens of seconds resolution.

Table 1*: Parameters of Liulin 6C MDU dosimeter as declared in datasheet.*

Dimensions	110 x 100 x 45 mm^3
Weight	570 g
Energy range	from 0.04 to 20.8 MeV
Number of channels	256
Channel width	81.4 keV
Exposition time	10, 20, 30, 60, 120, 240, 300 s
Continuous measurement (with 300 s period)	3 months
PIN diode type	Hamamatsu S2744-08
Battery	2x LS 33600
Flash memory	1 GiB

1.4.2. HAWK

HAWK FW-AD1 is a sample of TEPC (Tissue-Equivalent Proportional Counter) dosimeter. This dosimeter is intended for measurement in mixed radiation fields. As can be seen from parameters in table 2 (Far West Technology, Inc. 2010), this device can not be used for routine measurement on board aircraft due to big dimensions and low endurance of its batteries. However, this device is suitable for reference dosimetry (Lindborg et al. 1999). HAWK measures lineal energy spectra in tissue-equivalent material with minute resolution.

Table 2*: Parameters of HAWK TEPC FW-AD1 as declared in datasheet.*

Dimensions	160 mm dia x 340 mm
Weight	5 kg
Lineal energy range	0 - 25.6 and 0 - 1024 keV/µm
Number of channels	256 / 1024
Deadtime	64 ms
Continuous measurement	50 hours
Sensor type	125 mm dia spherical tissue equivalent proportional counter, Benjamin type, 2.1 mm plastic A150, propane 7 torr
Battery	4x D cells
Flash memory	Compact Flash Card

1.4.3. Passive dosimeters

Many types of passive dosimeters can be used for mixed radiation fields as well. Because this work focuses on measurement of short term fluctuations (lasting from seconds to days) in the secondary cosmic rays we can omit this group of dosimeters here. However, some results obtained by Liulin were checked against TLD's (Thermo-Luminiscent Detectors) and TED's (Track Etch Detectors) (Spurný et al. 2007; Spurný et al. 2009).

1.4.4. Programs for calculation of effective dose

By a recommendation of the authorities (ICRP 1997; ICRU 2010b) a calculation of effective dose rate, as a function of geographic location, altitude and solar cycle phase, and folding these values with flight and staff roster information to obtain estimates of effective doses[2] for individuals is a preferred approach (ISO 2015). There are programs available that do such calculations - for example CARI (Copeland et al. 2017; Copeland 2017) and EPCARD (Mares et al. 2009) are widely used.

[2] The effective dose (E) is a tissue-weighted sum of the equivalent doses in all specified tissues and organs of the body. Equivalent dose (H) is a dose quantity representing the stochastic health effects of low levels of ionizing radiation on the human body which represents the probability of radiation-induced cancer and genetic damage.

1.5. Silicon PIN diode detectors

1.5.1. Structure of PIN diode

Silicon PIN diode is a semiconductor structure with three layers - heavily doped p^+ and n^+ layers and i layer from intrinsic silicon. Practically, the intrinsic region is manufactured from very lightly doped n^- silicon. This diode is operated with reverse bias voltage as we can see in figure 5. An advantage of this diode is a wide thickness of depleted region (sensitive volume) stretching over the i region and slightly beyond it.

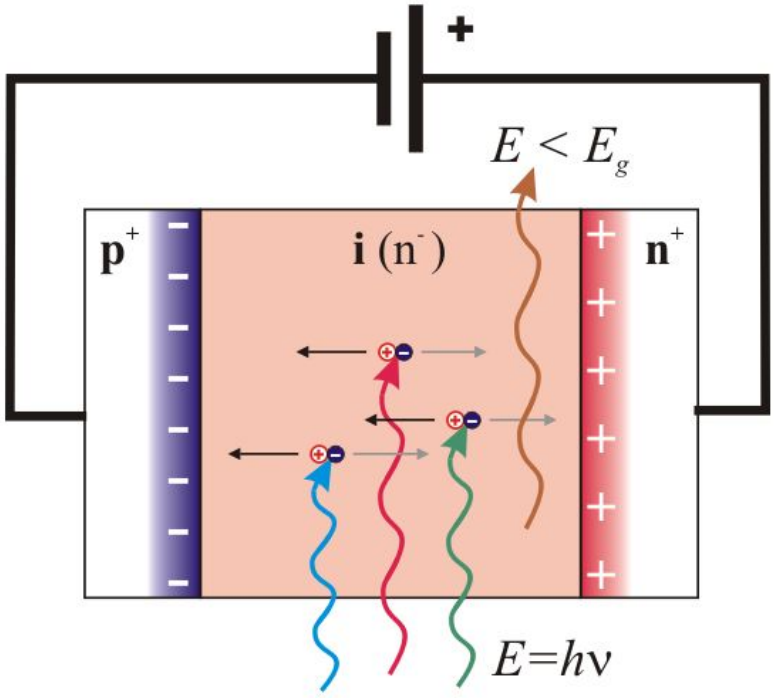

Figure 5*: Structure and principle of ionising particle detection with reverse biased PIN diode. Picture taken from (Lappetito 2017) .*

PIN diodes with relatively large areas are available commercially as photodiodes. Sample of diodes used in this work are S2744 (manufactured by Hamamatsu) and BPW34 (many manufacturers).

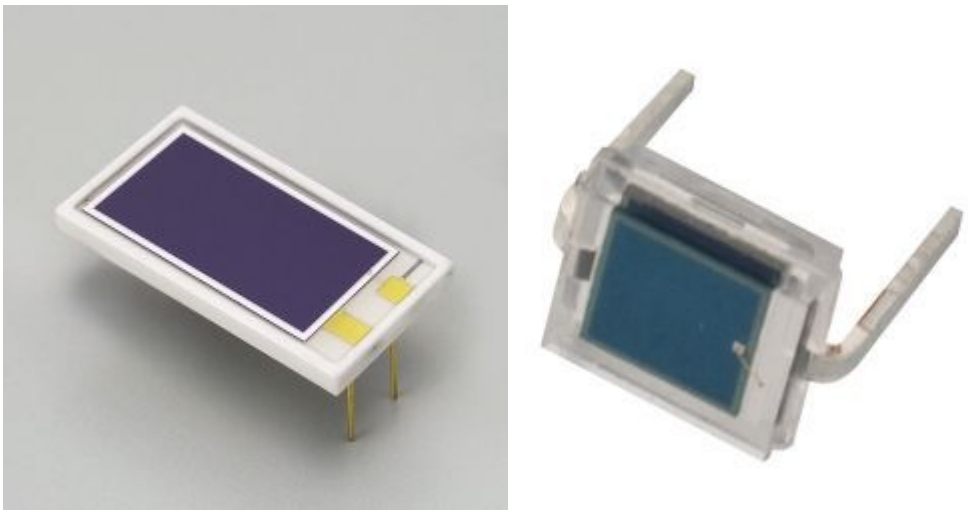

Figure 6*: Samples of PIN photodiodes. S2744 (HAMAMATSU 2011) on the left side and BPW34 (Vishay 2019) on the right side.*

1.5.2. Properties of PIN diodes

Thickness of depletion region is an important parameter of diodes if we are thinking about ionising radiation detection because we can detect ionisation mostly in depleted region. Second important parameter is the capacity of the diode, because the capacity in an input of frontend electronics increases input noise. Designers usually increase reverse bias voltage as high as possible slightly below breakdown of PN junction. Later we show that this is not necessary. There is C-V characteristics of S2744 PIN diode shown in figure 7. Many designers use 70 V as reverse bias voltage for this diode because of the lowest capacity. Maximum reverse voltage for S2744 is 100 V. Please note, that graph in figure 7 is measured with DC reverse voltage with 1 MHz AC component.

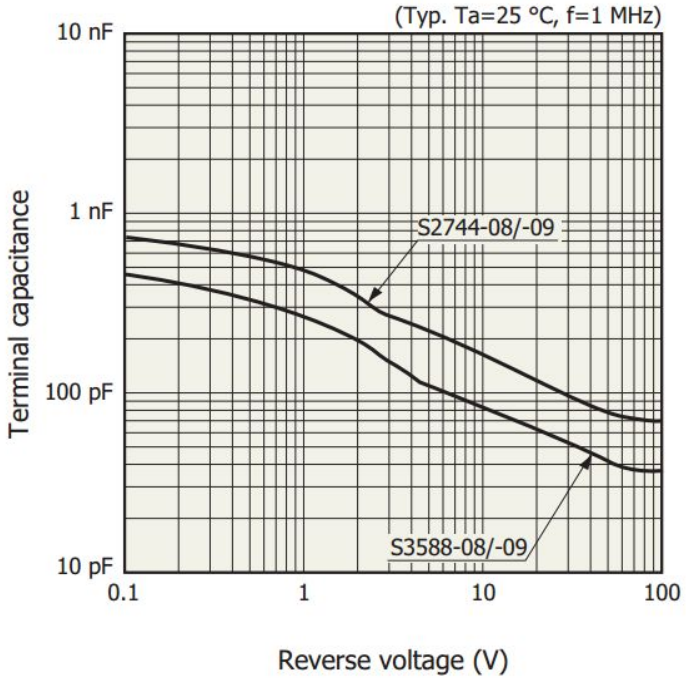

Figure 7*: Measured relation between Capacitance and Reverse Bias voltage taken from Hamamatsu datasheet.*

PIN diode has a limited ability in charged particle characterisation (Ammerlaan et al. 1963). It is done by limited velocity of charge carriers in an electric field formed in the intrinsic region of the diode. Drift velocity v_d of charge carriers is

$$v_d = \mu E ,$$

where μ is charge carrier mobility (1400 $cm^2 / V^{-1} s^{-1}$ for electrons and 450 $cm^2 / V^{-1} s^{-1}$ for holes in silicon at room temperature) and E is intensity of electric field in V cm^{-1}. Please note that the hole traverse 300 um of depleted region of the S2744 PIN diode in 1 us for reverse bias voltage 2 V. Compare this information with measurement frequency in figure 7.

1.5.3. Silicon PIN diode as ionising radiation detector

An important parameter for PIN diode as a particle detector is the energy necessary for electron-hole pair creation. It is experimentally observed that the energy required to form the electron-hole pair exceeds the bandgap about three times. It is the result of energy and momentum conservation (Alig and Bloom 1975). Mean energy for electron-hole creation is about 3.65 eV in silicon.

We have taken into account practical limitations of used silicon diode detector. Figure 8 illustrates the range of different types of charged particles in silicon. Practical designs with large area diodes are able to detect minimally tens of thousands of electrons. This limits the sensitivity from 200 keV approximately. We can conclude from figure 8 that a 300 μm thin detector is capable of capturing almost no electrons with full energy and only a very limited

range of energies of protons (up to 6 MeV). From all the other particles and energies the sensor is capable of capturing only a fragment of their energy. The situation is similar with photons because they are represented by recoiling electrons.

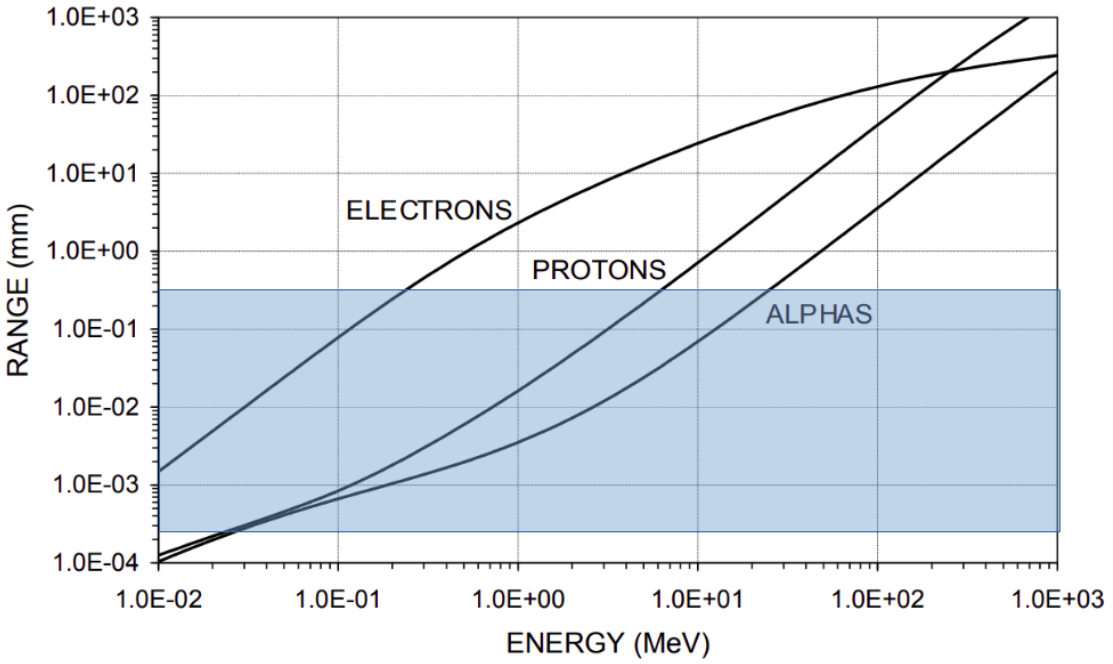

Figure 8*: Range of different ionising radiation particles in silicon. Grayed region represents particles incident perpendicularly to the detector and deposit full energy in silicon diode with 300 µm depleted region. Graph of ranges of particles in silicon is reprinted from (Spieler 2012)*

.

1.5.4. Analog front-end electronics

Charge dissipated in silicon diode detector by ionizing radiation has to be collected and transferred to measure quantities like current or voltage. It is obviously done by a transimpedance/charge amplifier (figure 9) (Keim 2018).

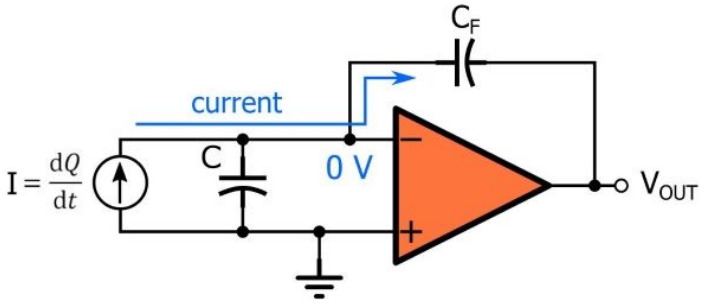

Figure 9*: Charge amplifier (Keim 2018).*

This circuit can convert charge to voltage according to

$$V_{OUT} = \frac{1}{C_F} \int -I\, dt = -\frac{Q}{C_F}\,.$$

Amplifier has a gain

$$A_Q = \frac{dV_{OUT}}{dQ} \approx \frac{1}{C_F}\,.$$

However, the circuit in figure 9 is impractical due to amplification of offset current flowing into the input of an operational amplifier. The resistor parallel to the feedback capacitor C_F has to be connected (figure 10) for discharging the C_F.

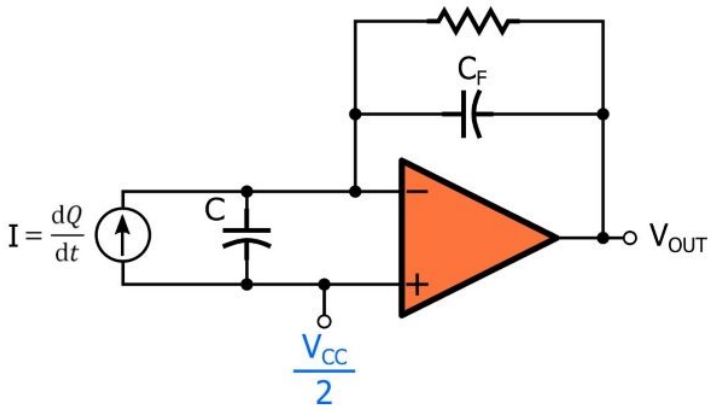

Figure 10*: Practical arrangement of charge amplifier (Keim 2018).*

2. Main goals of this work

Three main goals were defined for this work:

I. Assess an influence of short term solar activity on intensity of secondary cosmic rays using a comparison of historical data measured on board aircraft and neutron monitors data measured on the ground.

II. Develop and evaluate a dosimeter based on a PIN diode detector suitable for measurement in mixed radiation field on board aircraft.

III. Find a method that improves the current characterization of mixed radiation field on board aircraft using the PIN diode detector.

3. Evaluation of historical data

The main goal of this section was an assessment of the relationship between a dose measured on board aircraft, models and ground based measurements performed by neutron monitors. There is a potential for refining models of ionising radiation on board aircraft.

3.1. CR10 database

For an evaluation of historical airborne data obtained by our research group (Spurný and Dachev 2003), a database CR10 of measurements obtained by Liulin dosimeter (Dachev et al. 1989) on board aircraft has been established. My contribution involved programming the database and programming scripts for data evaluation from the database. An example of data evaluation is finding of the FD (Forbush Decrease) in data (figure 12) by newly developed scripts. The database was introduced in paper (Kákona, Kyselová, et al. 2019).

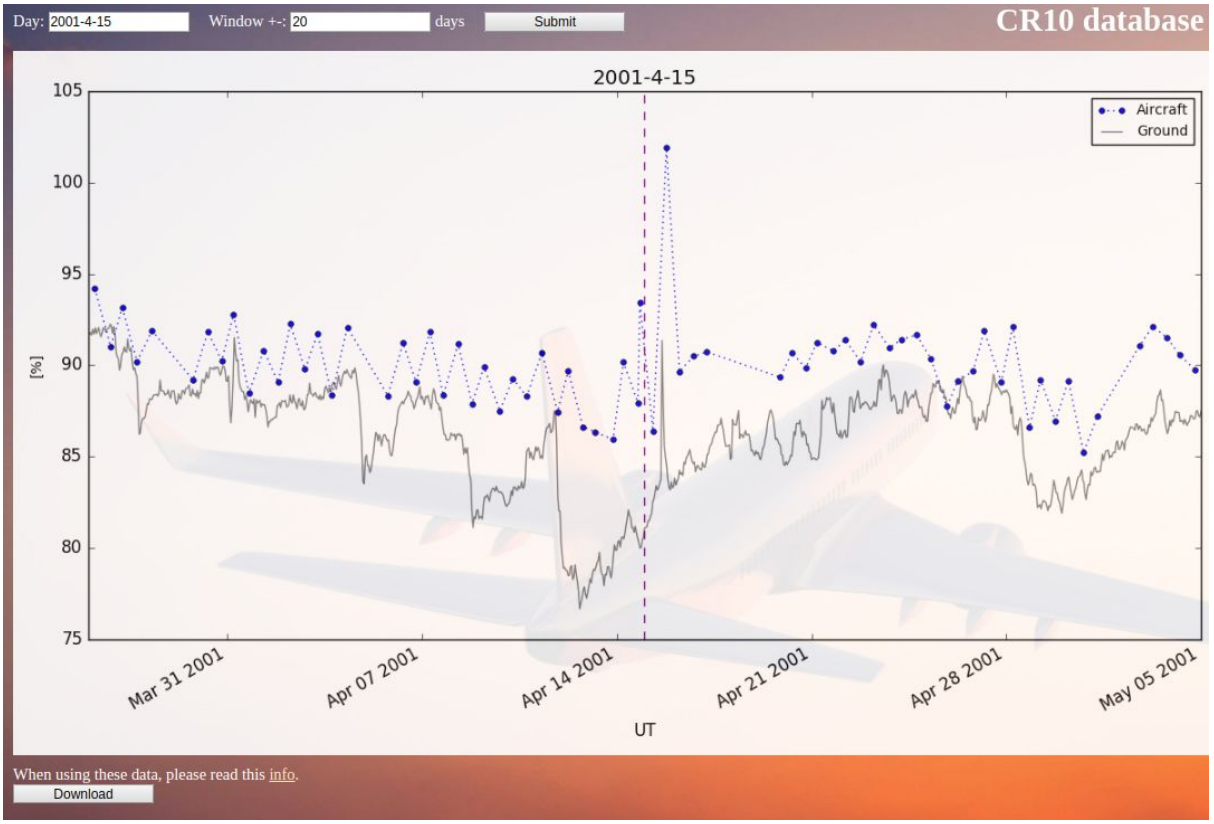

Figure 11*: CR10 database user interface with depicted GLE.*

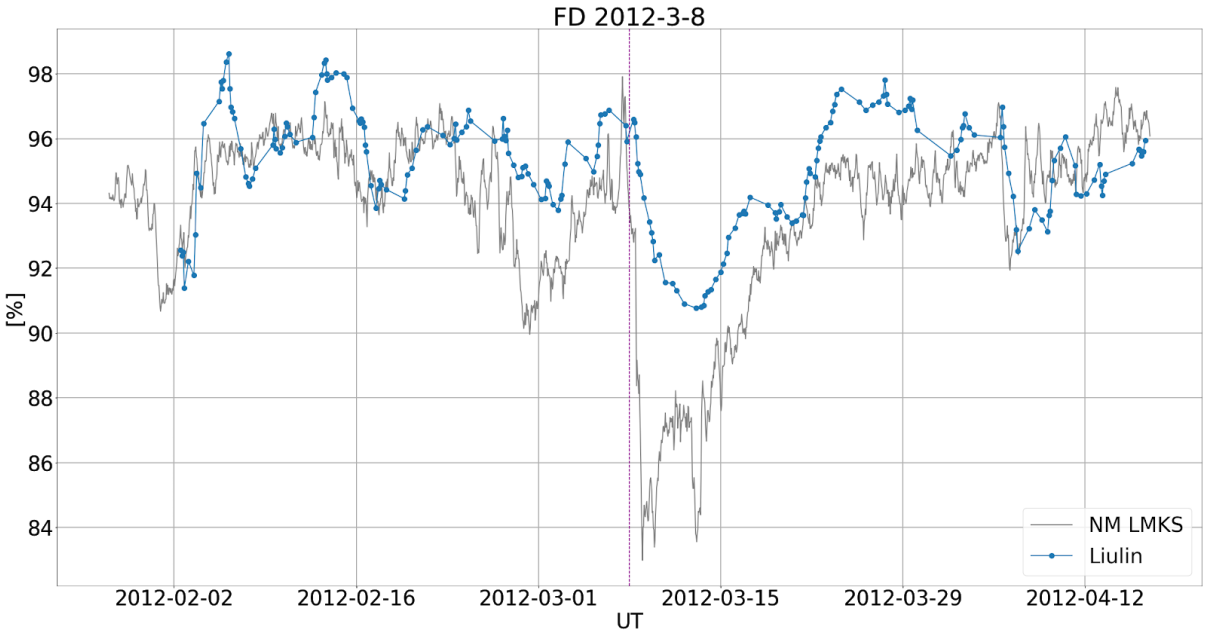

Figure 12*: FD (Forbush decrease) on 8th March 2012 depicted by data evaluation scripts from CR10.*

3.2. Comparison of airborne data with neutron monitor data

For evaluation of historical data in CR10 database, a comparison of airborne data with other methods of measurement and assessment of the relevance of airborne measurements was performed. This assessment was done by (Kákona et al. 2016). Randomly, four months of measurements were selected (about 7300 values from on board measurements). First, the data from the model, from Liulin measurements and from a neutron monitor were recalculated for different geomagnetic positions of aircraft and then a comparison of fits was performed. We showed that our airborne data are in correlation with the ground based measurements provided by neutron monitor and reflects variations in solar activity. Due to discrepancies in the historical data mentioned in the next chapter we realised that more statistics is necessary for compensation of errors of measurement. More dosimeters flying simultaneously are needed. It motivated us for a development of a new open source dosimeter which is described in this work.

3.3. Discrepancies in previous measurements

During our measurements with Liulin dosimeters, some discrepancies were observed. There were not fully explained quantities in the first energy channels (figure 13) and there are changes in response during long time usage of Liulin dosimeter (figure 14). Both these phenomena could be explained with our experiences from design of AIRDOS dosimeter (the design of AIRDOS is described further in this work). A comparison of AIRDOS and Liulin dosimeters was done in publication (Kákona, Štěpán, et al. 2019). Differences in results AIRDOS and Liulin showed that the origin of the peak in Liulin's channel 3 is in electronics of Liulin - not in nature. Most likely explanation of this peak comes from understanding of the block schematics of Liulin dosimeter figure 3. There is a discriminator/comparator used in the Liulin circuit. The key issue is generating a reference voltage for comparison with a signal from

ionizing radiation. With usage of some back-engineering, a resistive trimmer for setting reference voltage was discovered in the Liulin electronics. Mechanical stability and presetting of this trimmer has a major influence on the size of the peak in channel 3 and values in channels 2 and 1. AIRDOS dosimeter does not suffer for this because AIRDOS design does not use discriminator for starting A/D conversion and converts signal continuously. Discrimination of noise is done in postprocessing of AIRDOS's data not in electronics as is done by Liulin.

Described findings are important for assessing the dose because events in first channels (with energy deposition from 200 to 400 keV) contributed more than 30 % of the deposited energy in the field on board aircraft. As noted by (Dachev et al. 2002), moving the spectrum one channel left or right can result in a ±40% difference in dose.

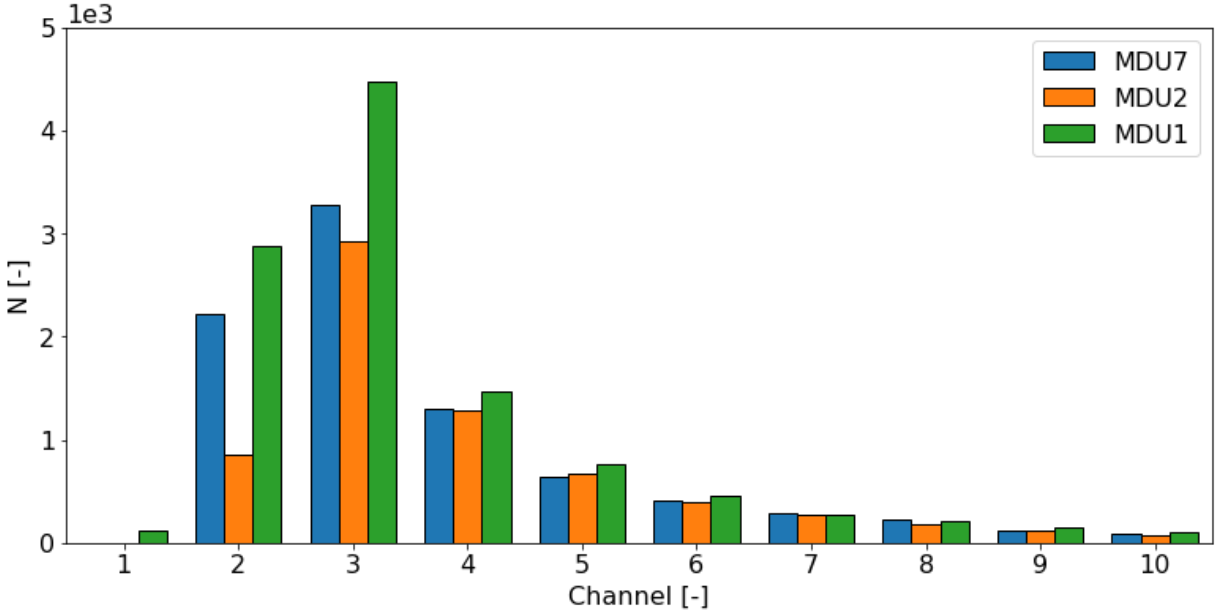

Figure 13*: Comparison of spectra from three Liulin MDUs measured during one flight from Prague to Barcelona (measurement campaign of our group on December 10, 2015). We can see big differences in the first three channels.*

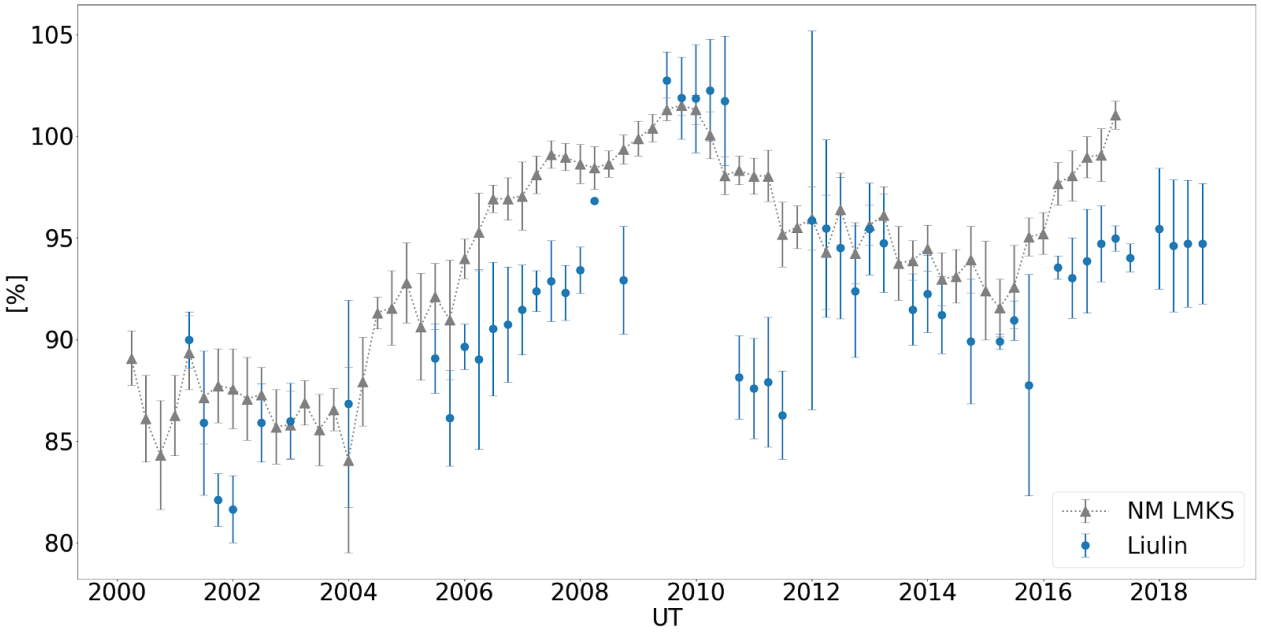

Figure 14*: Long term measurement with Liulin dosimeter on board aircraft and comparison with Neutron Monitor data from Lomnický Štít. Whole solar cycle is depicted here. We can see discrepancy in data in the year 2011. There is a relative flux at the y axis displayed in percent scale. For the neutron monitor data, the percentages are normalized to 100% level reached in September 1986 and represented by 1 745 200 counts per hour. For the Liulin data, 100% is 1.55 particles per square centimeter per second. Data are taken from (Kákona, Kyselová, et al. 2019).*

3.4. Results of evaluation of historical data

Evaluation of historical data showed us that measurement on board aircraft is feasible and obtained data can follow a modulation of secondary cosmic rays. Nevertheless, some discrepancies and issues with measurement method and some issues with used dosimeter devices were discovered. These results directed us to a development of a new fully documented device with fully documented measurement method and new scripts for calculation of an ambient dose equivalent rate from measured data was programmed. All that work was done by the author of this thesis. Design of the new dosimeter is described in the next chapter and a sample of scripts is an attachment of this work.

4. AIRDOS dosimeter

Two new open source airborne dosimeters were developed by the author of this thesis (AIRDOS 01 and AIRDOS 02). Manufacturing documentation, firmware documentation and scripts for data evaluation for these dosimeters are publicly available at GitHub server (Kákona et al. 2017; Kákona and Chroust 2018a). Only the most advanced version of AIRDOS 02 is described in this work.

The AIRDOS is intended for measurements in low intensity mixed ionizing radiation fields. In its aircraft version, it houses a silicon PIN diode as a radiation detector, an electronics for conversion of the signal to the pulse-height spectra, a GPS module (optional), a datalogger, a memory card and batteries for up to six months of operation. It is a portable device for routine measurements on board aircraft. This design is built on an Open Hardware modular platform MLAB, the firmware is written in Open Software platform Processing and data processing is written in Python using Open Software scientific libraries.

4.1. AIRDOS design

4.1.1. Hardware design

AIRDOS is a low power, battery operated, absorbed dose in silicon spectrometer. It contains a silicon PIN diode (Hamamatsu S2744-09) as a sensor, analog signal processing and acquisition unit with datalogger. Optionally, a GPS (Global Positioning System) receiver is mounted. Two LS33600 (Li-$SOCl_2$) cells are used as a power source. Endurance of measurement is six months without GPS and one month with GPS. The data are stored on an SD card (Secure Digital Memory Card). Block schematic of AIRDOS is depicted in figure 15 and a typical outfit with an aluminium case is shown in figure 16. Electronics is divided into two, respectively three PCB's (Printed Circuits Boards): analog electronics (PCRD04B), the GPS receiver (GPS01B) and a datalogger (DATALOGGER01A). See figure 17. The dosimeter modules have become a part of an Open Hardware project MLAB (MLAB 2003). All modules are available under GNU General Public License v3.0 (GNU 2007). The modularity of AIRDOS allows further development, easy adding of new features, easy adding of new sensors and a cooperation with the open hardware project.

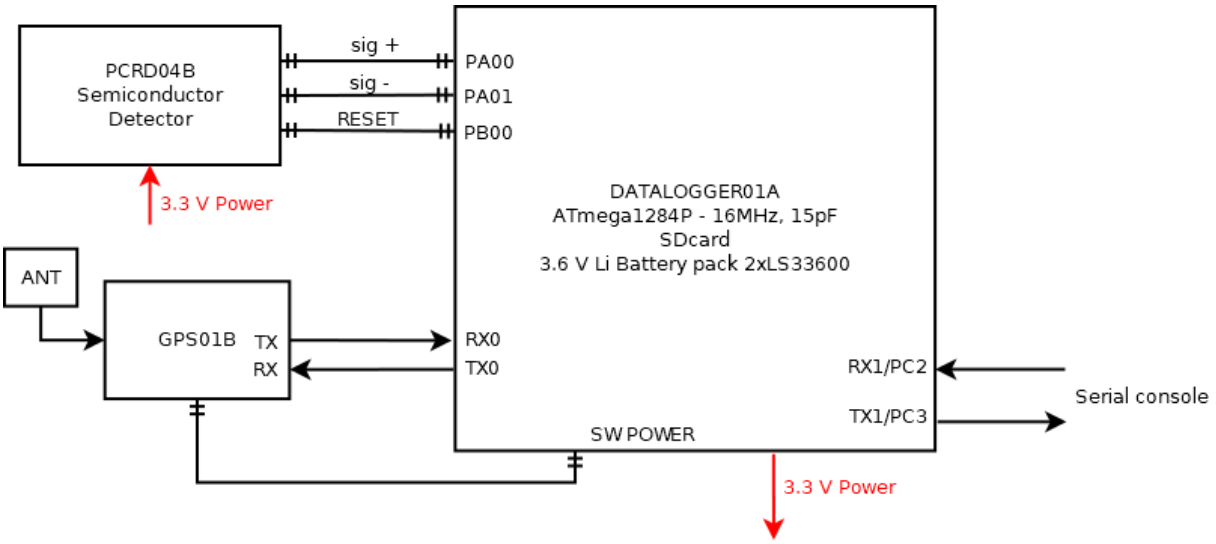

Figure 15*: Block diagram of AIRDOS 02.*

Figure 16*: Outfit of AIRDOS 02 dosimeter.*

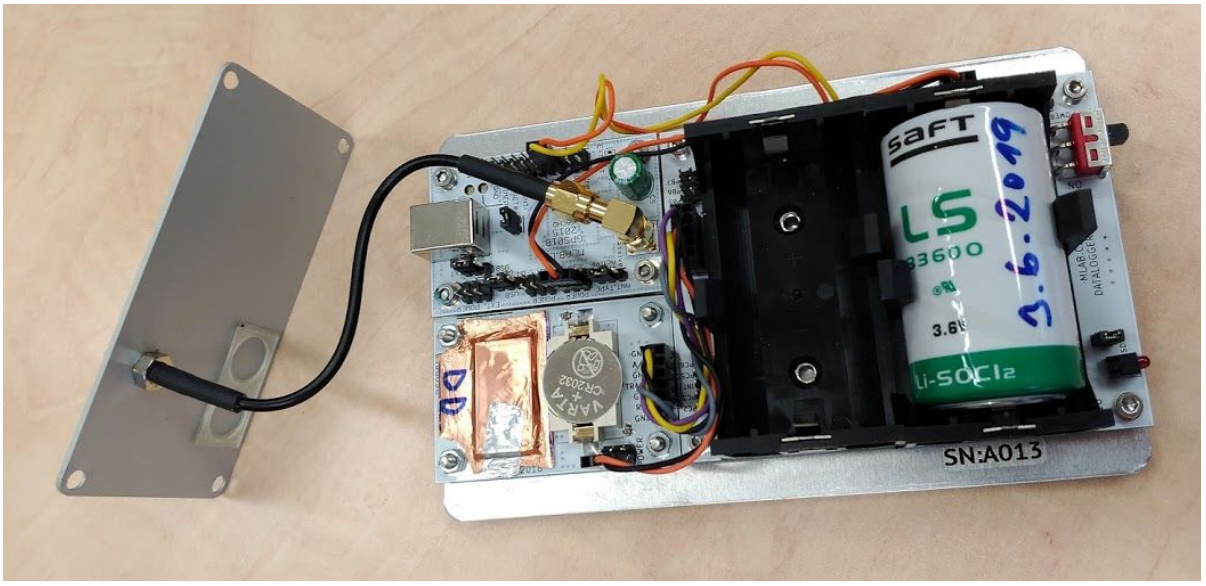

Figure 17*: Deployment of PCB's inside the AIRDOS 02 dosimeter. Left up is the GPS module. Left down is the analog frontend with a PIN diode sensor and a V_{bias} battery CR2032.*

4.1.2. Analog circuit design

All analog circuits are implemented on PCB (Printed Circuits Board) PCRD04B. Manufacturing documentation for this module is available on-line (Kákona 2018b).

Silicon PIN photodiode (D2) is connected to a trans-impedance amplifier (figure 18) and is negatively biased by lithium cell CR2032 (BT1) with 3 V against the reference voltage REF 1.2 V.

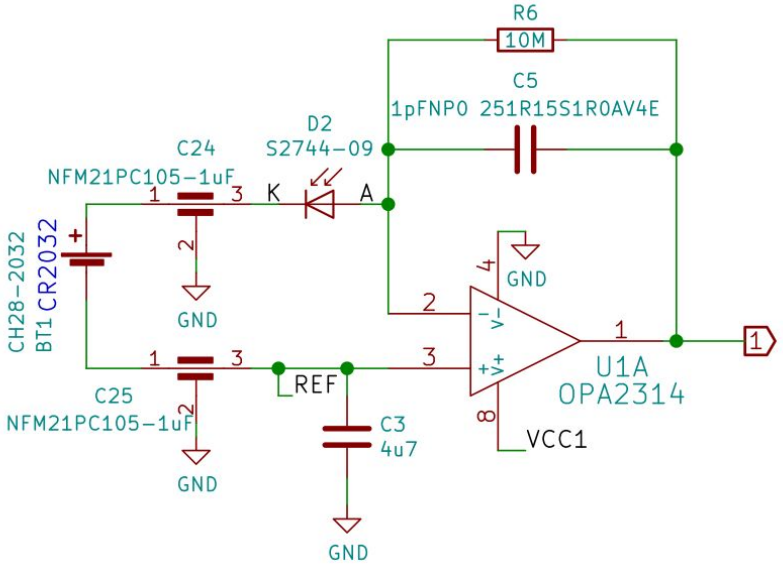

Figure 18*: Silicon PIN diode sensor and charge amplifier / trans-impedance amplifier.*

Voltage signal from the trans-impedance amplifier is filtered by a bandpass filter (figure 19). Each ionizing radiation event in the photodiode produces, after filtering/shaping, a pulse with a duration of about 80 µs (figure 20). Amplitude of the pulse is proportional to charge in case of a constant charge collection time and the charge is proportional to the deposited energy in a sensitive volume in the PIN diode.

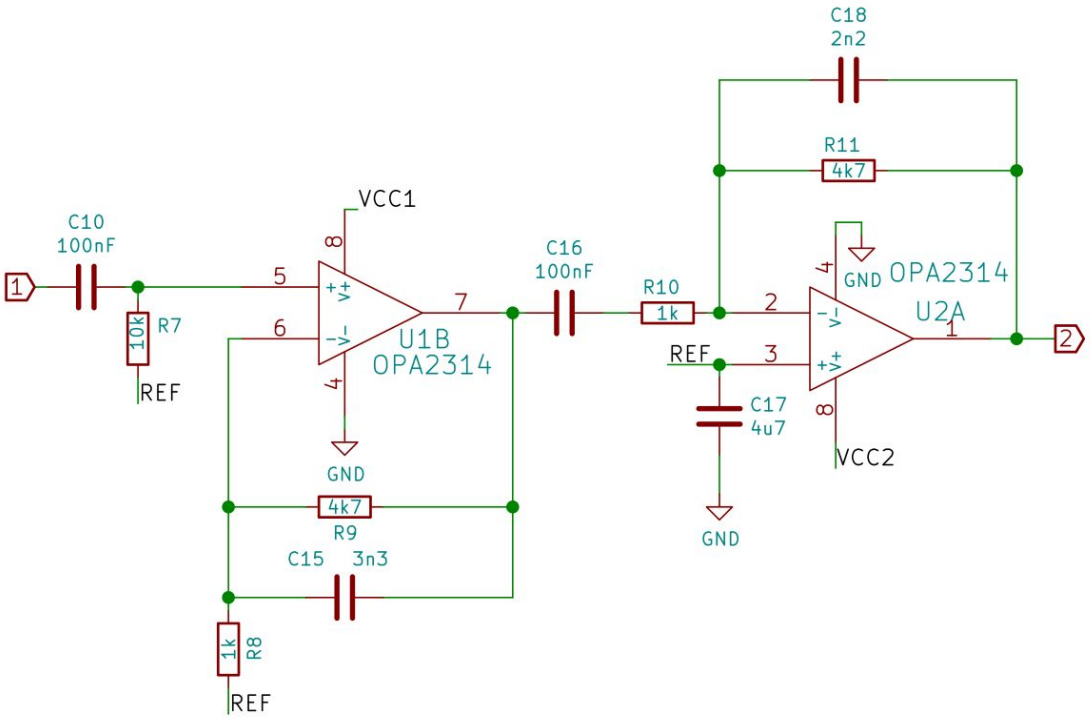

Figure 19*: Two stage bandpass filter and amplifier.*

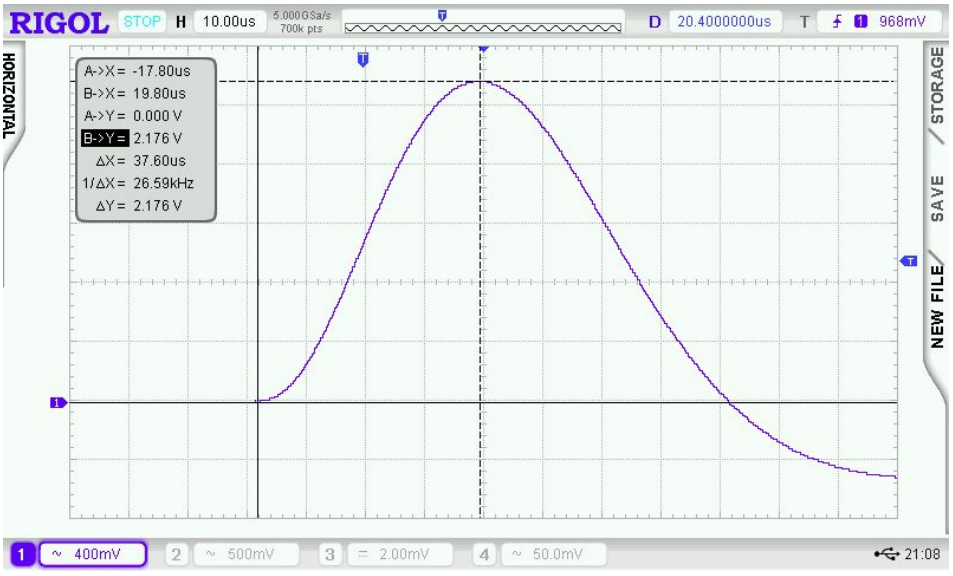

Figure 20*: Pulse response of analogue part of AIRDOS to ionising radiation event recorded by oscilloscope.*

Resulting pulses are stored in a specially developed sample-hold circuit that behaves as a signal follower and analog memory (figure 21). When signal #PeakDetect_Trace is in H an analog switch U5 turns on and a signal at an output U2B follows a signal at input (2) with slight delay which is done by R13 and C19. If signal #PeakDetect_Trace is switched to a high impedance state the analog switch U5 starts to be controlled by a comparator U4. In this case, when the input signal (2) goes from high to low, a positive input of comparator will be at a higher voltage than negative input, following a voltage at capacitor C19. It causes switching-off of the analog switch U5 and the capacitor C19 holds its last voltage value. This behaviour is similar to a peak detector circuit. Next the stored voltage can be converted by ADC (Analogue to Digital Converter) and after this conversion the input #PeakDetect_Trace goes again to H and circuit changes behavior to signal follower circuit. The described sample-hold circuit does not suffer with typical peak detector circuits ills like insensitivity to small signals, mistreatment of negative signals or discharging the capacitor by leakage current through diodes. Moreover, this circuit can be used as a pulse discriminator as well. The signal #PeakDetect_Trace can be connected to an input of digital circuits when it is controlled by the comparator U4. When the input signal (2) goes from high to low, the signal #PeakDetect_Trace goes from high to low as well. This behavior can be used for detection of falling edge of signal. There is only one constraint of this circuit, the input signal can not change raising/falling time widely and RC time constant (R13, C19) must be chosen correctly, respecting the input signal time properties.

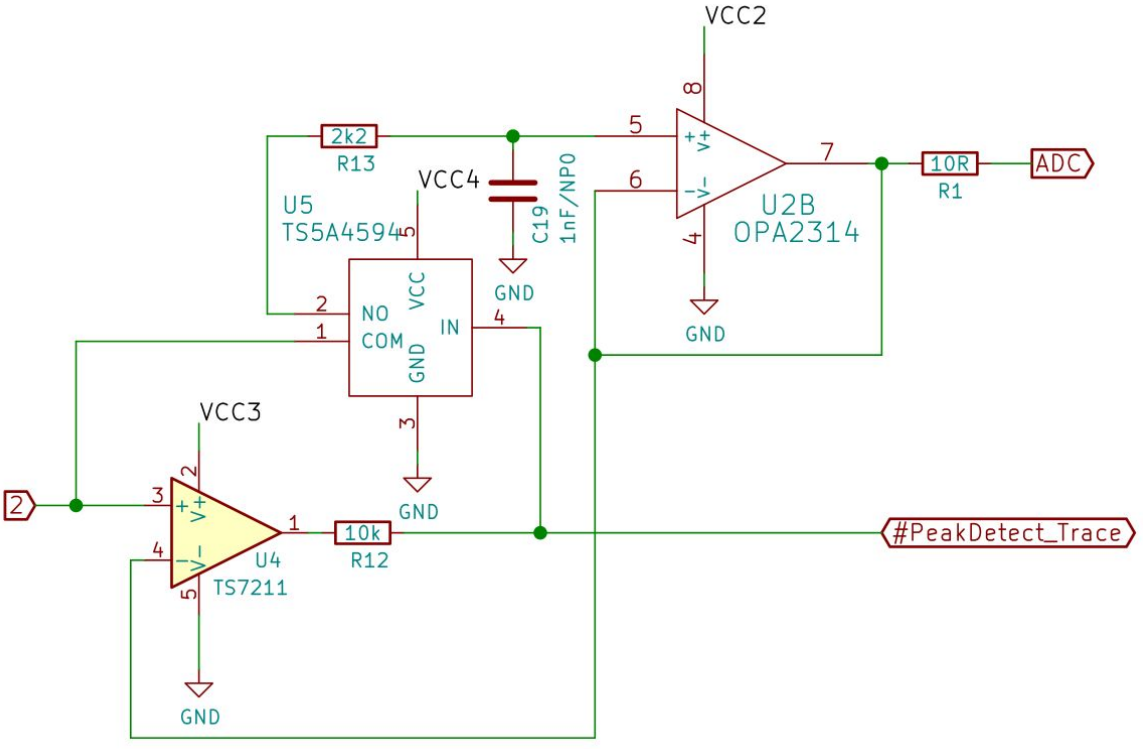

Figure 21*: Signal follower with analog memory. It is a circuit equivalent to a sample-hold circuit triggered by a falling edge of signal or a circuit equivalent to a peak detector.*

4.1.3. Digital circuits design

The heart of a data acquisition unit is the DATALOGGER01A module which was developed during AIRDOS design. Manufacturing documentation for this module is available on-line (Kákona and Chroust 2018b). Simplified schematics of the digital part of AIRDOS are depicted in figure 22 and figure 23. ATmega 1284P (Microchip 2018). This µC is a low power variant of ATmega 1284 and utilises differential 10-bit ADC (Analog to Digital Converter). Power consumption of this µC is less than 1 mA on working frequency 1 MHz (AIRDOS does not use an external crystal oscillator). Each manufactured AIRDOS contains a silicon serial number in the U6 (figure 22). This serial number is used as a marker for output data and helps registration of deployment of dosimeters and data pairing with specific aircraft.

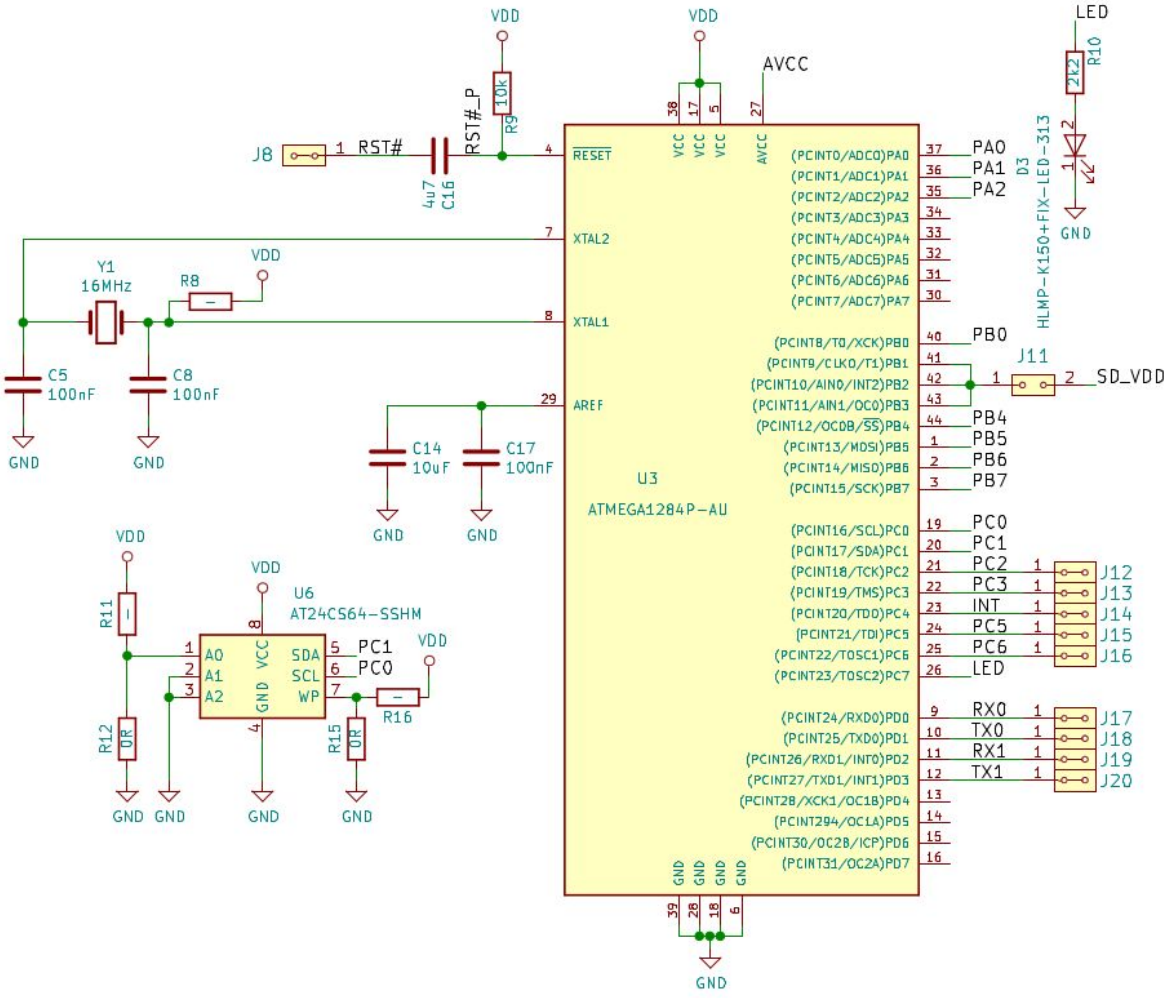

Figure 22*: Schematics of microcomputer with EEPROM.*

The rest of the electronics in figure 23 comprises an RTC (Real Time Clock) (U4) with an accuracy of 20 PPM, a power switch for switching-off the GPS (U2) and an SD card slot (J7). The whole SD card is switched-off during the dosimeter integration as well as the power for the GPS. Power for the SD card and GPS is controlled by firmware.

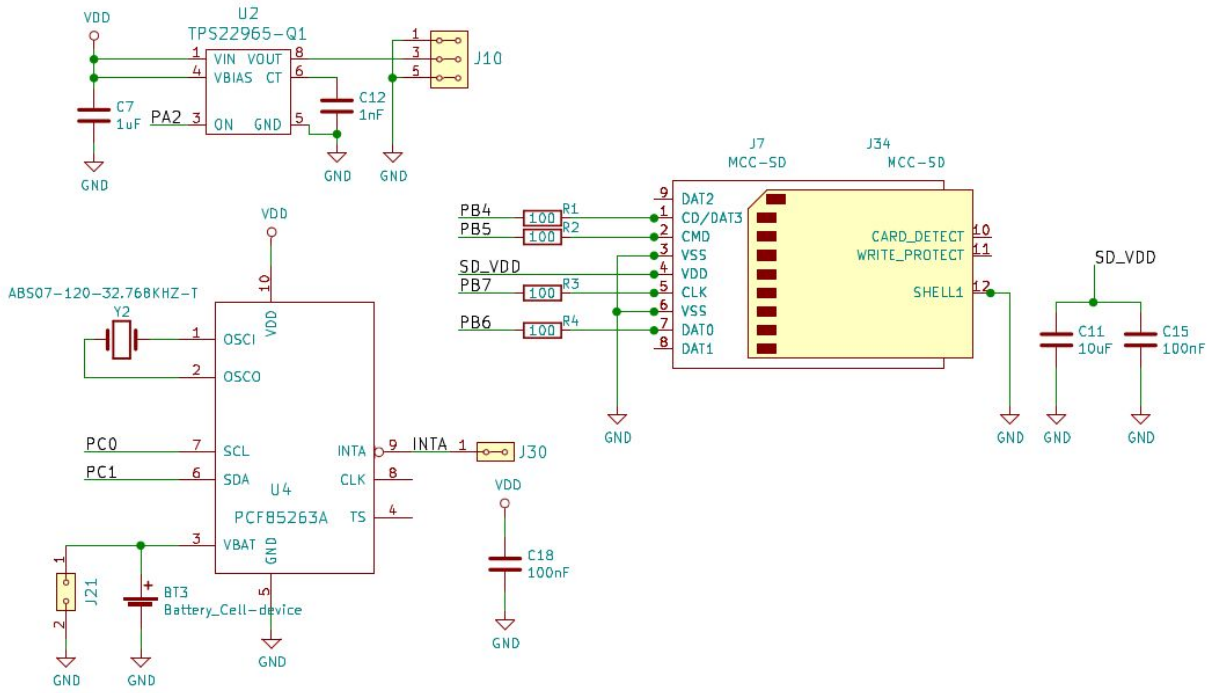

Figure 23*: Schematics of RTC, power switch and SD card reader.*

4.1.4. AIRDOS Firmware design

The firmware of AIRDOS was written in Processing environment (Processing Foundation 2001) for ease of modification by non-programmers (e.g. scientists). Source code of the firmware is available under GNU General Public License v3.0 on GitHub (Kákona 2018a) and the last version from the year 2019 is a part of this work as Attachment E.

There are two variants of the firmware: with and without a GPS receiver. The GPS receiver is the most power consuming part of the device. For reducing the power consumption, GPS receiver is switched off if averaged ionizing radiation flux is below some limit (a constant GPSthreshold in the firmware). The second most power consuming part of the design is the SD card. AIRDOS integrates ionizing radiation for about 10 seconds for reducing the power consumption of the SD card. The SD card is switched off during the integration and the power consumption of AIRDOS is under 10 mW during this period. Power consumption of SD card or GPS is ten times higher and may be optimized according to user requirements in the firmware.

There is no signal discriminator in AIRDOS hardware. Consequently, AIRDOS firmware periodically samples the analog signal. This sampling is asynchronous with ionization events and one event can accidentally belong to two neighboring samples. This circumstance has to be solved by a software filter. Filtering algorithm is described in figure 24. This algorithm is looking for local maxima of signal and stores these local maxima to an array Histogram[].

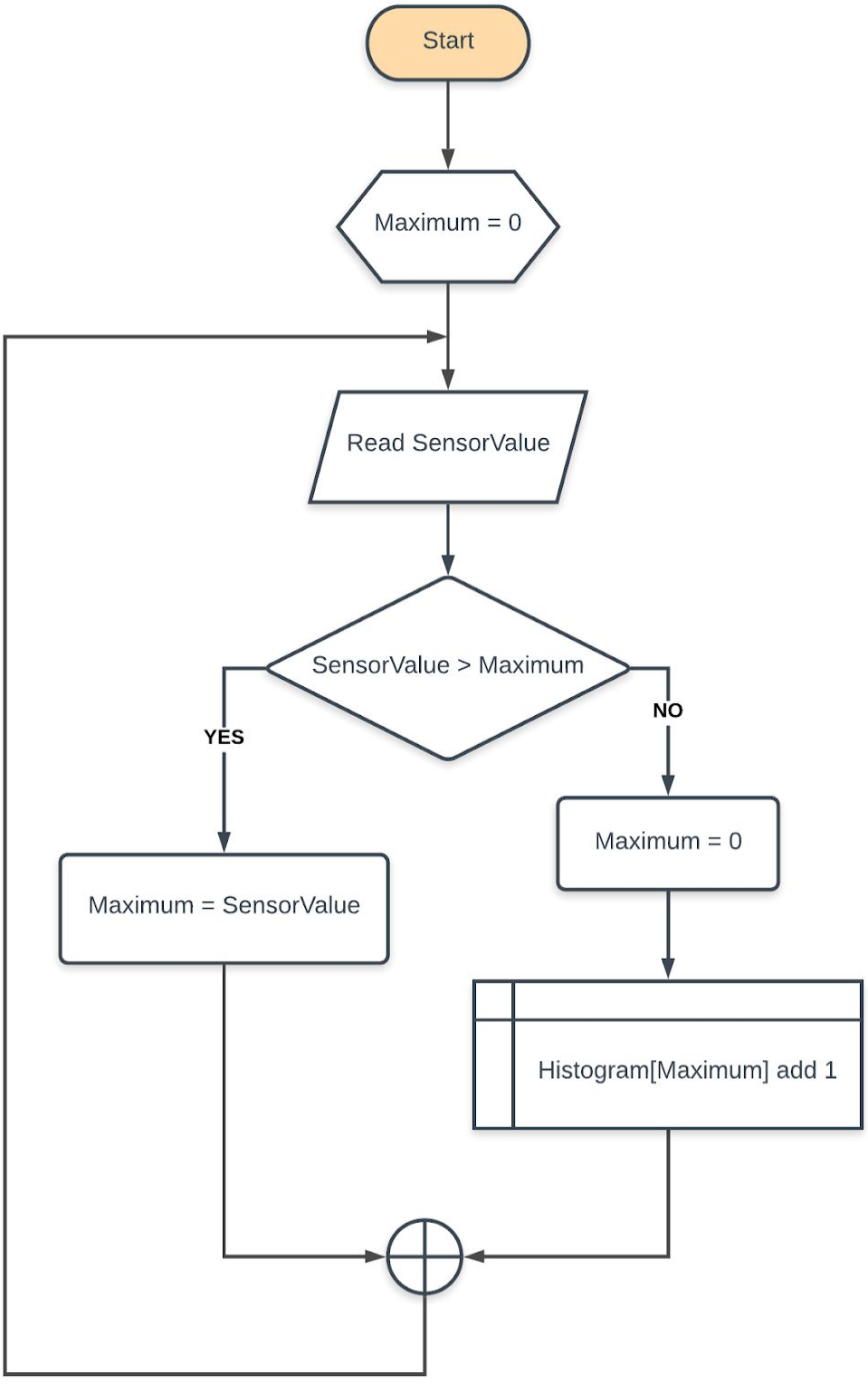

Figure 24*: Flowchart of algorithm for suppressing a double detection of events. SensorValue is a value obtained from ADC. Maximum is a local variable. Histogram is an array for output values sorted by deposited energy (in channels).*

4.1.5. AIRDOS Output

Data from AIRDOS can be obtained by an asynchronous serial protocol at UART (Universal Asynchronous Receiver/Transmitter) interface or can be stored on SD card.

Data format is described in protocol documentation at (Kákona 2019). Parsers for output data are also available as an open source code at (Kákona 2017). The source code of parser and the data format description are attached to this work as Attachment F and Attachment D respectively.

4.2. AIRDOS Calibration

4.2.1. Energy calibration

Linearity of energy response was investigated first. Defined charge was injected through a calibrated capacitor 1 pF (C_T) connected to a signal generator.

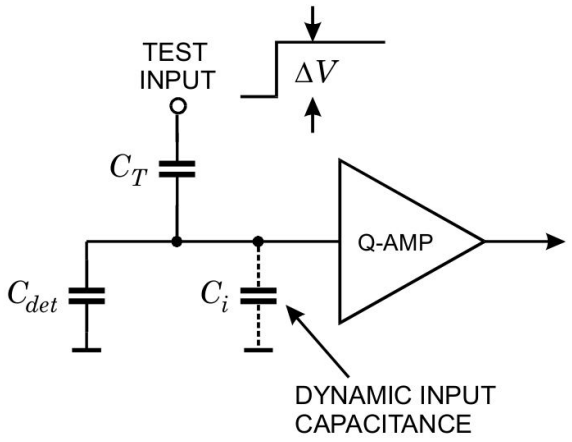

Figure 25*: Circuit for calibration (Spieler 2012).*

Rising edge of generated pulses was set to be equal to real pulses from ionisation events. Amplitude of voltage pulses (ΔV) was measured by an oscilloscope and charge was calculated using a formula

$$Q = \Delta V C_T ,$$

where Q is charge in Coulombs, C_T is capacity in Farads and ΔV is voltage in Volts. This formula is true in case $C_i >> C_T$. Capacity of photodiode C_{det} is two orders higher than our 1 pF capacitor (C_T) - therefore, in our case, this condition is fulfilled.

Now we can easily calculate the number of electrons corresponding to injected charge.

$$N_e = \frac{Q}{e},$$

where N_e is the number of electrons, *Q* is charge and *e* is the elementary charge (1.602×10^{-19} C).

Then, the estimated ionisation energy corresponds to number of electron-hole pairs

$$E = N_e \, \varepsilon_{e-h},$$

where *E* is the energy in eV deposited by ionising radiation, N_e is the number of released electrons and ε_{e-h} is equal to 3.65 eV for silicon and it represents mean energy for electron-hole pair creation.

Figure 26 shows the result of energy calibration by injected charge. As can be seen the response is perfectly linear.

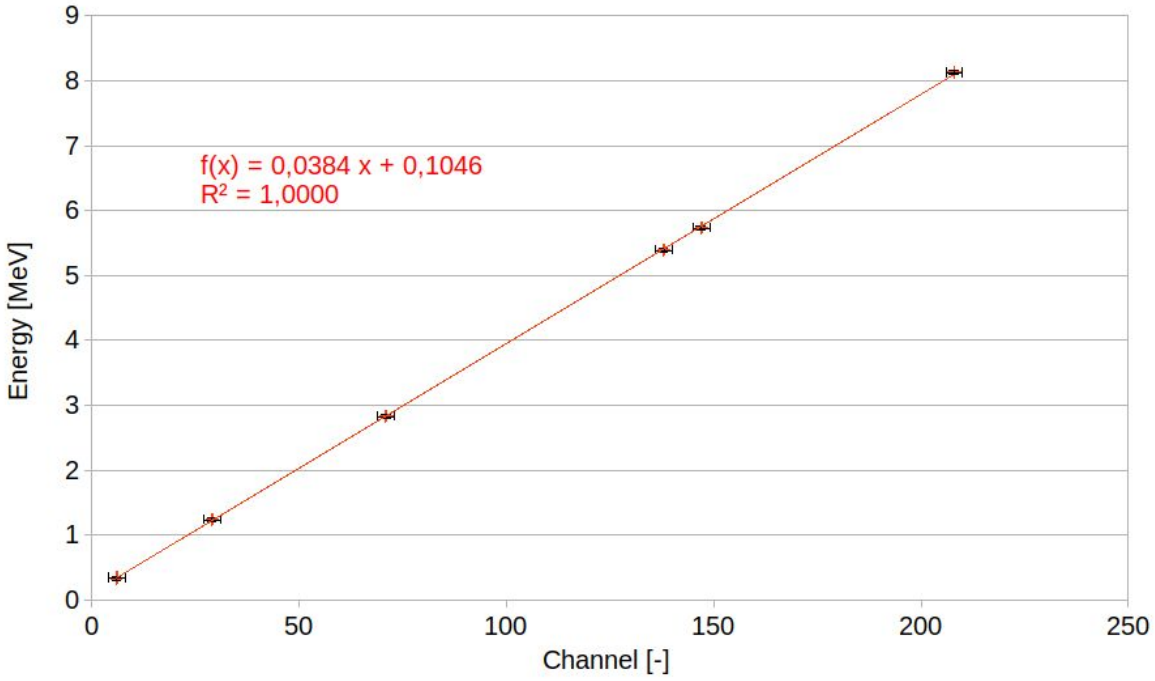

Figure 26*: Linear energy response obtained by injecting a defined charge into the input of charge amplifier. Depicted error bars display quantisation error of ADC.*

A second method of energetic calibration is a measurement of response to real ionising particles originating in radioactive nuclides or particle accelerators. Typical response of the detector is shown in figure 27, example of measurement setup is in figure 28. Calibration result and table of used ions are in figure 29 and table 3.

For energy calibration of AIRDOS alphas from radionuclide sources as representatives of “high LET” particles and protons and alphas from accelerators as representatives of “low LET” particles were used to cover all detector’s energy range. Deposited energies were calculated by SRIM program (Ziegler 2010; Ziegler et al. 2010). Figure 29 presents response for alpha

particles from radionuclide sources (^{239}Pu, ^{241}Am), alpha particles from HIMAC (Heavy Ion Medical Accelerator in Chiba) accelerator (Yamada 1995) and protons from U-120M accelerator (Křížek et al. 2018). From this figure it can be seen that measured energies from real particles slightly differ from method of injected charge presented above. Please note, that the real particles have to give theoretically lower values because of energy loss in an entrance window of the detector, limited lifetime of charge carriers and slower charge collection speed. However, we observed positive offset which can be attributed to the noise of the detector. This noise is caused mainly by a current noise of the input of the trans-impedance amplifier and thermal noise/dark current of the diode. This noise is proportional to the internal capacity of the photodiode and is negligible in case of charge injected by capacitor because capacity of the sensor is two orders higher than the capacity of the capacitor used for injecting charge.

Four manufactured AIRDOS dosimeters were checked by the method described above, the differences in calibration between individual pieces are less than one channel of ADC. We can conclude that the calibration of individual devices is not necessary.

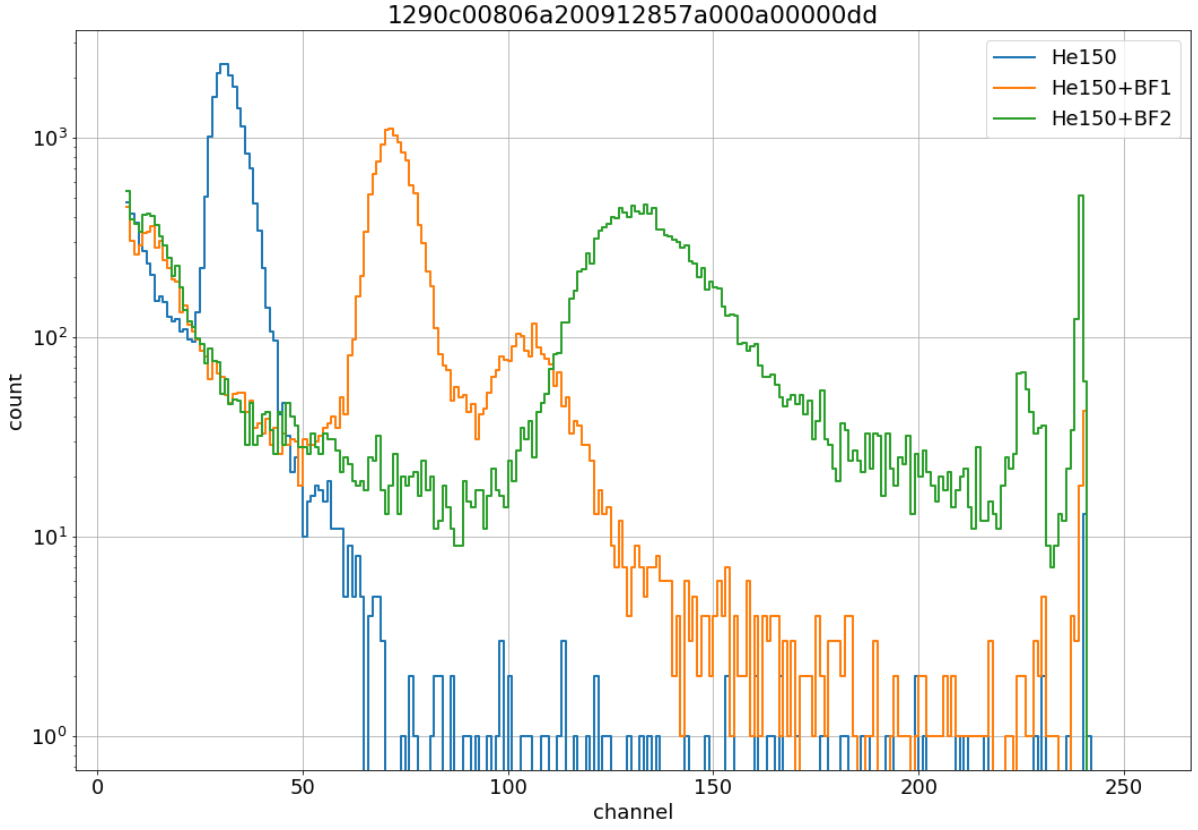

Figure 27*: Example of irradiation of AIRDOS by helium ions with energy of about 150 MeV/u (blue line) and a response to attenuated beam in PMMA (Polymethyl methacrylate) filter equivalent to 127.68 mm H_20 (orange line) and equivalent to 142.02 mm H_20 (green line). The second peaks (most prominently visible on the orange line) are from recoiled particles in a beam probe (see* figure 28*). The very small peaks in the left portion of the orange and green lines are probably particles recoiled from the filters. Irradiation was performed at HIMAC. (The number above the graph is a serial number of the AIRDOS device.)*

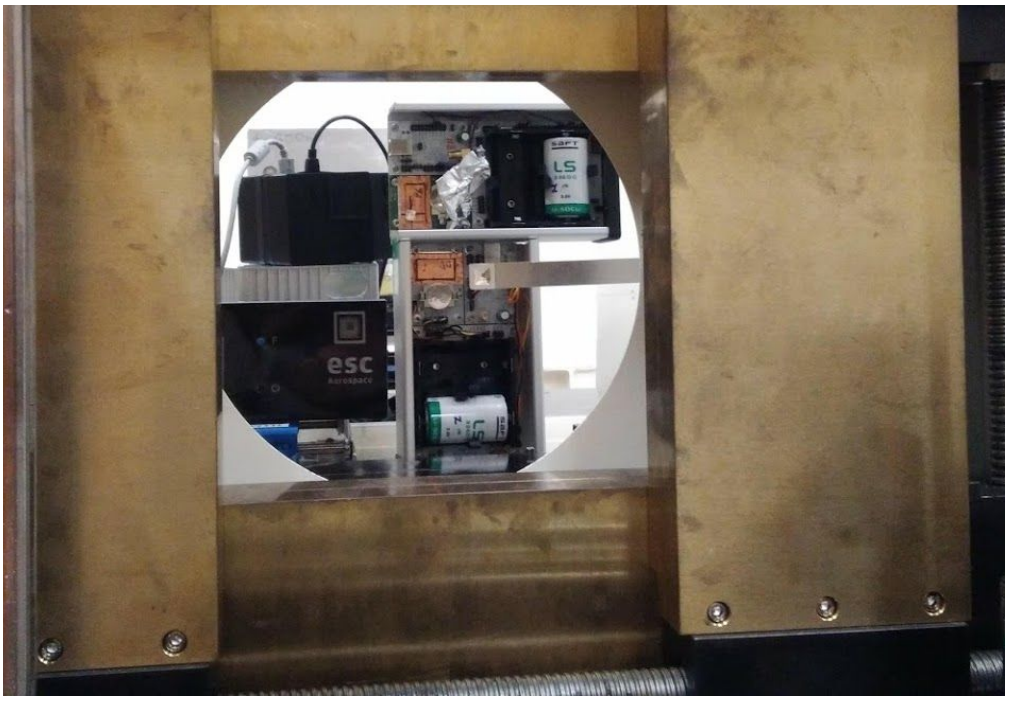

Figure 28*: Measurement setup in the HIMAC Bio room. AIRDOS s.n. 98 (top) and AIRDOS s.n. DD (bottom) are irradiated. The beam probe is in the centre of the picture (to the right near the AIRDOS sensor). The picture is taken from the beam view.*

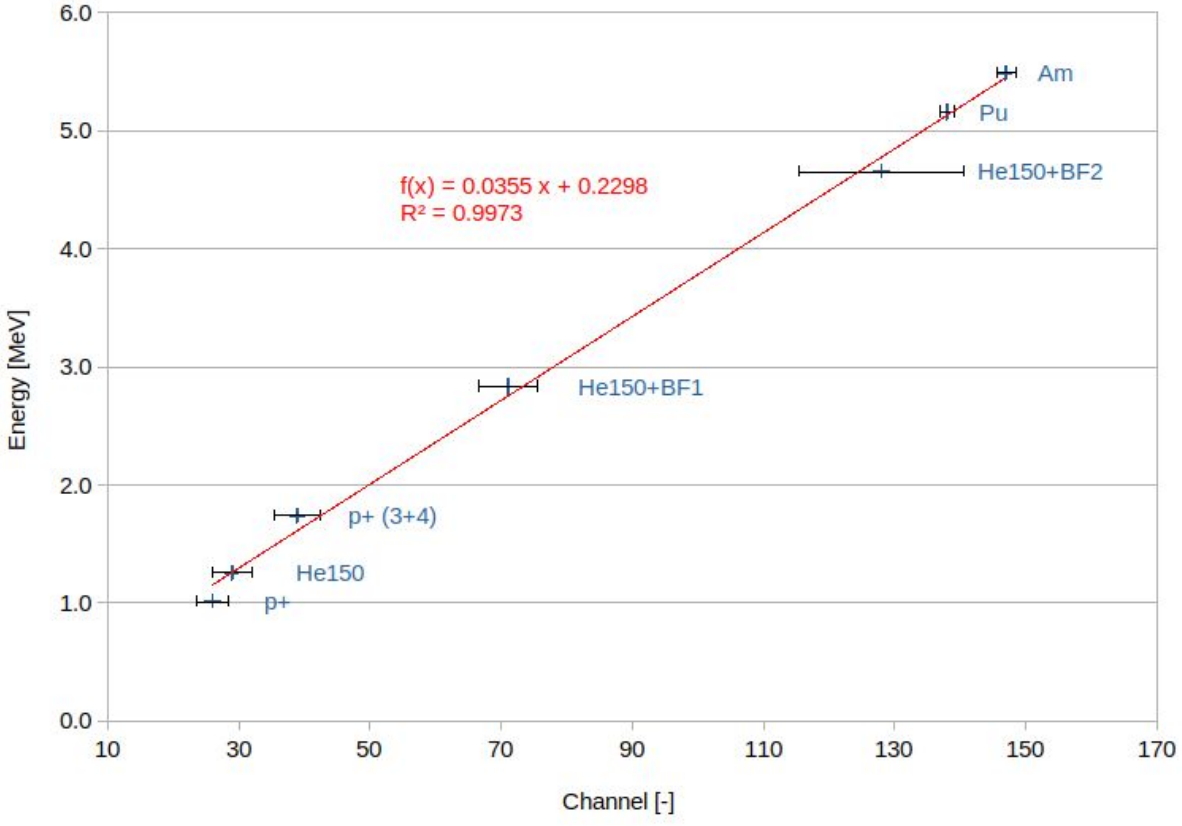

Figure 29*: Energetic calibration of AIRDOS. Depicted errors are FWHM values. Used ions are described in* table 3*.*

Table 3*: Table of ions used for AIRDOS energy calibration.*

Source name	Origin	Calculated Deposited Energy in Si [MeV]
He150	HIMAC Helium 150 MeV/u	1.3
He150 + BF 1	HIMAC Helium 150 MeV/u with filter equivalent to 127.68 mm H^2O	2.8
He150 + BF 2	HIMAC Helium 150 MeV/u with filter equivalent to 142.02 mm H^2O	4.7
p+	U-120M Protons	1.0
p+ (3 + 4)	U-120M Protons with Al filters	1.7
Pu	Calibration alpha source EA14 AMPU 14 with ^{239}Pu and ^{241}Am	5.2
Am	Calibration alpha source EA14 AMPU 14 with ^{239}Pu and ^{241}Am	5.5

4.2.2. Thermal sensitivity

Thermal sensitivity of AIRDOS was tested with alpha particles from ^{241}Am and ^{239}Pu radionuclide thin layer calibration sources during cooling in the refrigerator. The data from this test are depicted in figure 30. The difference in temperature results in difference in detected deposited energy in scale of one channel (38 keV) per 12 °C.

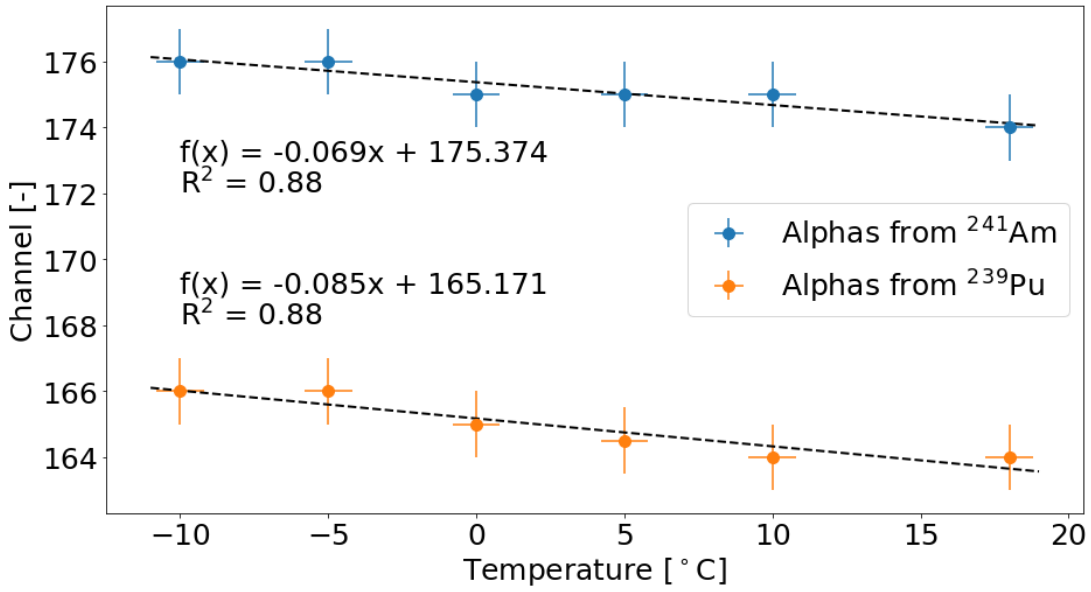

Figure 30*: Dependence of energy response of AIRDOS on temperature. Depicted measurement's uncertainties come from method of measurement (slow continuous cooling of device) and from quantisation error (channels have discrete values).*

4.2.3. Flux calibration

Calibration to the flux of charged particles is not needed because AIRDOS dosimeter detects all particles up to flux which does not cause pile-ups. For intended use of AIRDOS dosimeter on board aircraft the fluxes are very low with respect to the used diode area so the pile-ups are very rare. Only dead time must be taken into account. There are two types of dead times in AIRDOS, time for writing data to SD card and time for obtaining absolute time and position information from GPS. These periods should vary slightly depending on GPS signal quality or internal file system conditions of SD card. Nevertheless, integration time of one measurement cycle (time for collecting data to histogram before writing to SD card) is constant and is specifically 10.4 s. ADC performs 46000 samples during this period. Timeout for waiting for GPS signal is 58 s. Time for writing to SD card alternates from 2 to 4 s depending on SD card type and condition. We can conclude than number of events/particles in one measurement cycle must be divided by 10.4 for obtaining the rate per second.

4.3. Comparison of AIRDOS with Liulin

We compared AIRDOS dosimeter with Liulin dosimeter which has the same PIN diode sensor. A comparison with Liulin dosimeter was done on board aircraft at selected flights and long term measurement at high mountain observatory. Results of this comparison were published at work (Kákona, Štěpán, et al. 2019). Differences in dose in silicon measured by Liulin and AIRDOS are below 10 % with systematic error +4.75 % due to $\exp^2$ nature of the cosmic rays spectra. Please note that this comparison was done from deposited energies above 250 keV. It is due to different designs of Liulin and AIRDOS dosimeters because Liulin dosimeter uses a signal discriminator which introduces jitter to first channels (lower energies). Therefore these channels were omitted in comparison.

4.4. Operational dosimetric values calculation

A challenging task with solid state detectors is a measurement of operational dosimetric quantities (e.g. H*(10)) in mixed radiation field. On one hand, AIRDOS is intended for measurement of mixed radiation field with huge ranges of energies and with the different types of particles and on the other hand AIRDOS is capable to detect only specific particles within narrow energy range. According to this the ambient dose equivalent must be interpolated from limited sample of mixed radiation field measured by this device. There are several approaches to how to calculate the operational dosimetric quantities from energy deposited in silicone (Ploc et al. 2013; Wissmann and Klages 2019). In the next chapter, we will utilise simple approach of (Wissmann and Klages 2019). Another factor which influences dose calculation is the active volume of a sensor in which the charge is released by ionizing radiation and subsequently collected. We can find different values of the active volume for the used sensor in literature (Meier et al. 2016; Uchihori et al. 2002). Discussion about the correct sensitive volume is part of this dissertation work - see chapter 5.2. Assessment of Sensitive volume.

4.5. Comparison of AIRDOS measurements with model

For comparison with a model, the flight from Prague (PRG; Cutoff Rigidity = 3.5 GV) to Malaga (AGP; Cutoff Rigidity = 8.6 GV) and back was performed (figure 31). Measurement campaign lasted from 2019-11-28 16:00 to 2019-11-29 01:10 UTC and for calculation of dose the time from 2019-11-28 18:55 to 2019-11-28 20:55 was used for the flight PRG-AGP and from 2019-11-28 23:00 to 2019-11-29 00:30 for the flight AGP-PRG. Four different AIRDOS devices were used, having serial numbers 16, 21, 98 and F0.

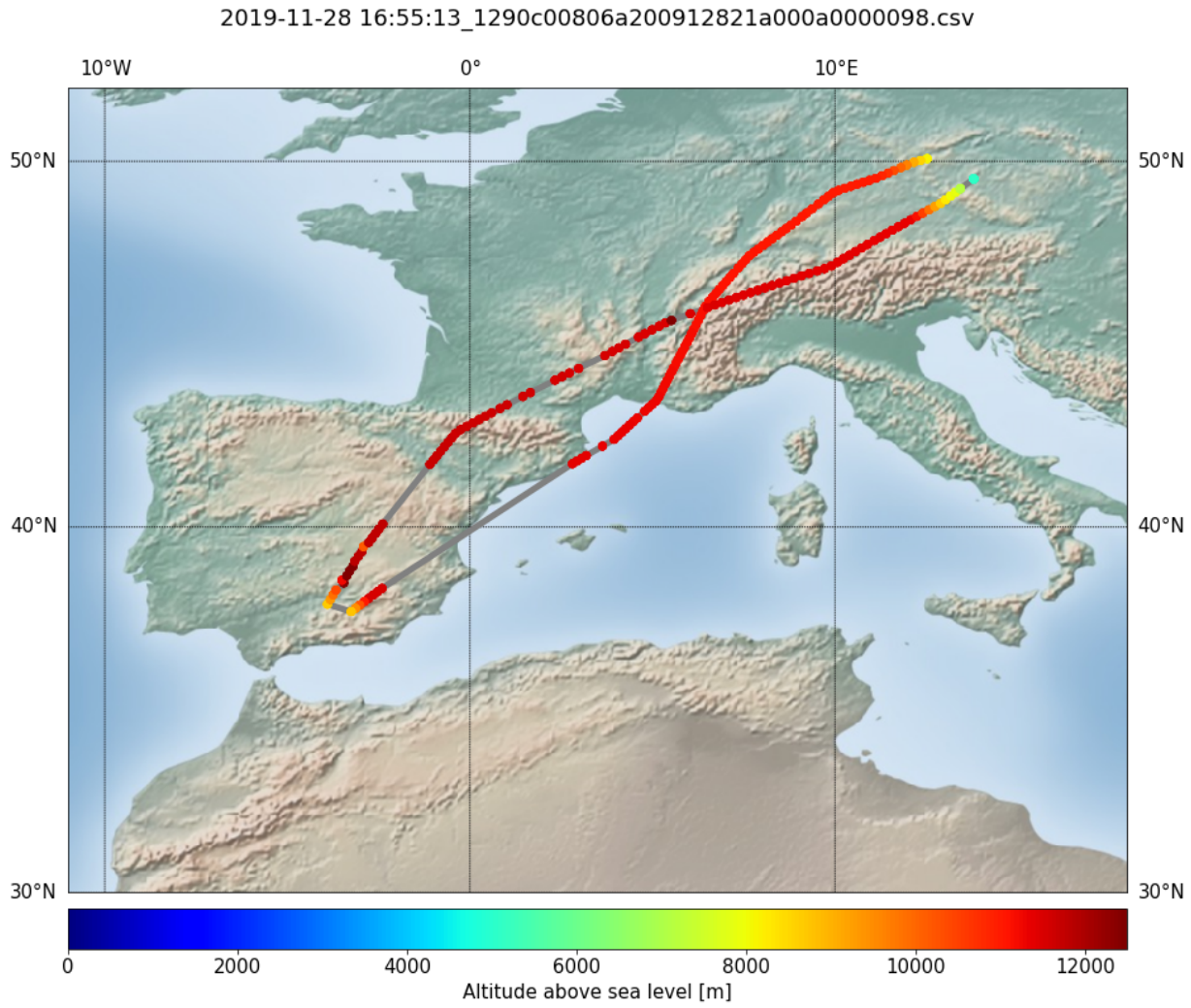

Figure 31: Flight from Prague to Malaga and back with flight altitude obtained from GPS projected on the map. *(The name of the data file above the graph contains time of the first GPS Fix and serial number of AIRDOS device. This measurement flight was performed by our group in November 2019.)*

Calculation of an effective dose during the flight was done by CARI 7 computer program (Copeland et al. 2017). CARI 7 uses a database of atmospheric response which is generated by Monte Carlo particle transport program MCNPX 2.7.0. Modulation of cosmic rays by the solar wind is taken into account by the monthly averages of the heliospheric potential available at FAA (Federal Aviation Administration) web site (Copeland et al. 2017; FAA 2019).

For calculation of an ambient dose equivalent rate from a dose rate in silicon provided by AIRDOS, we used the approach described in (Wissmann and Klages 2019). This method was established for Liulin, nevertheless AIRDOS utilises the exactly same PIN diode as Liulin thus dose in silicon has to be the same. Liulin has different energy range but particles with deposited energy higher than 9 MeV are rare on board aircraft (we can see in figure 32 that only 9 events were registered over the range of AIRDOS during both flights) and lower channels (with deposited energy < 200 keV) are usually omitted in Liulin data.

Spectrum measured with AIRDOS during the flight is in figure 32.

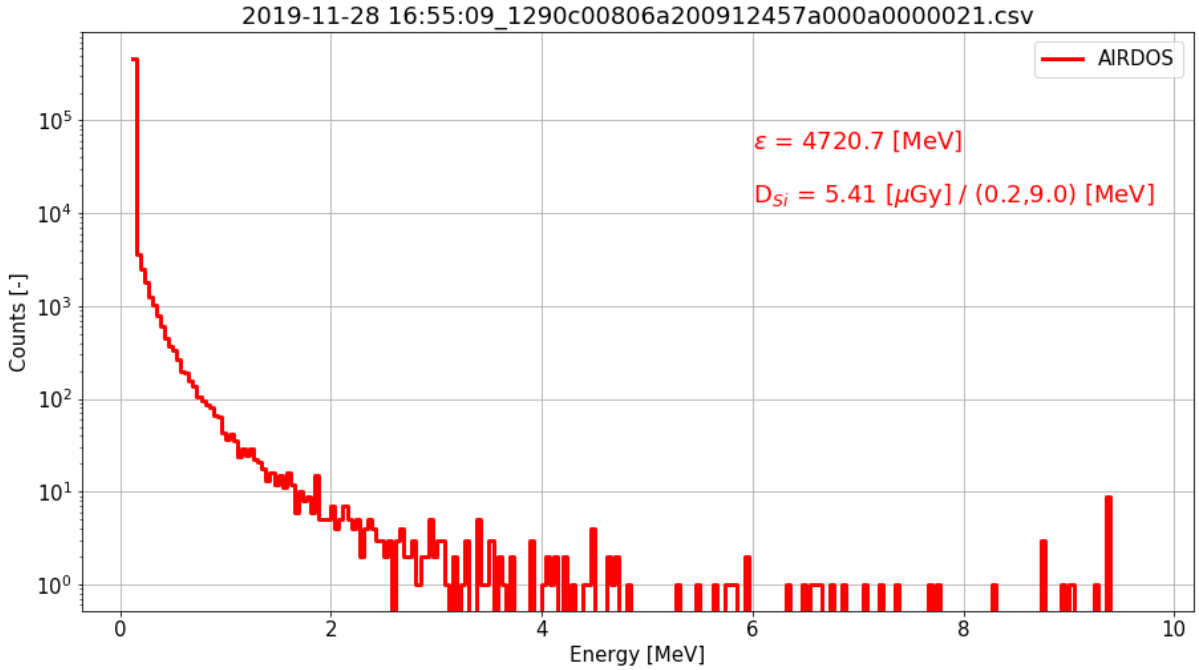

Figure 32*: Spectrum obtained during the whole measurement campaign (from 2019-11-28 18:55:00 to 2019-11-29 01:00:00 UTC i.e. 21900 seconds) including waiting at Malaga airport. The ε is a whole deposited energy and D_{Si} is a dose in silicon for a given range of energies. (The name of the data file above the graph contains time of the first GPS Fix and a serial number of AIRDOS device.)*

First, we have to calculate the dose rate in silicon

$$\frac{dD_{Si}}{dt} = \frac{\sum_{i=4}^{250} 0.384 \,.\, N_i + 0.105}{m_{Si}\Delta t},$$

where coefficients are taken from figure 26, m_{Si} is 0.1398 g and integration time Δt is 10.4 s. N_i is the number of events registered in channel *i*.

Then we apply coefficients for conversion dose in silicon to ambient dose equivalent

$$\frac{dH^*(10)}{dt} = \frac{dD_{Si}}{dt}\; k_{Dead}\; k_{Liulin/Airdos}\; k_{Sv/Gy}\,.$$

Where, $k_{Dead} = 1.10$, it compensates the Dead Time of the AIRDOS detector, $k_{Liulin/Airdos} = 1.14$, it represents a conversion factor between Liulin and AIRDOS, it comprises of 9.4 % for different energy ranges and 4.8 % for systematic difference due to different channel energy width (Kákona, Štěpán, et al. 2019), $k_{Sv/Gy} = 2.45$, it is a mean value of a calibration factor (Wissmann and Klages 2019) for the geomagnetic cutoff rigidities from 3.5 to

8.6 GV. Calculated values for the four AIRDOS devices are displayed in the graphs in figure 33.

Now we can compare the measured/calculated ambient dose equivalent (by AIRDOS) with an effective dose calculated by CARI 7 in table 4. AIRDOS s.n. 98 has a different firmware with GPS measurements occurring more often. Thus we could not include its measurements in comparison because these values have to be systematically lower. However, the dose rates measured with the device s.n. 98 displayed in figure 33 are comparable with other devices. For the deposited energy the calculation formula from figure 23 was used. Despite the fact that the general calibration formula was used and calibration for individual manufactured AIRDOSes has not been taken into account, the errors in ambient dose equivalent are mostly less than 10 %. Differences between the devices are mostly due to a DC offset of the A/D converter. This offset is compensated in the firmware but the compensation can be done with granularity of one channel width only (i.e. about 40 keV). This compensation is done according to chapter Offset Compensation Schemes in a datasheet (Microchip 2018).

We have to add a note about quantities used for the comparison. The effective dose E (ICRP 2007) provided by CARI 7 can not be directly measured therefore we use the ambient dose equivalent H*(10) (ICRP 2007) for the AIRDOS measurements. The ambient dose equivalent is commonly used as a conservative estimation of the effective dose in case of isotropic radiation (ICRU 2010b).

Table 4*: Comparison of doses calculated by CARI 7 program and doses measured with four manufactured dosimeters. Please note that error of the used computation method (Wissmann and Klages 2019) of the ambient dose equivalent is* ±2.6 % and CARI 7 model deviation from ICRU reference data is from -4 % to +14 % (Copeland 2017).

	PRG-AGP		**AGP-PRG**	
Program or Dosimeter	**H*(10) or E [μSv]**	**Difference**	**H*(10) or E [μSv]**	**Difference**
CARI 7	8.7	reference value	7.6	reference value
AIRDOS s.n. 16	8.9	+2.3 %	7.3	-3.6 %
AIRDOS s.n. 21	8.2	-5.5 %	6.8	-10.2 %
AIRDOS s.n. 98	6.7	n/a	5.9	n/a
AIRDOS s.n. F0	9.2	+5.5 %	7.6	+0.1 %

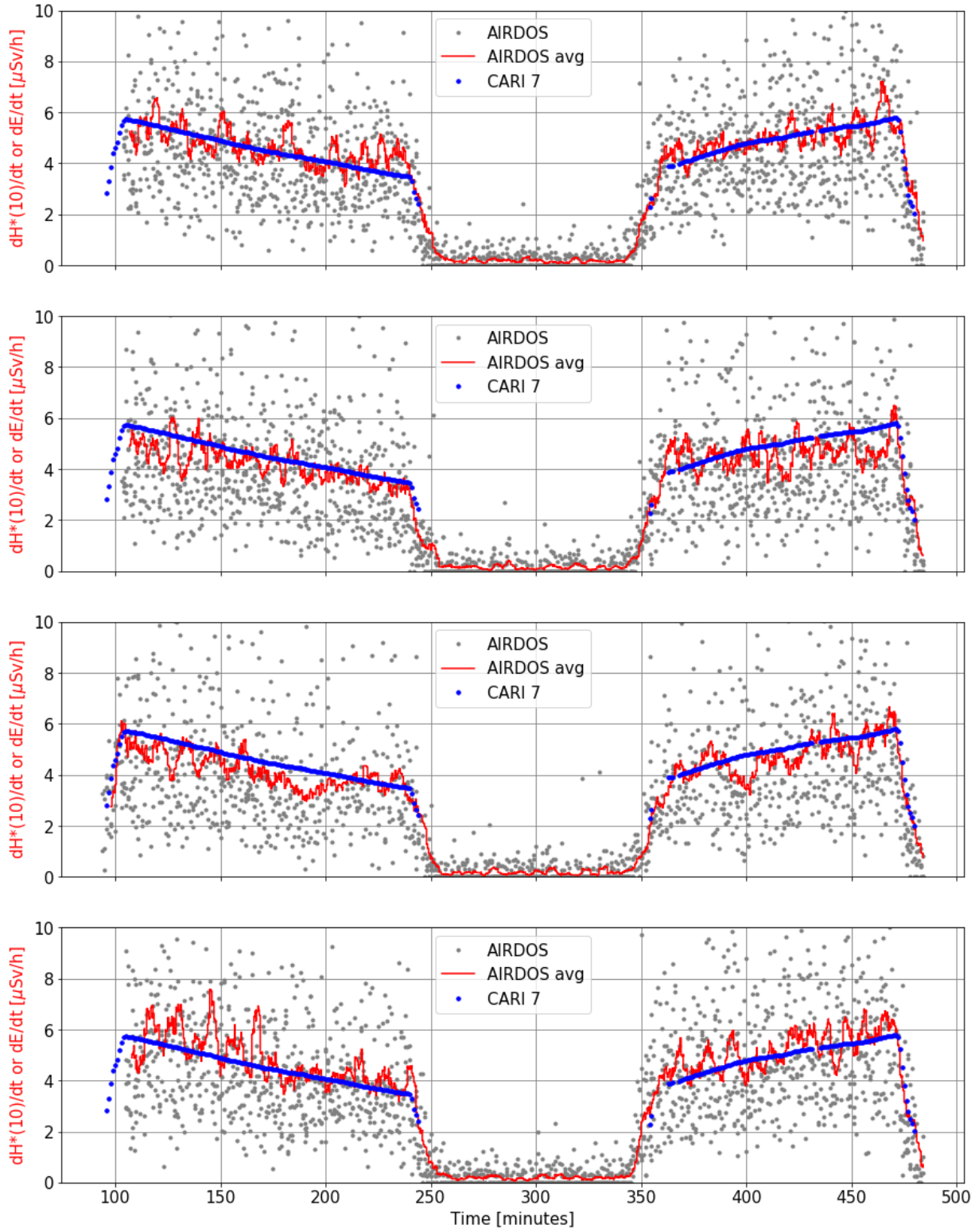

Figure 33*: Radiation profiles of flights PRG-AGP (left) and AGP-PRG (right) in time. Gray points are particular measurements recalculated to ambient dose equivalent rate. Each measurement lasted 10.4 s. Red curves are running averages for 20 measurements. Blue dots are effective dose rates calculated by CARI 7 according to the flight route. Measurements were performed with AIRDOSes with serial numbers 16, 21, 98 and F0 from the top to bottom.*

4.6. Conclusions about AIRDOS dosimeter design

Finally reached parameters of the initial public design of AIRDOS are summarised in table 5.

Table 5*: Parameters of AIRDOS dosimeter (for version 02 F).*

Dimensions	166 x 107 x 57 mm^3
Weight	730 g
Energy range	from 0.2 to 9 MeV
Number of channels	240
Channel width	38 keV
Integration time	10.4 s
Continuous measurement	6 months
PIN diode type	Hamamatsu S2744-09
Battery	2x LS 33600
Flash memory	SD card

A new open source dosimeter for measurements on board aircraft was introduced. It is the first step towards future improvements and innovations originated in the public scientific community based on a fully described open source design. We share our effort for better understanding of solid state dosimeters. We hope that we encourage other scientists and designers to introduce their ideas to an open science in mixed radiation field dosimetry.

5. Improving of radiation measurements with PIN diode dosimeters

5.1. CANDY detector

During the design of AIRDOS dosimeter, a lot of parameters and hypotheses were tested experimentally. These tests (mostly described in the section of thesis below) were performed using a laboratory design/detector CANDY (figure 34). This design uses faster operational amplifiers than AIRDOS design due to the better time resolution. A disadvantage of CANDY design is its more than three times higher power consumption than front-end electronics of AIRDOS.

Figure 34*: CANDY detector - mechanical setup. Please consider the size of AA batteries in order to imagine the dimensions.*

5.1.1. HW design

Schematics of CANDY detector are shown in figure 35 and figure 36. Detector consists of a silicon PIN diode (D1, Hamamatsu S2744-09 or BPW34) as an ionizing radiation sensor, a charge amplifier (U1) and an active filters (U2A, U2B). The circuit of the charge amplifier was designed according to a recommendation in a (Linear Technology 2006) datasheet. Capacitor C4 is implemented directly on PCB as an area of copper. Bias voltage (Ubias) can be set from 0 to 33 V due to a limitation of capacitors C1 and C15 and used PIN diode. Output of CANDY was connected directly to 1 MΩ input of an oscilloscope for recording individual pulses.

There are two PIN diodes utilized in performed experiments Hamamatsu S2744-09 and BPW34. The PIN diode S2744-09 is a flat silicon chip with dimensions 10 x 20 mm and thickness of depletion region 300 µm (HAMAMATSU 2011). It can register charged particles and photons within deposited energy range (for this setting) from 200 keV to tens of MeV. The PIN diode BPW34 is a small photodiode 7.5 mm^2 with a thickness 100 µm (Vishay 2019).

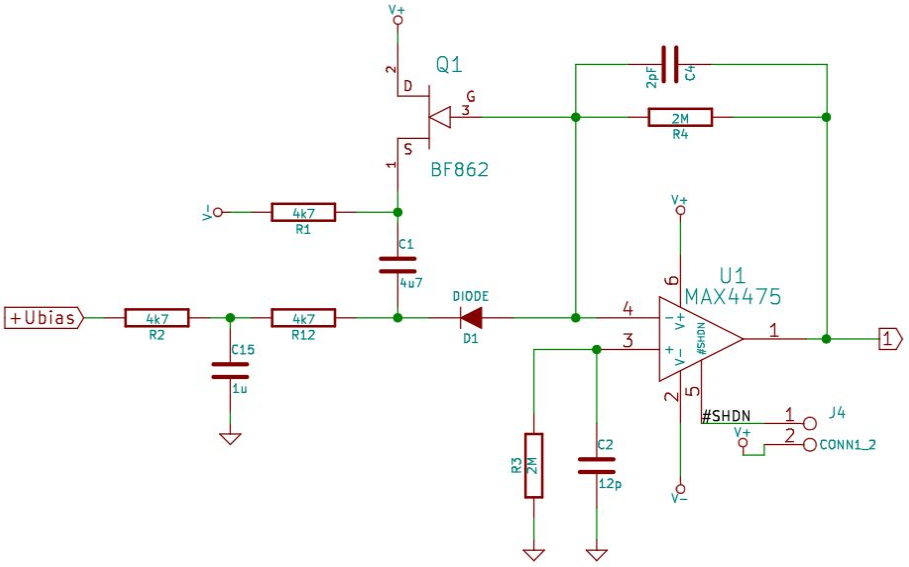

Figure 35*: Schematic of CANDY detector - Charge Amplifier.*

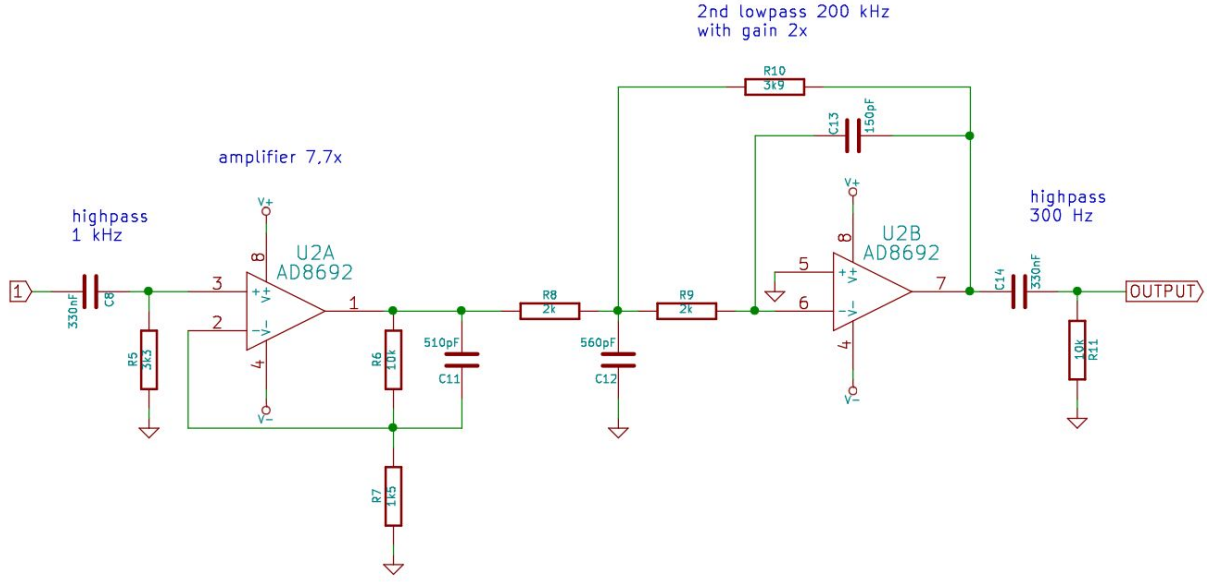

Figure 36*: Schematic of CANDY detector - Bandpass Filter.*

5.1.2. Data processing

Radiation events in CANDY detector were recorded by a digital storage oscilloscope with a specially developed program (Kákona 2016) in all experiments. Full shape of each pulse was recorded. Each ionization event produces a pulse with a specific amplitude and shape. Captured pulses can be plotted into the histogram (see example in figure 37) - these are

sample of data captured by CANDY detector in mixed ionizing radiation field at CERF (Silari and Pozzi 2017) where measurement setup was tested before deployment on board aircraft. Data are sorted by amplitude (vertical axes) and area of pulse (horizontal axes). Each point represents one pulse with a specific amplitude and with a specific pulse area. Color of points represents the number of pulses with the same shape (same amplitude and same area). Two pulses lying between the red lines in figure 37 are displayed in figure 38. There are several pulses with the same amplitude (lying between the horizontal red lines) and with different shape (area of pulses is different). Note that the area of the pulse corresponds to released charge/deposited energy in active volume of sensor and the shape of the pulse corresponds to the speed of collection of the charge in/from the sensor. Second intersection in the histogram is done by black lines. Figure 39 shows pulses which correspond to the same energy/charge collected but with different amplitudes. As follows from this figure, there are many kinds of interaction of ionizing radiation inside the diode. We will use this method of visualization (figure 37) for experiments described further in this text without detailed graphs of individual pulses (figure 38 and figure 39).

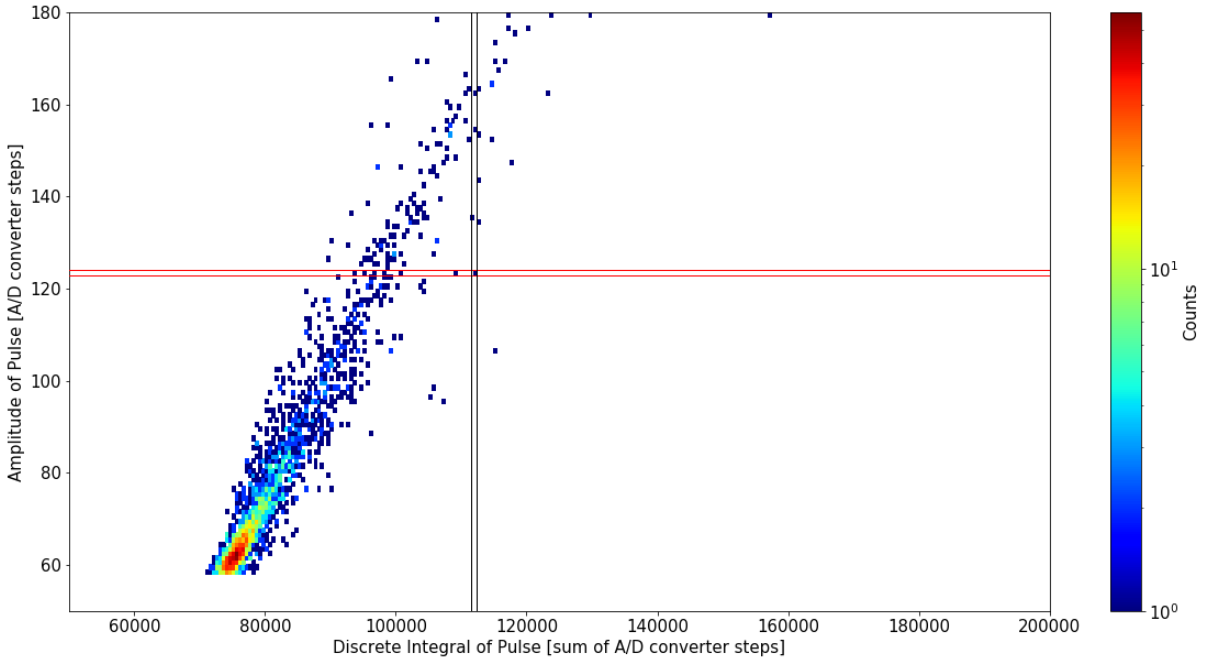

Figure 37*: Histogram of events depending on pulse shape captured at CERF.*

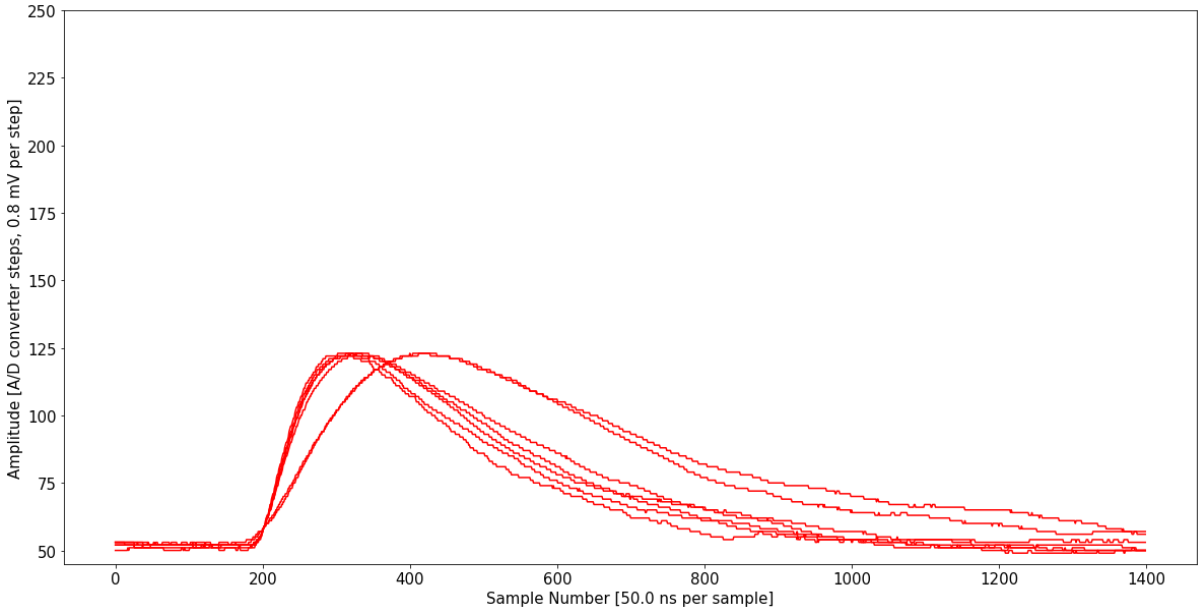

Figure 38*: Shape of pulses lying between red lines in* figure 37*. Amplitude of all pulses is the same. Pulses differ in their area.*

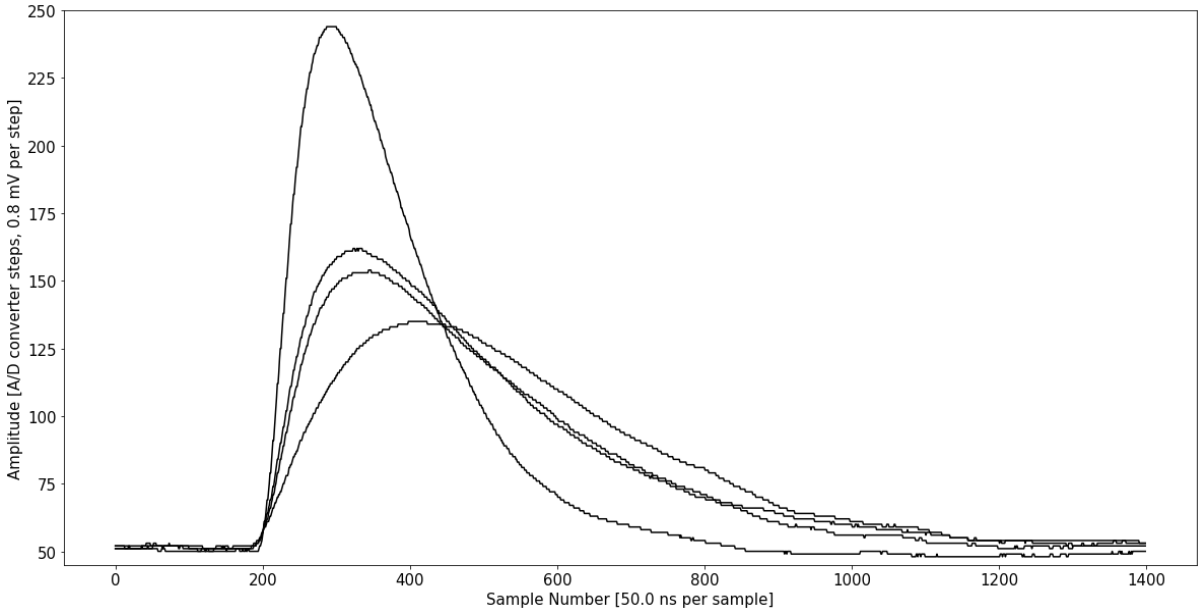

Figure 39*: Shape of pulses lying between black lines in* figure 37*. Area is the same for all depicted pulses. Pulses differ in amplitude and slope.*

5.2. Assessment of Sensitive volume

5.2.1. Laboratory setups

Sensitivity of volume of PIN diode was tested in measurement setup depicted in figure 40. Sensor is deployed on a moving platform with precise positioning within an accuracy better than 0.1 mm. The beam size was in order of ones of mm. The sensor was irradiated by He nuclei with energy of 230 MeV/u at HIMAC (Yamada 1995).

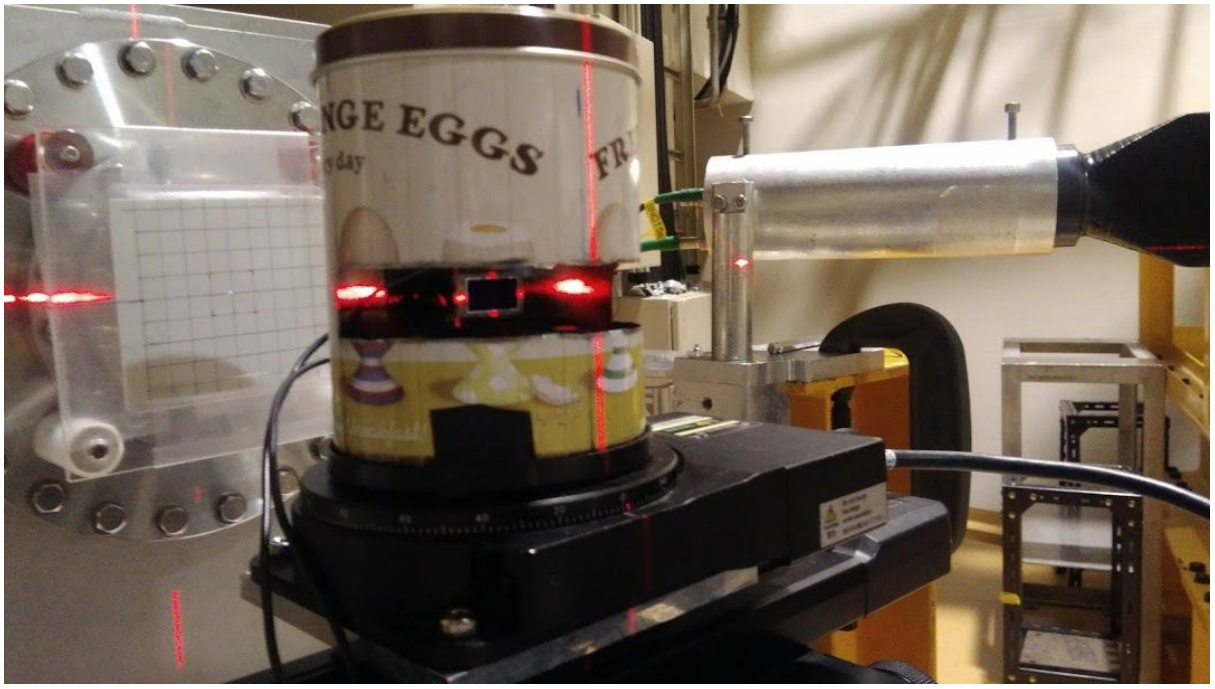

Figure 40*: Experimental setup for investigation of the Edge Effect and the dependence of thickness of depleted region on bias voltage. Output of HIMAC Physics beam can be seen on the left side and Hamamatsu PIN diode is near the center of the picture. Laser cross is projected on the white frame of a ceramic package of the diode inside a metallic can.*

The second measurement was performed at Tandetron 4130 MC facility (Romanenko et al. 2019) in Nuclear Physics Institute in Řež. The beam of 3 MeV protons with diameter less than 0.5 mm was used. Sensor was again placed in a metal can with an aluminium foil window (with thickness 15 μm) on a moving platform (figure 41). Position of the sensor was measured relatively based on a position of aluminium sheet placed on the sensor. Measurement of position was performed with an accuracy of 0.1 mm by dial indicator.

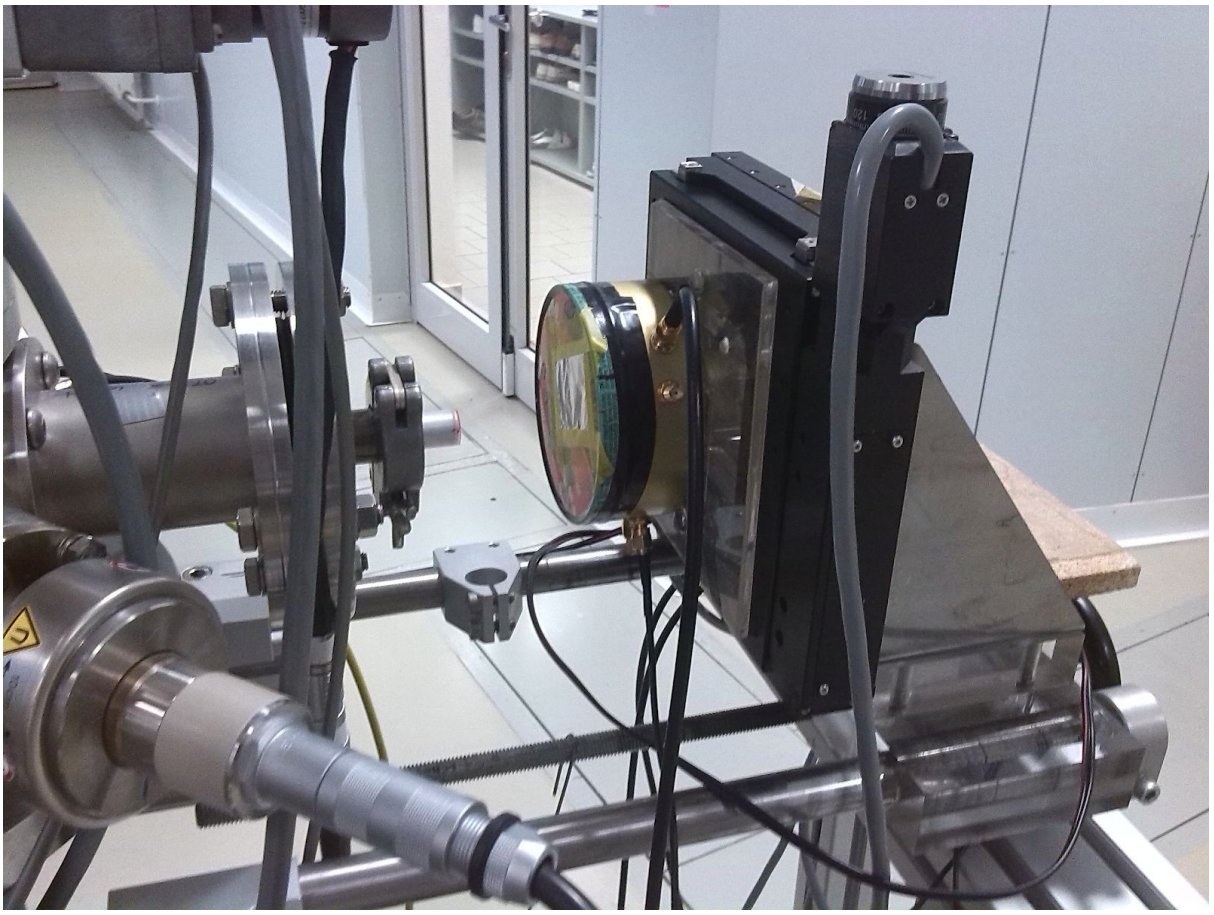

Figure 41*: Proton beam microprobe <0.5 mm in diameter in air, 3 MeV, ~100 protons/s.*

5.2.2. Edge effect

Irradiation of the PIN diode was performed in different positions. Each irradiation lasted as long as necessary for capturing the exact same number of particles by sensor. Histograms of relation of amplitude of pulses and area of pulses obtained at HIMAC setup are shown in figure 42. The results show a strong dependence of energy response on the edge of the sensor. At the very edge of the sensor, there are a lot of events with much lower energy than expected. As beam moves towards the edge of the sensor less particles in the peak (upper region of graphs) and more particles without the correctly measured energy (lower parts of graphs) are detected. We can see from the overview graphs (figure 42) that the ratio of false detections to correct detections in respect of bias voltage is similar. It can be seen from colour of points in upper and bottom regions.

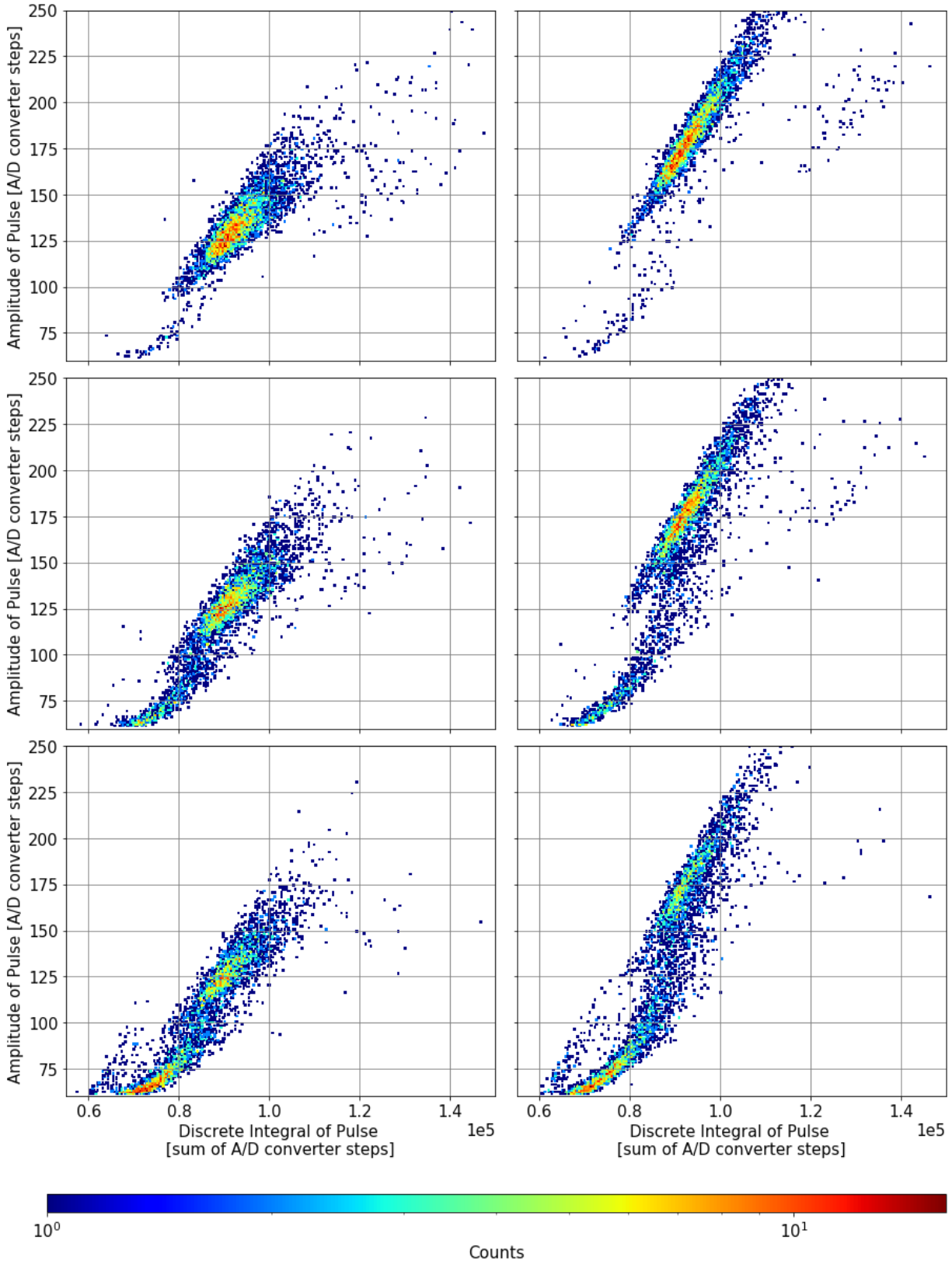

Figure 42*: Overview of edge effect measurements. Depicted histograms are for different positions of beam* 90.2 mm, 89 mm, 87.8 mm *(in rows from top to bottom) and different bias voltage (left column is for 3 V, right column is for 18 V). Each histogram comprises 5080 events from the beam with He nuclei with energy of 230 MeV/u.*

Wideness of the beam and wideness of the edge region when distortion of the signal happens can be seen in graph in figure 43. It can be observed from decreasing of the detected flux near the edge. If we linearly interpolate the measured fluxes we can read from an intersection of interpolation on the x axis that the beam is out of the chip in position 87.4 mm and the thickness of the beam is about 2.5 mm. The beam is homogenous because linear approximation is possible.

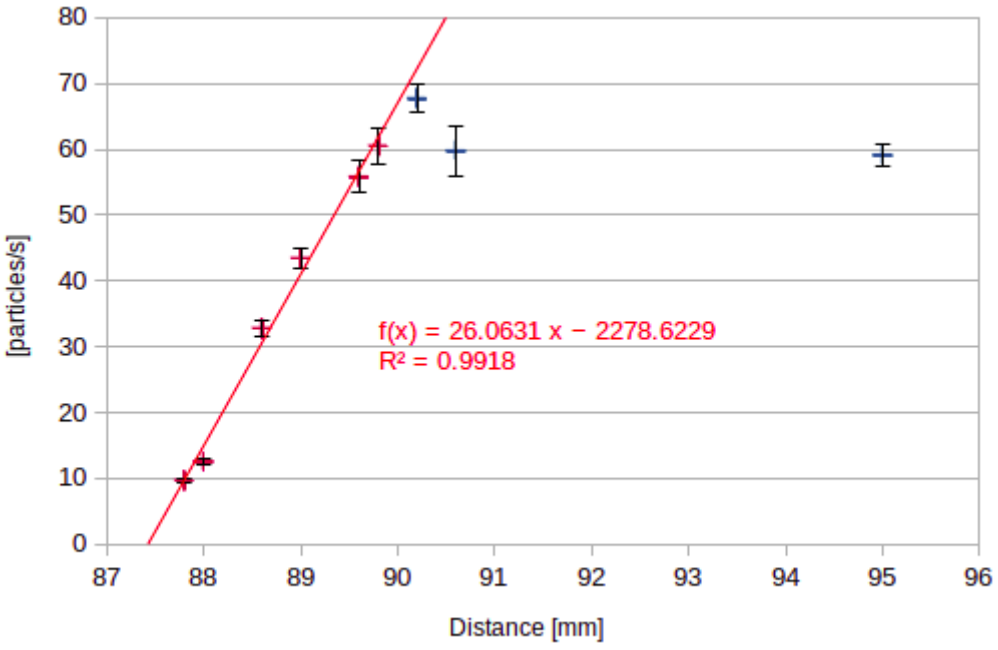

Figure 43*: Dependence of number of detected particles on position of beam. Red points were used for linear interpolation. Blue points belong to the area out of the edge distortion and its surroundings.*

We can divide the obtained histograms into two parts - the region where the particle energy (upper region) is correctly detected and the region where the detection of energy (lower region) was wrong as depicted in figure 44. Then, for each measured position, we can calculate the ratio of false/good detections (ratio between the number of detection in the upper and lower part of graphs). This ratio is plotted in the graph in figure 45. In this graph, we can see that ⅓ of all detections are false in the region of about one millimeter from the edge of the diode.

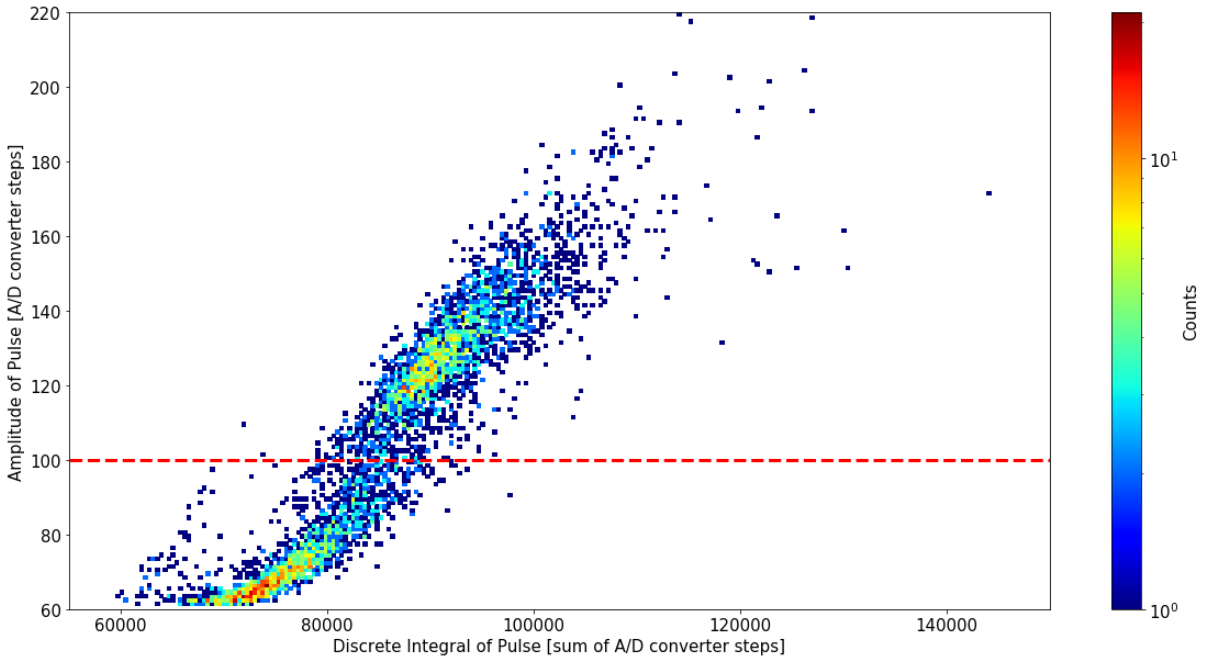

Figure 44*: Histogram of captured events when a beam penetrates the very edge of the sensor. Red dashed line is the chosen threshold between good and false detection of energy.*

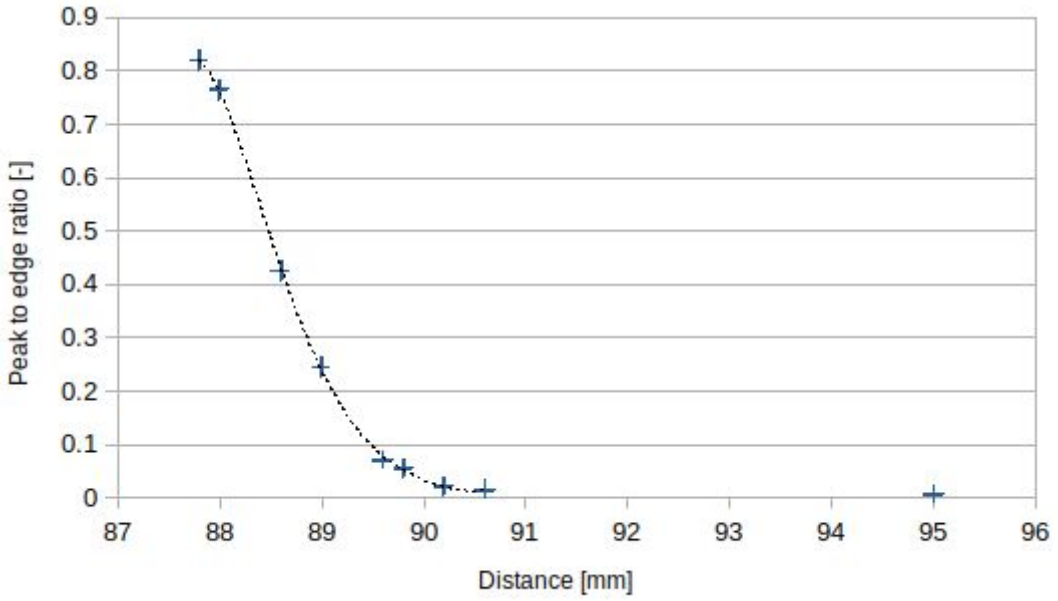

Figure 45*: Ratio between particles with correct and incorrect detected energy. Dashed line is only a spline. Errors were not calculated because the graph shows ratio and we assume that measurement errors are the same for both measured populations and precision in measured distance is greater than resolution of this graph.*

The second experiment was performed at Tandetron accelerator (figure 41) with less than 0.5 thin beam of protons with energy of 3 MeV. Several positions near the edge of the chip were irradiated. We can see in the figure 46 that 1.3 mm from the edge the measured energy is without distortion. We have to take into account that the range of 3 MeV protons in silicon is

about 100 μm. When we move the beam more closely to the edge of the chip we obtained a distorted spectra. These results are in agreement with measurement at HIMAC because in this experiment we measured only in one third of the thickness of the depleted region.

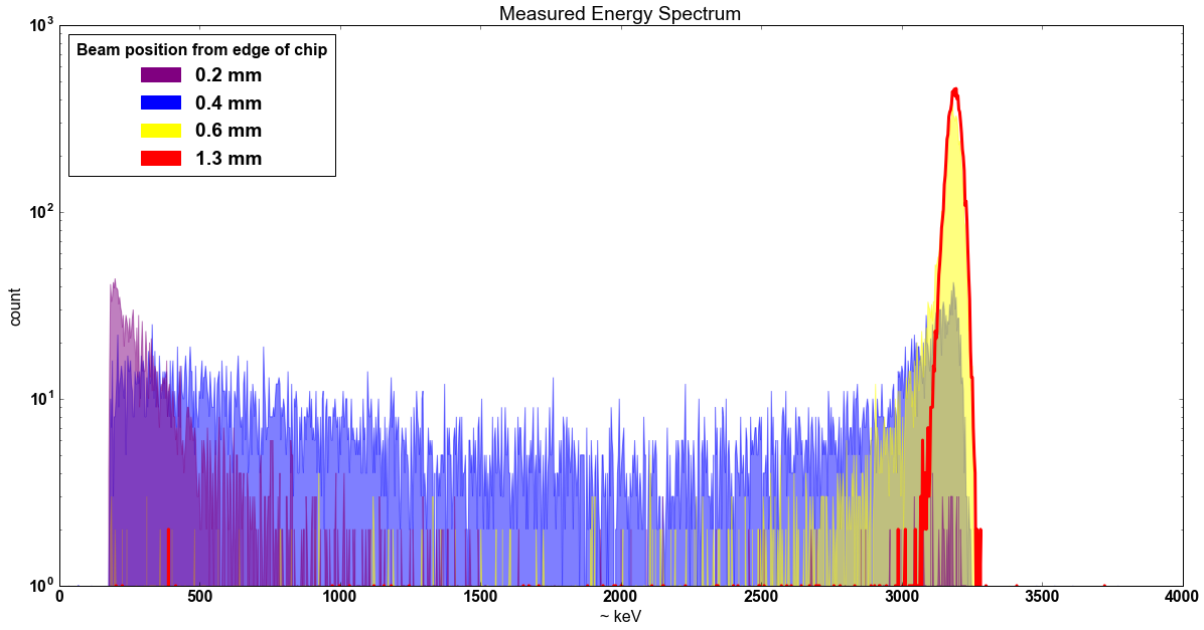

Figure 46*: Spectra obtained at Tandetron. Colour differs depending on the beam position from the edge of the chip. Colours are semi transparent for visibility of overlapped graphs. Red spectrum is depicted only as an outline.*

5.2.3. Conclusion about the sensitive volume versus edge effect

The mass of the sensitive detector volume in literature differs. The sizes of the S2744-09 chip are 21.2 mm X 11.2 mm X 0.3 mm (0.3 mm is the thickness of depleted region taken from Hamamatsu datasheet) and according to (Meier et al. 2016) the whole volume of the diode is considered as sensitive volume. We have shown that this consideration is generally wrong and cca. 16 % of the considered volume must be treated differently. Particles are detected, but their measured energy is significantly lower. This finding suggests that dimensions of sensitive volume 20 mm X 10 mm X 0.3 mm previously used by (Dachev et al. 2002) in Liulin complementary software are more close to the real sensitive volume. We can estimate an error about 8 % in assessment of the dose in silicon if we suppose 50 % decrease in measured energy at the edge region of the diode.

5.2.4. Thickness of entrance window

Knowledge of the thickness of an entrance window (or dead layer) of a solid state sensor is essential for energy calibration performed by ionizing particles with range lower than the thickness of the sensor.

We can use a standard method for determining the thickness of the entrance window described in (Knoll 2000). This method used irradiation with particles with known energy loss irradiated from different angles.

Energy loss in irradiation perpendicular to the surface of diode is given by

$$\Delta E_0 = \frac{dE_0}{dx} t .$$

Where t is the thickness of the dead layer and dE_0/dx is LET for silicon for given particles.

The energy loss for angle θ is given by

$$\Delta E(\theta) = \frac{\Delta E_0}{cos\,\theta} .$$

Therefore, the difference between the measured pulse heights for angles zero and θ is given by

$$E' = \Delta E_0 (\frac{1}{cos\,\theta} - 1) .$$

Finally when we linearly fit the measured energies as a function of (1/cos θ - 1) the slope of this line is equal to ΔE_0 and from this value we can calculate the thickness of the dead layer if we know LET of given particles for silicon.

Dead layer of similar diode from Hamamatsu S3204-09 (this diode has the same parameters and only a larger area than S2744-09) was measured using the described method by (Spencer 2004) and determined to be 122 nm. From previous work cited by (Spencer 2004) the error is ±10 nm.

5.2.5. Thickness of depleted region

Knowledge of thickness of a depleted region is essential for energy calibration performed by ionizing particles with stopping power in silicon less or equal to Bragg's curve plateau for given thickness of sensitive region of a sensor. Dependence of thickness of depleted region on reverse bias voltage was tested with positive ions with enough energy to penetrate the whole thickness of the diode. Bragg peak must lay behind the diode. If we presume that deposited energy depends on the thickness of depleted region and depleted region increases with reverse bias voltage we can observe an increase of deposited energy together with increasing bias voltage.

Diode Hamamatsu S2744-09 has a thickness of depleted region 300 μm as stated in the datasheet. The question is if the thickness of depletion is affected by reverse bias voltage. Using a similar method as for estimation of thickness of dead layer we can measure energy deposited in tilted sensor. The measurement setup is the same as for edge effect measurement (figure 40) only the moving platform is not shifted but tilted. We get dependence of energy depicted in figure 47 with the method used in previous chapter for assessment of the thickness of the entrance window.

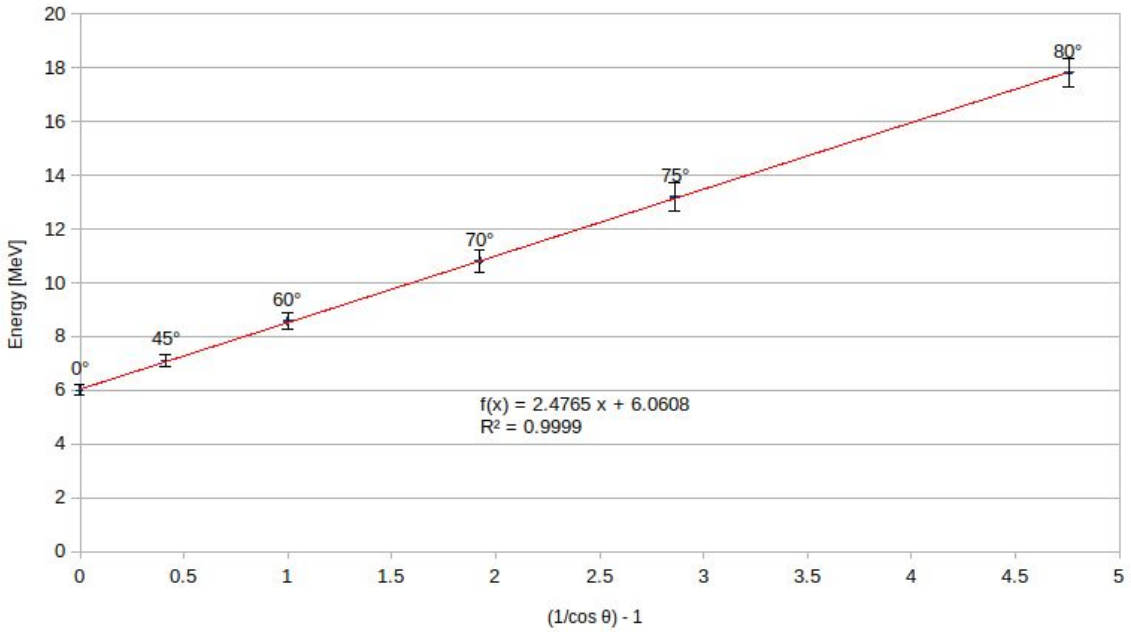

Figure 47*: Dependence of deposited energy on (1/cos θ - 1). Length of path of particles inside a diode depends on an angle θ and the length of path is directly proportional to the deposited energy. Irradiation was performed by carbon nuclei with energy of 380.9 MeV/u.*

For different reverse bias voltages we got different energy responses, the slope of the linear fit was different (figure 48). One can conclude that the thickness of the depleted region depends on the reverse bias voltage. We can do a more precise investigation using the technique described in the chapter 5.1.2. Data processing. Histogram of amplitude and area of pulses are shown in figure 49. Horizontal and vertical cross sections in this histogram are histograms in figure 50 and figure 51. We can see that amplitudes are changing a lot with angle but the area seems to stay very similar.

When we investigate the difference between particular pulses for a specific area we can see from figure 52 that a slight difference is not a characteristic of the diode but an error of measurement. Please compare the captured waveforms in figure 52 beyond 50 μs. There is a feedback capacitor in charge amplifier completely discharged in the case of the black cross section but there is some remaining charge in the case of the red cross section. This remaining charge produces a difference in the area of the pulses.

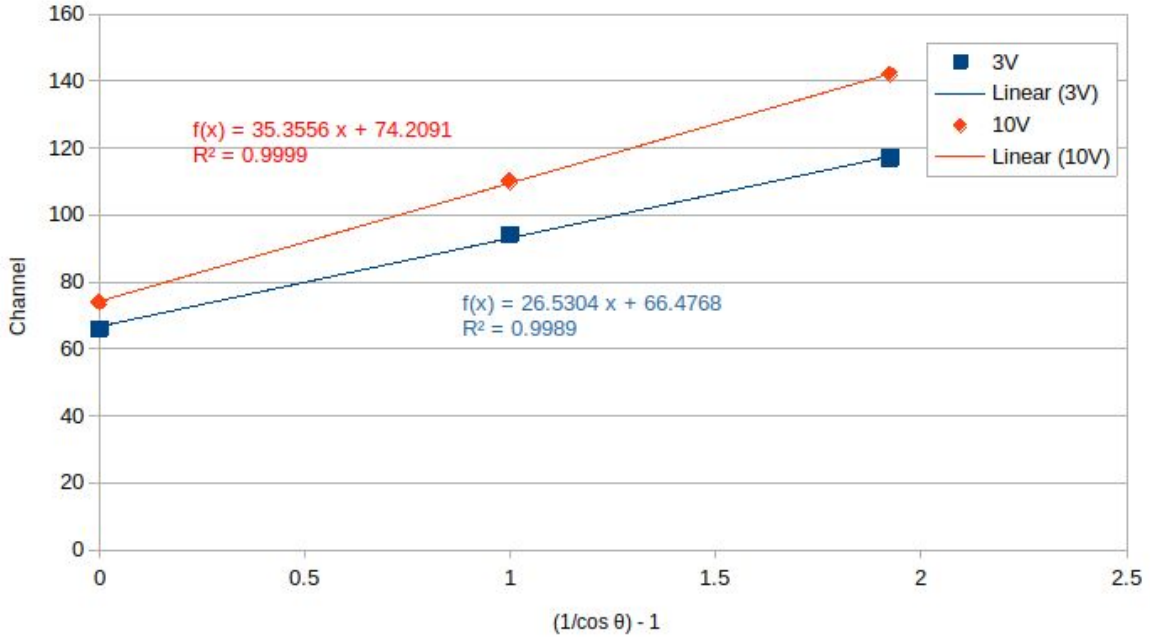

Figure 48*: Different energy response for angles 0°, 60°, 70° (from left to right) and for reverse bias voltages 3 V and 10 V. Irradiation was performed by carbon nuclei with the energy of 380.9 MeV/u. Errors are not depicted because they are evident from next pictures.*

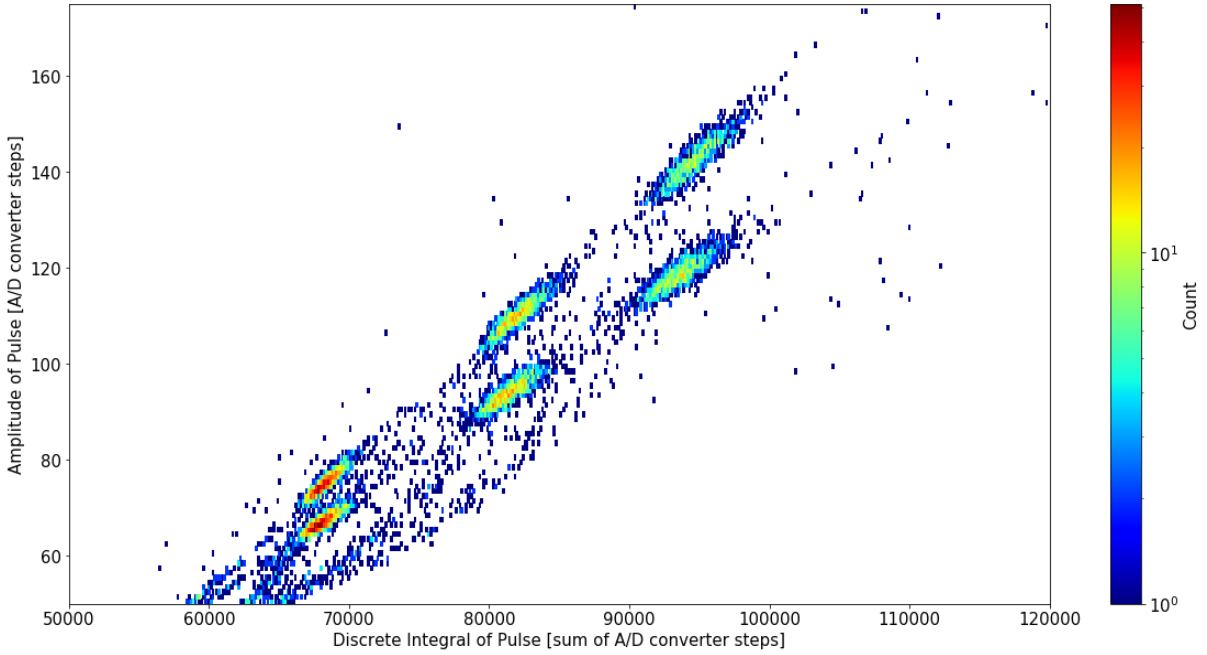

Figure 49*: Histogram of response of detector for different bias voltages and different angles of irradiation. From left to right the peaks correspond to angles 0°, 60° and 70°. Upper peaks correspond to 10 V and lower peaks correspond to 3 V of reverse bias voltage. Please see histograms in* figure 50 *and* figure 51 *for horizontal and vertical cross sections of this graph.*

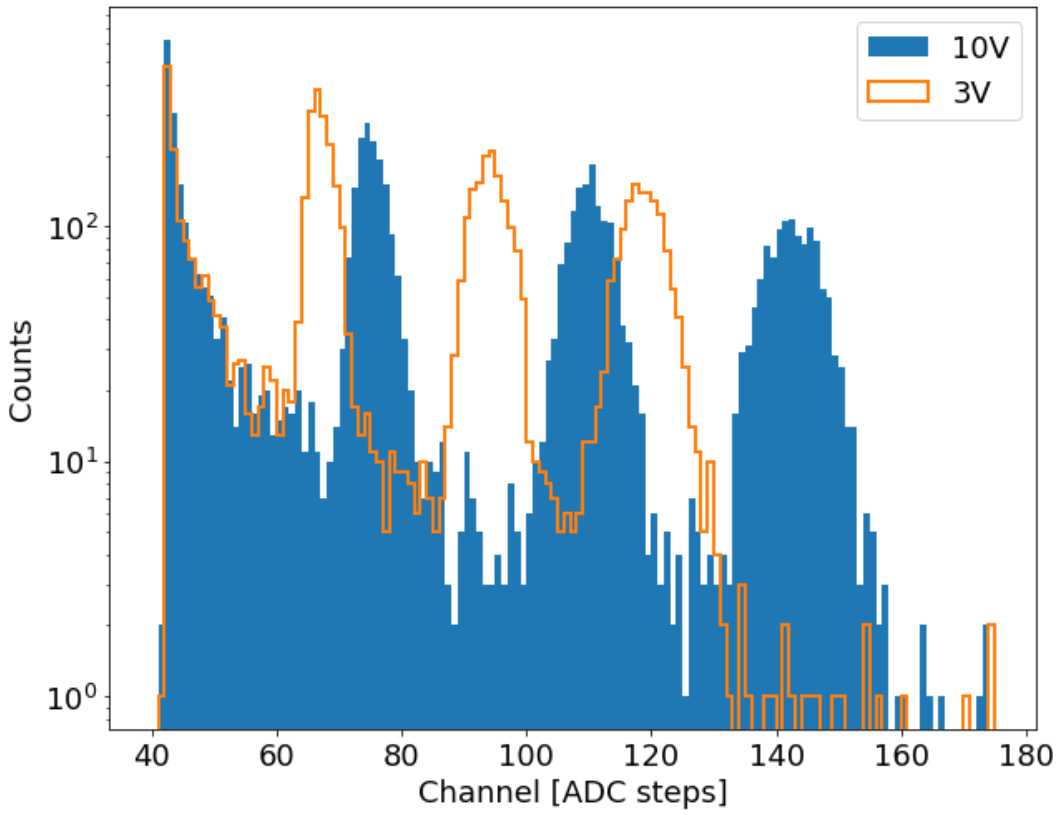

Figure 50*: Histogram of angular response of detector. Amplitude of pulses. From left to right the peaks correspond to angles 0°, 60° and 70°. Blue bars correspond to 10 V and orange steps correspond to 3 V of reverse bias voltage.*

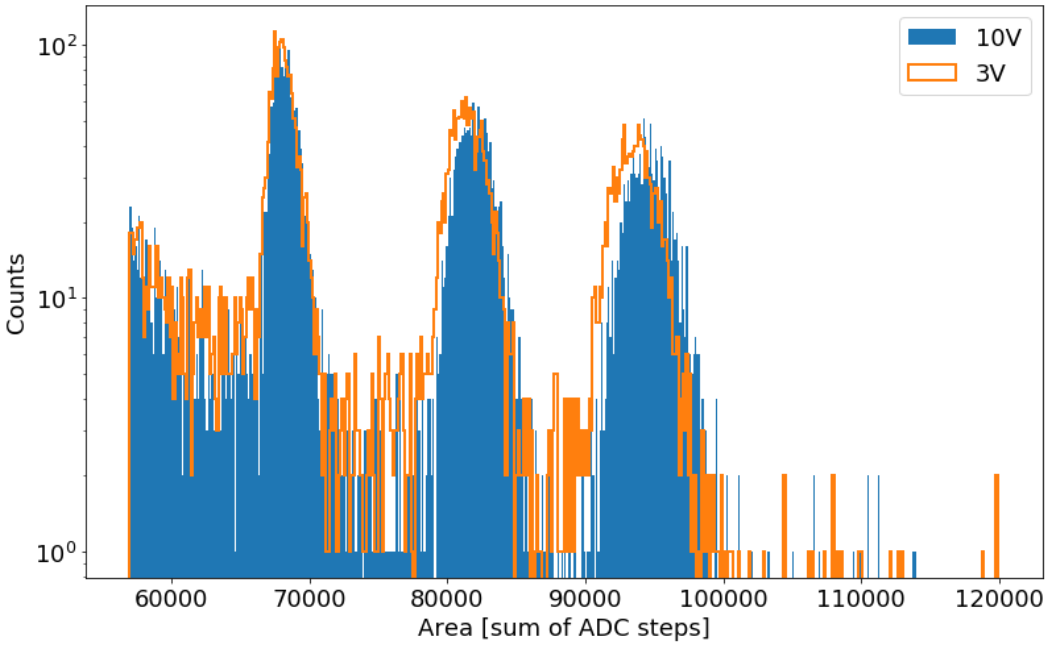

Figure 51*: Histogram of angular response of detector. Area of pulses. From left to right the peaks correspond to angles 0°, 60° and 70°. Blue bars correspond to 10 V and orange steps correspond to 3 V of reverse bias voltage.*

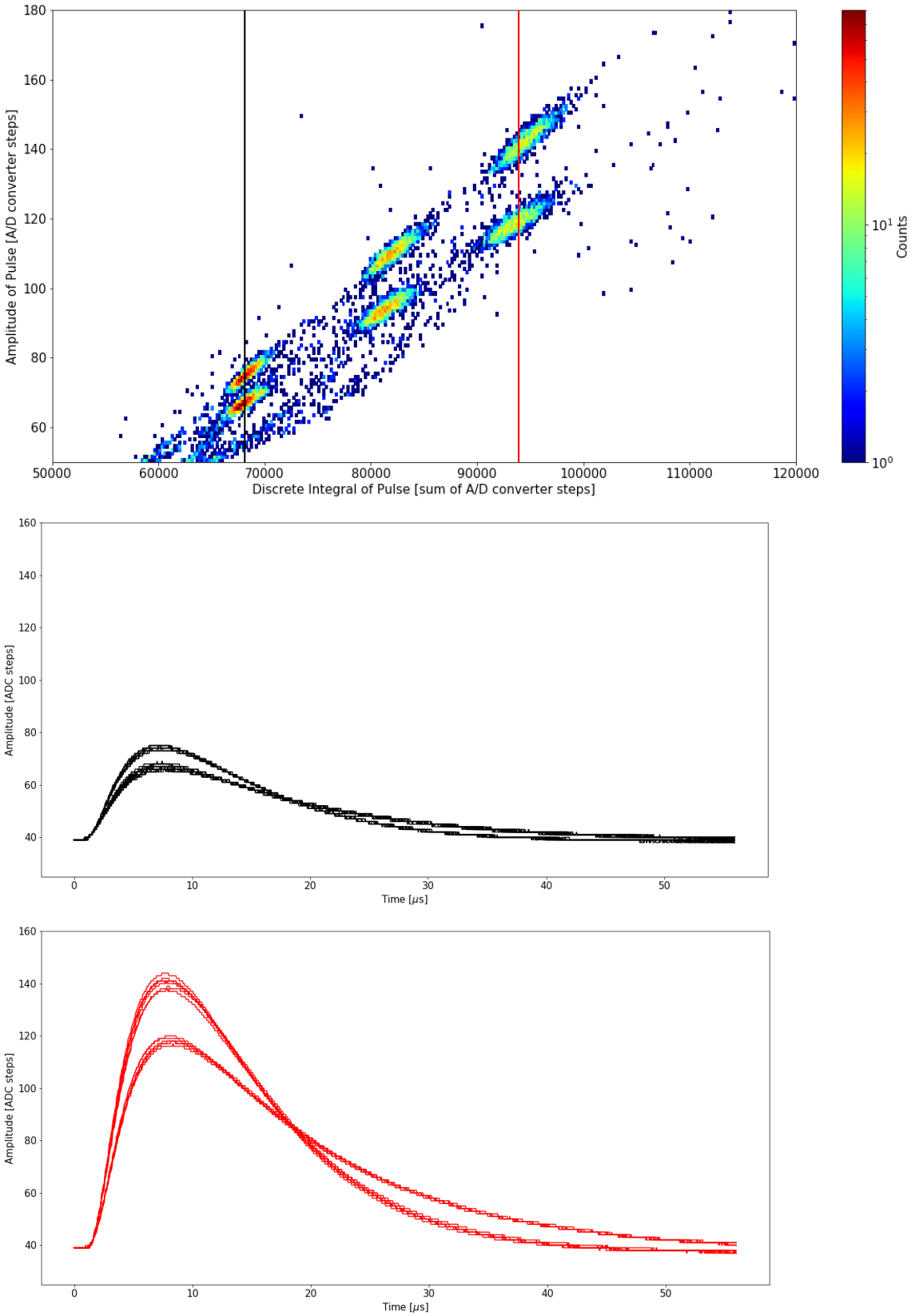

Figure 52*: Cross-section of histogram of angular response for different bias voltages. Depicted pulses are taken from region marked by black and red lines. Area of black pulses is same and analogically area of red pulses is same.*

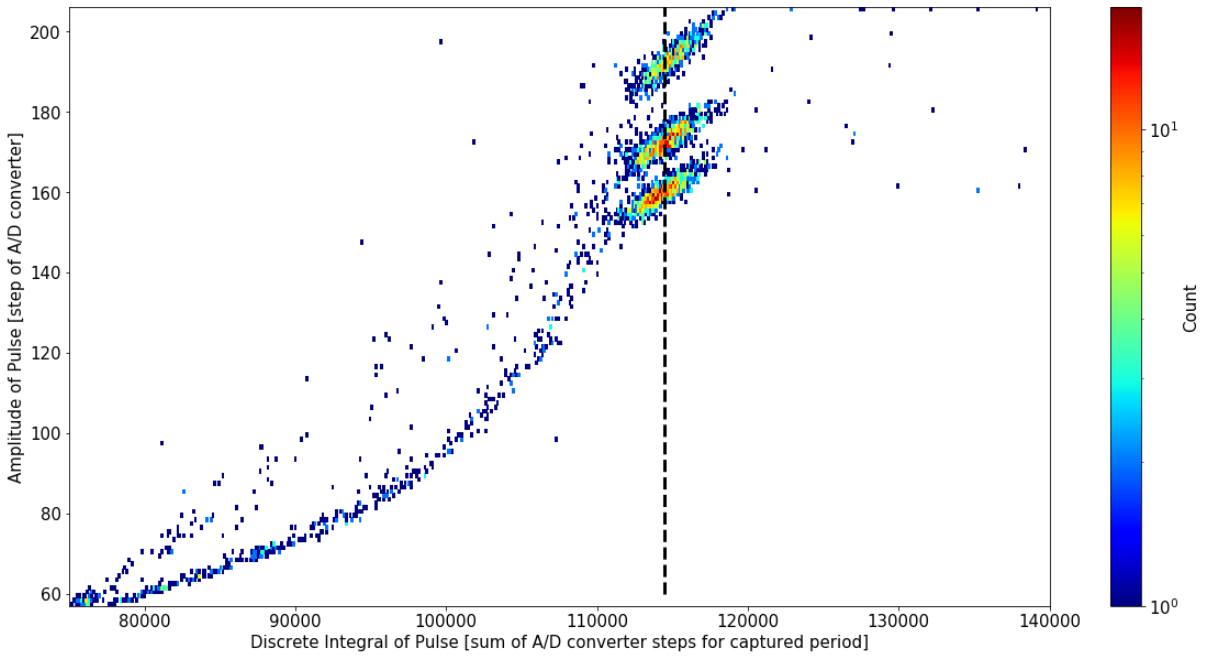

Figure 53*: Test of different reverse bias voltages with irradiation by Si ions with energy 490 MeV/u. Bias voltages are 1.5 V, 3 V and 6 V from the bottom to the top accordingly. Dashed line points to the constant area of pulses.*

Remaining question is if different types of ions or different bias voltages give the same result. It was investigated by different ions with different energies and different reverse bias voltages. An example of this measurement is shown in figure 53.

Figure 53 and figure 52 clearly show that deposited energy (corresponds to the area of pulses) is independent of bias voltage. Increasing reverse bias voltage causes an increase in the amplitude/slope of the pulses. We can conclude from these results that increasing bias voltage does not increase the thickness of the depleted region in the PIN diode, it only causes an increase in the drift force and speeds up the charge carriers.

5.2.6. Volume sensitivity of PIN diode detector

Irradiation of CANDY detector by gamma photons gives different results in contrast to irradiation by positively charged ions mentioned in the previous chapter. It is due to different manners of interaction of photons with matter. Gamma photons interact in random depths of silicon crystal. Experiment, when we irradiate PIN diode with gamma photons, gives histograms in figure 54. There are two clearly visible regions of interaction in the case of the low biasing diode. If we increase the bias voltage, one region stays in the same place (we can call this region “static”) but the other moves towards the static one (we can call this region “moving”). The “static” region holds interactions with lower probability than the “moving” region. With presumption that the gamma photons interact with the same probability in the whole volume of a crystal we can conclude that the “static” region has a smaller volume than “moving”. The ratio between the number of interactions in both regions is the same

independent of the reverse bias voltage. It means that the recorded pulses in the “moving” region only change its shape with respect to the reverse bias voltage.

The results show that both regions do not change their volume, meaning that the thickness of both stays constant (in fact the thickness of the depleted region) independently of the reverse bias voltage. Because of decreasing the charge collection time (increasing the amplitude of pulses with the constant area of pulses) with respect to increasing reverse bias voltage the drift force in “moving” region increases but in “static” region seems to be constant.

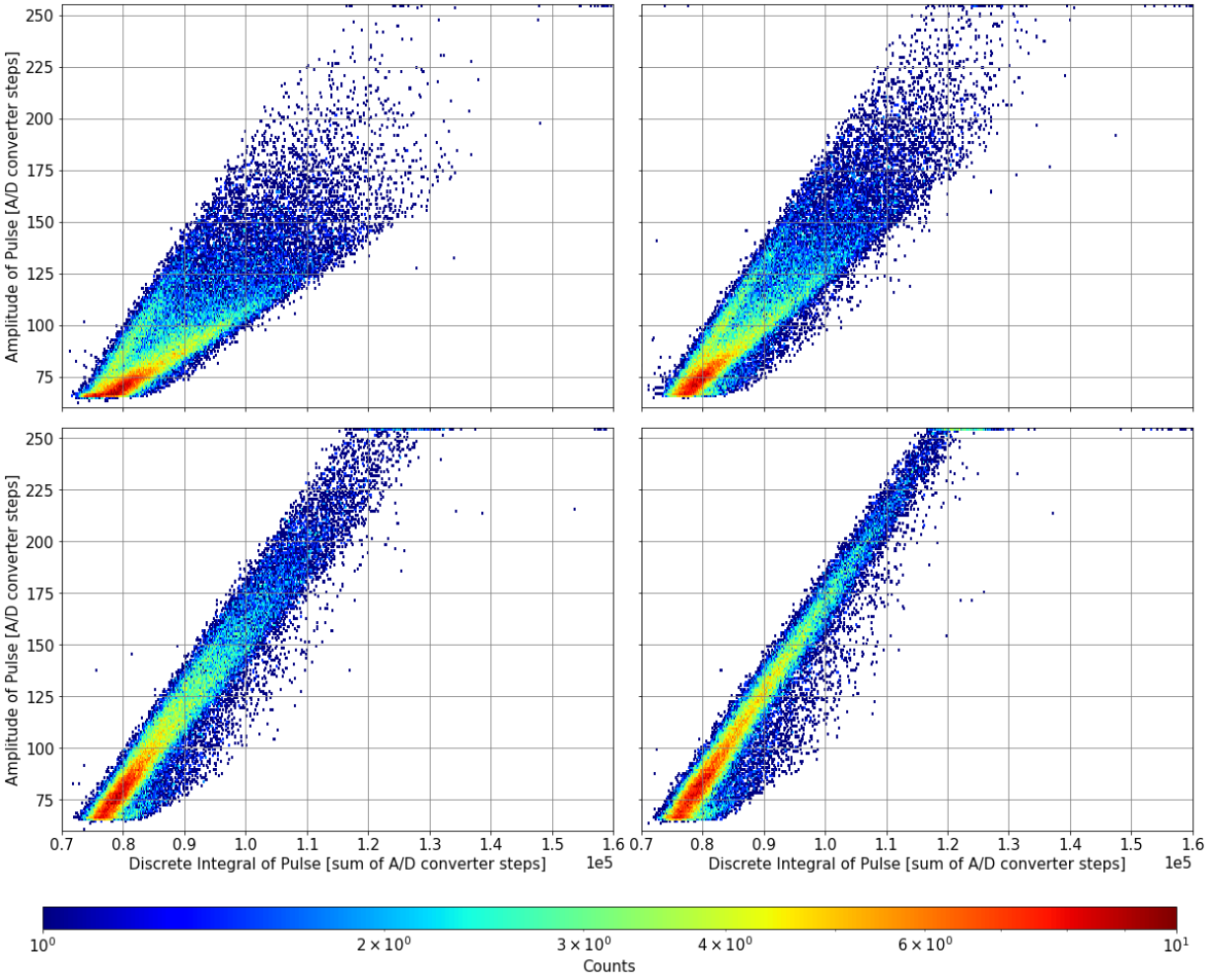

Figure 54*: Irradiation of CANDY detector with gammas from ^{60}Co with different reverse bias voltages (3 V, 10 V, 20 V, 30 V from the left top to bottom right). Each histogram comprises 50800 events.*

We can conclude that there are two regions in PIN diode with different charge collection mechanisms/speed. One region exists in the neighbourhood of PI junction and the second one arrond IN junction. IN region is more than three times thicker than PI region (see figure 55). It is only an estimation from the ratio of events considering both populations of events from the measurements above.

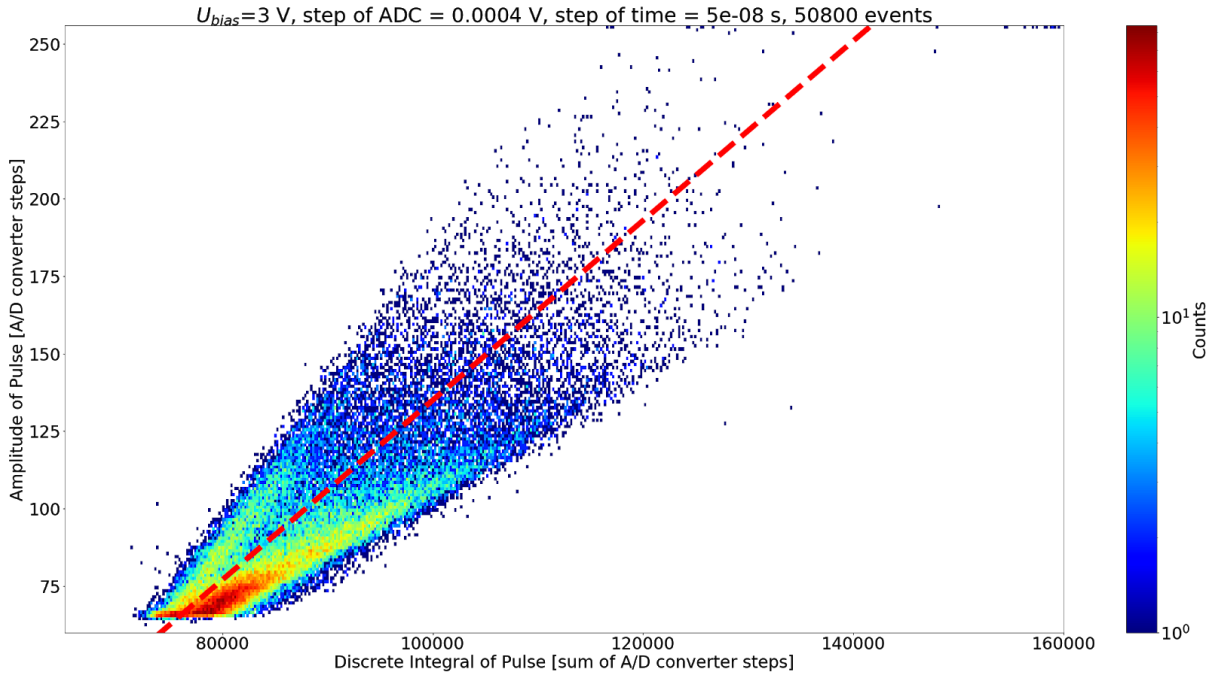

Figure 55*: When we divide the histogram of gamma detection by the red dashed line the depicted ratio between the two populations of events on two sides of the dashed line is 1:3.3 (top:bottom).*

5.2.7. Forward and backward irradiation

Behaviour of PIN diode irradiated by alpha particles from both sides was studied on BPW34 diode and CANDY detector. This diode is manufactured in plastique packaging. For the purpose of the test with alpha particles from radionuclide source this plastique packaging has to be removed by dissolving it in acetone to acquire access to the bare chip. In order to access the surface of the chip from the back side a cuprum electrode has to be etched by $FeCl_3$. The result is displayed in figure 56.

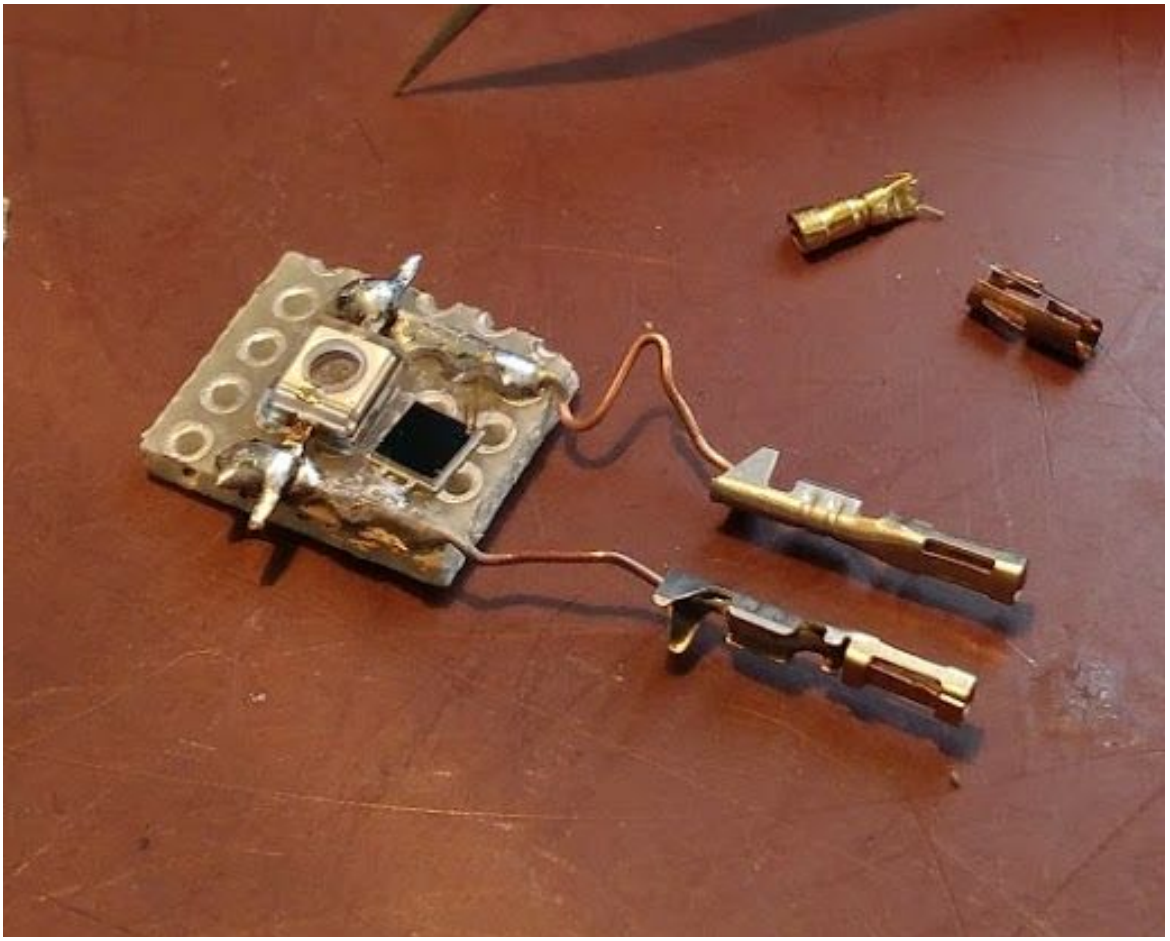

Figure 56*: Two BPW34 PIN diodes. Left side - diode with drilled hole in package and etched electrode from its back side. Right side - diode with removed plastique package. Anode contact is replaced by golden wire. The diodes are connected antiparallel for simultaneous measurement.*

Bare chip was irradiated from both sides with alpha particles with energy around 5 MeV. Two different reverse bias voltages were tested as well. We can see from figure 57 the difference in amplitude of a signal. There is a bigger amplitude in case of irradiation from the front side (anode side) and a lower amplitude in case of irradiation from the back side (cathode side). Dependence on bias voltage is interesting as well. Irradiation from the front side is almost independent of bias voltage opposite to the irradiation from backside where there is a strong dependence on bias voltage.

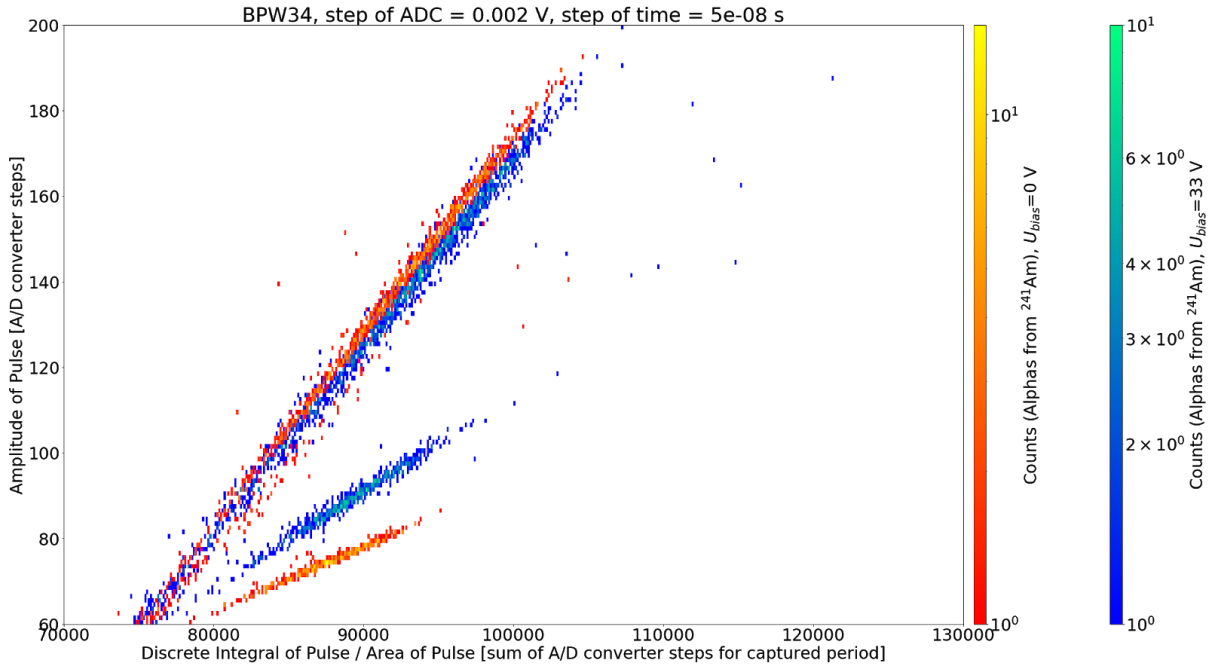

Figure 57*: Forward and backward irradiation of PIN diode with respect to different reverse bias voltages.*

These findings are in agreement with findings obtained from the irradiation of diode by gamma photons. There are two regions with different behavior; one region is close to PI junction and the second one to IN junction. The behavior of charge carriers in PI region is independent of reverse bias voltage. Velocity of charge carriers in IN region increases with increasing reverse bias voltage.

6. Neutrons conversion

Silicon diodes are not practically capable of directly detecting the neutrons because of a very low cross section of silicon for interaction with neutrons. Nevertheless the usage of silicon diode with an appropriate radiator/converter (^{10}B, ^{6}Li, ^{3}He, ^{157}Gd) is possible. See figure 58 for cross sections of nuclides for neutron capture.

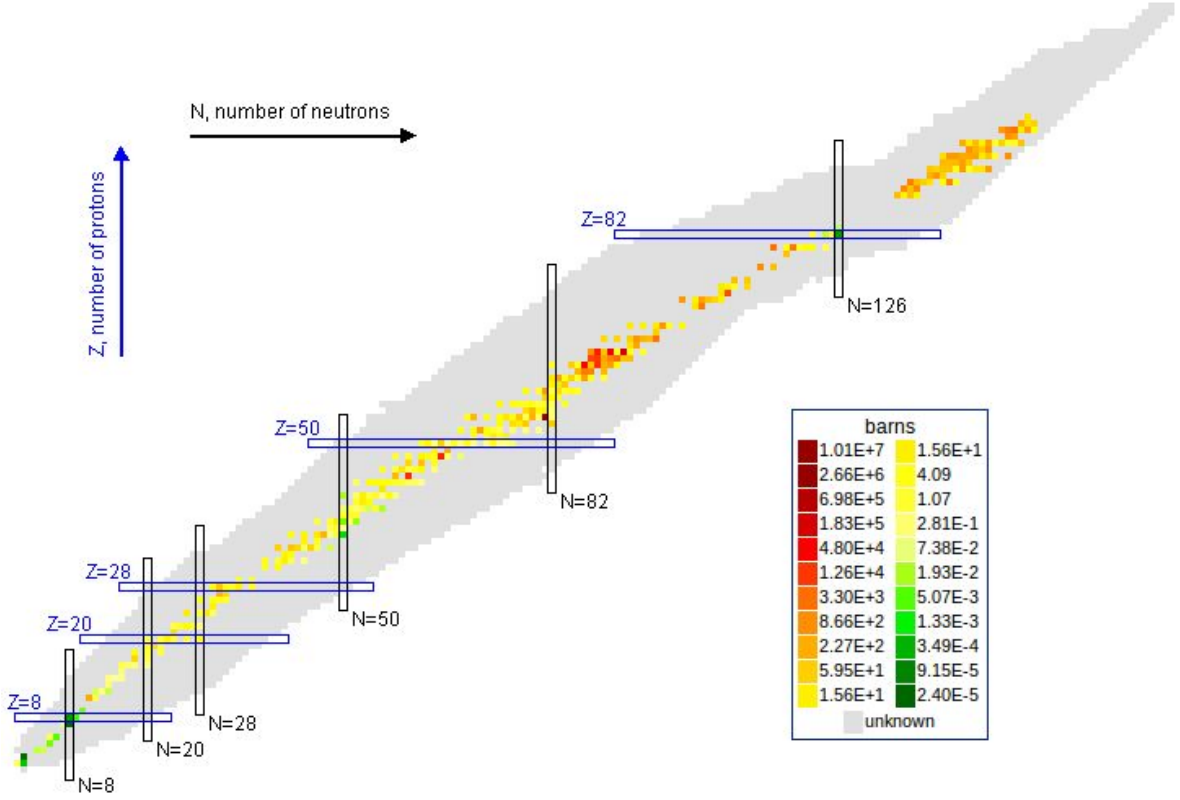

Figure 58*: Table of cross section of known nuclides for neutron capture. Values are for thermal neutrons. (National Nuclear Data Center/Brookhaven National Laboratory 2011)*

For instance a ^{10}B was proposed in (Tomov et al. 2008). Usage of ^{10}B depends on reaction ^{10}B(n,α)^{7}Li.

$^{10}B + n_{thermal} \rightarrow {}^{11}B^* \rightarrow \alpha$ [1.47 MeV] + ^{7}Li* [0.84 Mev] ; $^{7}Li^* \rightarrow {}^{7}Li + \gamma$ [0.48 MeV] 94 %

$^{10}B + n_{thermal} \rightarrow {}^{11}B^* \rightarrow \alpha$ [1.78 MeV] + ^{7}Li [1.02 Mev] 6 %

Cross section for the capture of thermal neutron in ^{10}B is about 4000 barns and the reaction described in the upper equation occurs in 94 % of cases.

If we are thinking about a more complex field as on board aircraft there is a big amount of photons accompanied by neutrons and other particles as well. We can eliminate these particles by appropriate shielding or by decreasing the thickness of the detection diode. However, decreasing of thickness increases the capacity of the diode and thus noise in the front end electronics is increased as well. At the same time, we also want to detect photons on board of aircraft. However, this task requires a thick diode and therefore a method for particle

distinction between neutrons and photons will be more suitable than mere suppression of gamma particles.

We tested a method for particle characterization proposed above with a combination of the ^{10}B radiator.

6.1. Practical setup of neutrons conversion

Figure 59 shows a practical setup of a detector with a ^{10}B radiator and a silicon PIN diode. Bare chip of Silicon PIN diode S2744-09 is covered by a thin ^{10}B film BE10 manufactured by DOSIRAD company. This film consists of 100 µm of PET carrier and 60 µm of enriched boron layer containing >90 % of the ^{10}B. The electronics and the method of signal discrimination are the same as was described in chapter 5.1. CANDY detector. This method (Kákona et al. 2018) can distinguish between alpha particles from the radiator originating in reaction $^{10}B(n,\alpha)^{7}Li$ and photons from ambient radiation field. The energy of alpha particles from the described reaction is about 1.5 MeV. Therefore these particles are capable of penetrating the silicon in a range of few micrometers. Also, the boron foil must be sufficiently thin because LET inside the boron layer is 200 - 300 keV/µm.

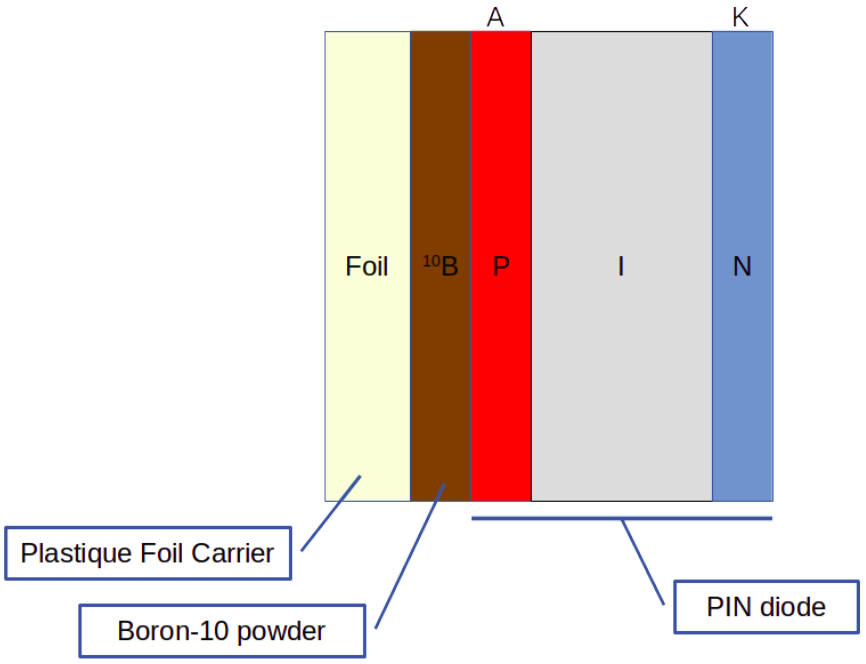

Figure 59*: Mechanical arrangement of detector. Foil with ^{10}B is closely connected to PIN diode.*

Irradiation was performed with an AmBe source which was put inside HDPE (High Density PolyEthylene) sphere 300 mm in radius in order to thermalize the neutrons. The experimental setup is depicted in figure 60.

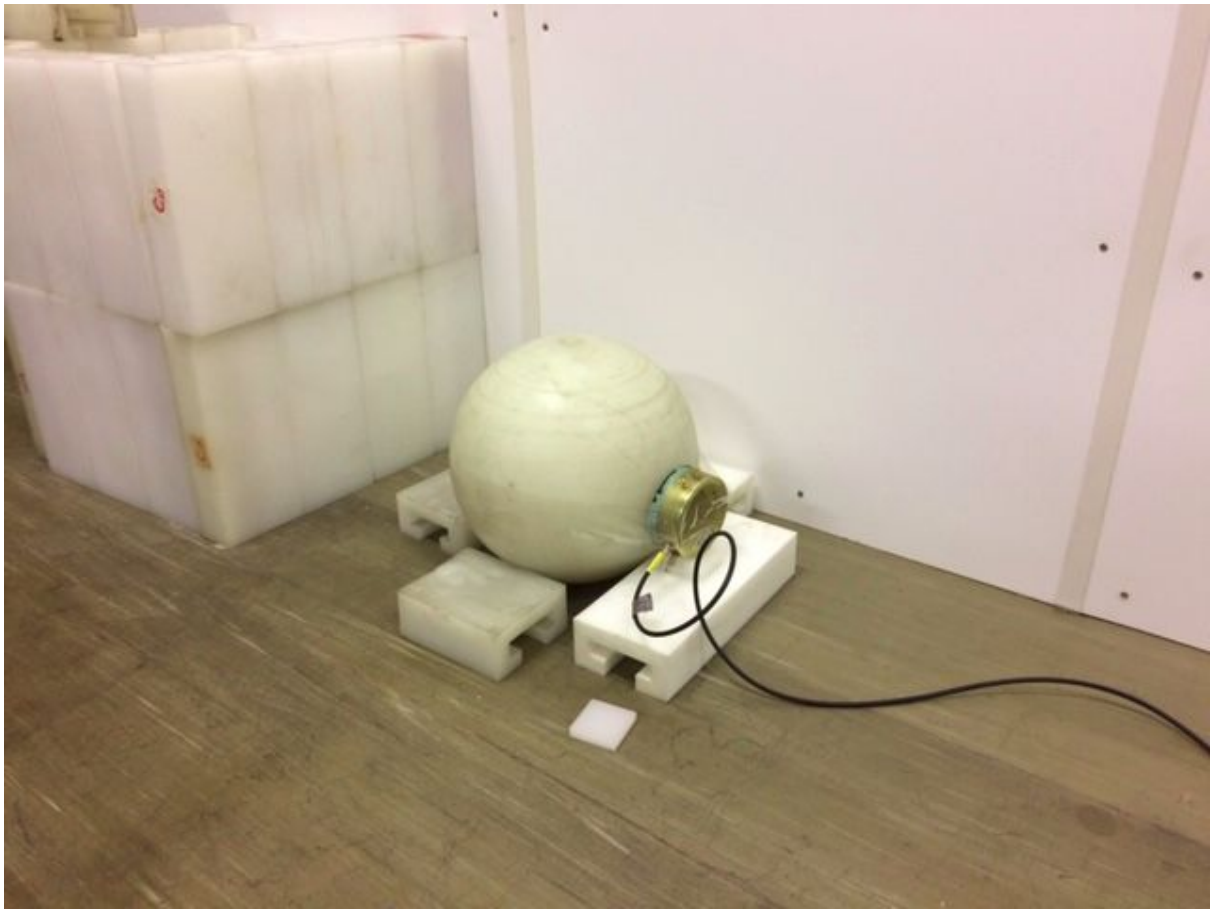

Figure 60*: Irradiation of CANDY detector with an AmBe source placed inside HDPE sphere 300 mm in radius.*

6.2. Results of neutron conversion

First, the sensor was irradiated without a ^{10}B foil. Irradiation lasted 6530 s and 36576 events were recorded (figure 61). These events were due to gamma photons because the silicon detector is not inherently sensitive to neutrons. Then the sensor was covered with a ^{10}B foil during irradiation. That exposure lasted 6497 s and 87376 particles were recorded (figure 62). The difference in detection is 50800 events which must be due to neutrons. If we apply filtering to events by proposed pulse-shape analysis, 46722 events are due to neutrons (figure 63). Filtering is done around a depicted red dashed line. All events above the threshold (5 ADC channels which correspond to 6 mV below the dashed line) are encountered. The red dashed line is fitted to samples in the region from 120 to 200 in the vertical axis and below 120000 in the horizontal axis occurring within the first 600 s of irradiation with the ^{10}B.

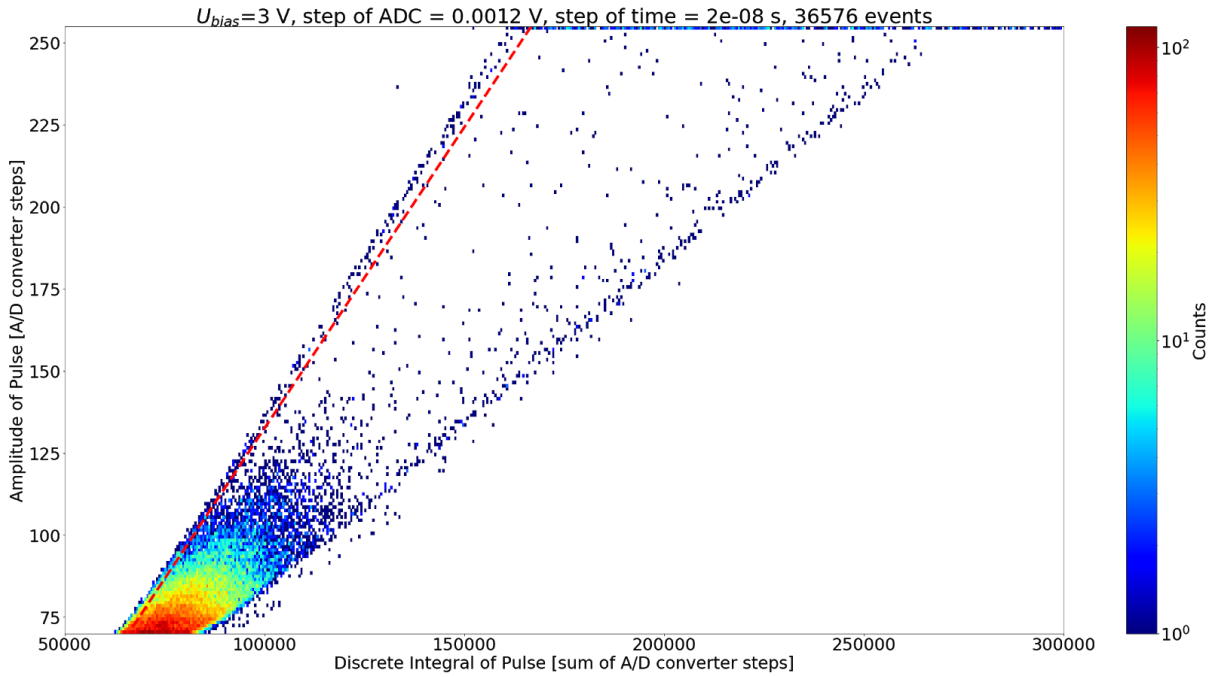

Figure 61*: Irradiation without ^{10}B.*

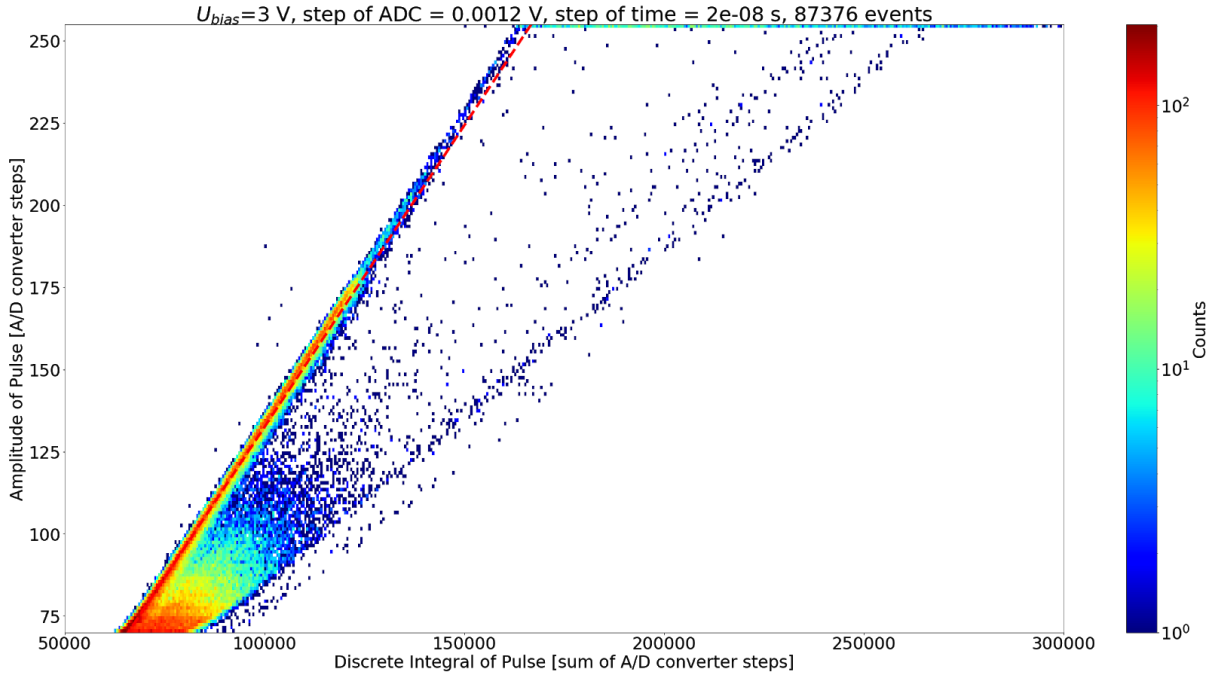

Figure 62*: Irradiation with a ^{10}B foil attached to the surface of a PIN diode.*

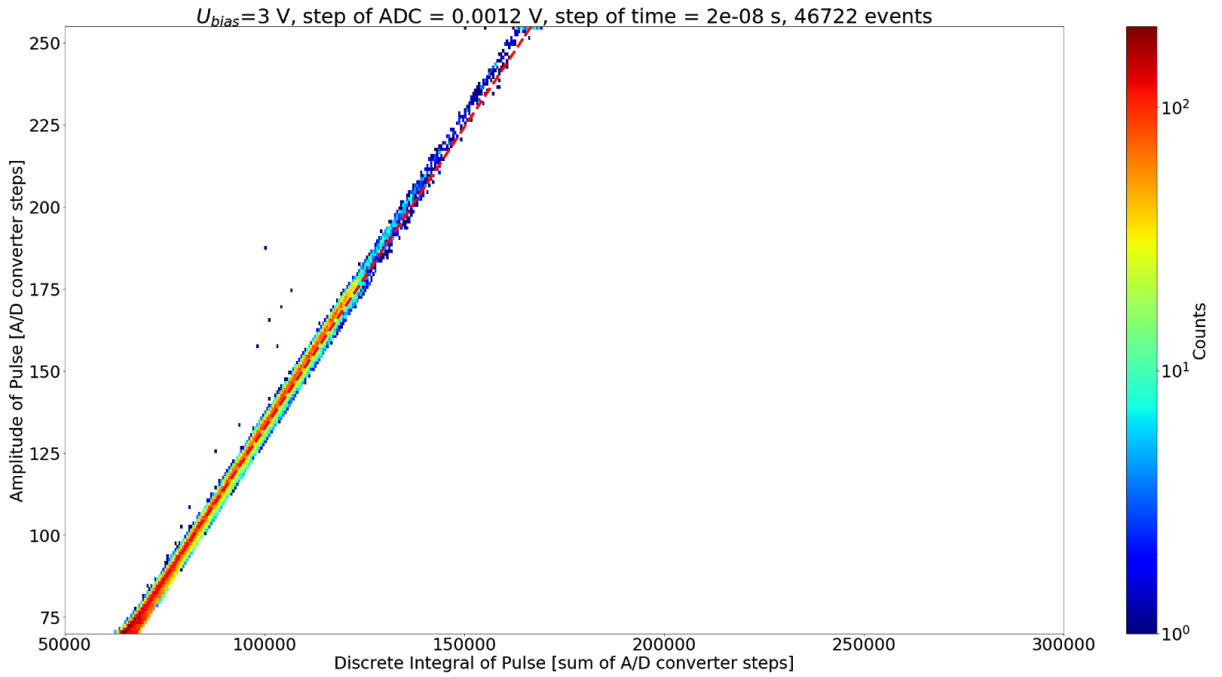

Figure 63*: Irradiation with ^{10}B with an application of a proposed filtering alphas/neutrons procedure.*

6.3. Discussion about detection of neutrons

If we normalize the number of particles per second we get 5.6 events per second for irradiation without the ^{10}B foil and 13,4 events per second in the case of irradiation with the ^{10}B foil. From this, there are 5.6 s^{-1} photons and 7.8 s^{-1} alphas/neutrons detected in the field (with given conversion and detection efficiency). Filtering gives 7.2 s^{-1} neutrons. We can conclude simply from the difference of obtained neutrons rates that an error in the characterisation of photons and neutrons with the proposed method is about 8 % (0.6 s^{-1} difference in our case).

6.4. Conclusion about neutrons conversion

The proposed method of neutron detection is feasible nevertheless the efficiency of this method was tested only with a source of thermal neutrons (where crosssection of the proposed radiator is high). The thermalization of neutrons on board aircraft is a hard task due to energies in ones of MeV and hundreds of MeV. A large volume of a moderator is needed and it is practically feasible only for neutrons in the region of ones of MeV. An aircraft fuel may have suitable characteristics and volume for efficient neutron moderation in such a range of energies. For higher energies, different radiators/converters have to be used. This is additional work that had not been done by the author of this thesis.

7. Conclusions

At the beginning of this work, an influence of short term solar activity to intensity of secondary cosmic ray was studied on historical data measured by Liulin dosimeter on board aircraft. The results are described in papers (Kákona, Kyselová, et al. 2019; Kákona et al. 2016). During this work, some discrepancies in long term measurements with silicon PIN diode dosimeters on board aircraft were discovered by the author of this thesis. Then a new open-source silicon PIN diode dosimeter (AIRDOS) was developed with a novel peak/sample-hold circuit. This dosimeter has some unique features:

A. The newly introduced design of dosimeter (AIRDOS) does not need calibration after manufacturing and recalibration during a lifetime within an error of 15 % in dose.
B. Treatment of low energy channels in AIRDOS dosimeter is done in post-processing. AIRDOS dosimeter stores all measured spectra including noise therefore we can look at measured data (including noise) in different manners anytime in the future.
C. Power consumption during a signal integration is 10 mW only. It guarantees half year uninterruptible operation on batteries.

During the design work, a lot of experiments were performed to better understand the principles of silicon PIN diode detectors. New properties of PIN diode detectors were discovered with practical influence on the design of new types of detectors and on practical usage of PIN diode detectors for better characterization of mixed radiation field on board aircraft, namely:

D. The sensitive volume of the PIN diode was assessed more precisely.
E. Influence of reverse bias voltage to the thickness of the depleted region was found negligible.
F. The new method of characterization of particles by (slow) pulse shape analysis with a PIN diode was introduced.
G. The new method of recognition of neutrons in a mixed neutron-photon field with a single PIN diode was proposed and laboratory tested with significantly good resolution.

Points A and B solved the discrepancies discovered in the beginning of the work. Point D can explain differences in conversion factors for converting a dose in silicon to an ambient dose equivalent which we can find in literature sources. Points E, F, and G open a new field in research of PIN diode detectors.

With experiences from an AIRDOS development new open-source dosimeters for space were developed SPACEDOS 01 (Kákona and Chroust 2019a) and SPACEDOS 02 (Kákona and Chroust 2019b). The first one (SPACEDOS 01) was successfully launched in July 2019 on board satellite SOCRAT R and commissioning in November 2019. Projected length of this mission is one and half year. This dosimeter was redesigned from AIRDOS with respect to its use in a vacuum environment and is capable of providing measurements on an orbit during passing through the inner Van Allen radiation belt. The second one (SPACEDOS 02) was successfully launched in September 2019 on board Soyuz MS-15 with a crew expedition 61 to

the ISS (International Space Station). The scheduled return of this dosimeter is at the beginning of the year 2020.

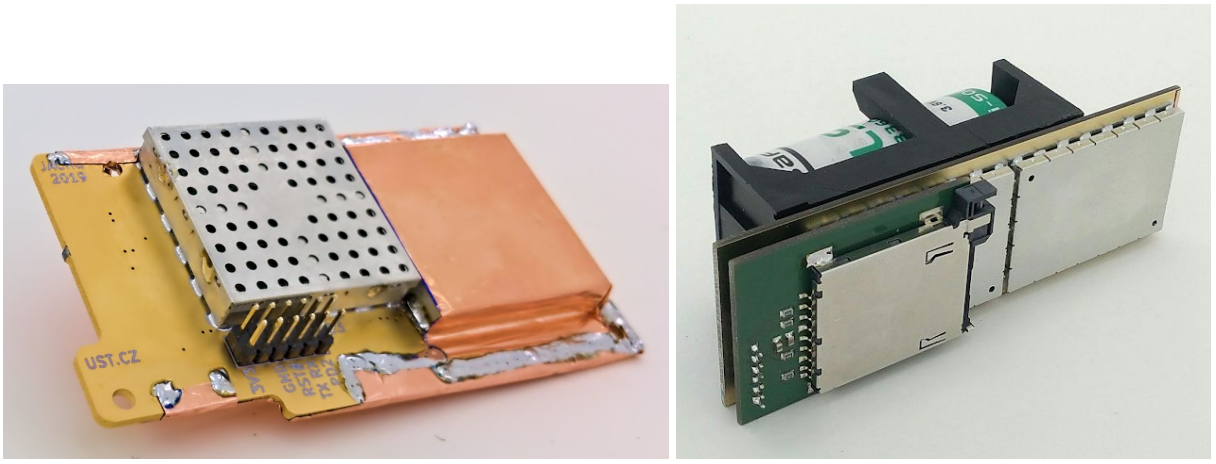

Figure 64*: SPACEDOS 01 (left) and SPACEDOS 02 (right). These dosimeters are intended for measurement of radiation on board satellites. SPACEDOS 01 is designed for a vacuum environment and SPACEDOS 02 is designed for manned space flights and for measuring radiation in a crew cabin.*

Future work can focus on better use of the newly introduced sample-hold circuit in the AIRDOS design and utilization of this circuit for signal discrimination for proposed and laboratory tested pulse-shape analysis. It opens new abilities for signal treatment. The new sample-hold circuit can be used for detecting a falling edge of signal when the signal starts falling just after a peak. This seems to be a better approach than a comparison of signal with some small voltage threshold which has to be inherently noisy.

Bibliography

Alig, R.C. and Bloom, S. 1975. Electron-Hole-Pair Creation Energies in Semiconductors. *Physical Review Letters* 35(22), pp. 1522–1525.

Ammerlaan, C.A.J., Rumphorst, R.F. and Koerts, L.A.C. 1963. Particle identification by pulse shape discrimination in the p-i-n type semiconductor detector. *Nuclear Instruments and Methods* 22, pp. 189–200.

Bottollier-Depois, J.F., Trompier, F., Clairand, I., et al. 2004. Exposure of aircraft crew to cosmic radiation: on-board intercomparison of various dosemeters. *Radiation Protection Dosimetry* 110(1–4), pp. 411–415.

Copeland, K. 2017. Cari-7a: development and validation. *Radiation Protection Dosimetry* 175(4), pp. 419–431.

Copeland, K., Friedberg, W., Duke, F., et al. 2017. CARI 7 [Online]. Available at: https://www.faa.gov/data_research/research/med_humanfacs/aeromedical/radiobiology/cari7/ [Accessed: 8 December 2019].

Dachev, T.P., Matviichuk, Y.N., Semkova, J.V., et al. 1989. Space radiation dosimetry with active detections for the scientific program of the second Bulgarian cosmonaut on board the MIR space station. *Advances in Space Research* 9(10), pp. 247–251.

Dachev, T., Dimitrov, P., Tomov, B. and Matviichuk, Y. 2001. TECHNICAL DESCRIPTIONOF LIULIN-4 TYPE LET SPECTROMETERS (LETS) . . Available at: http://citeseerx.ist.psu.edu/viewdoc/download?doi=10.1.1.504.2611&rep=rep1&type=pdf [Accessed: 10 December 2019].

Dachev, T., Dimitrov, P., Tomov, B. and Matviichuk, Y. 2009. Technical Description of the Spectrometer-Dosimeter Liulin-6C MDU-6.

Dachev, T., Tomov, B., Matviichuk, Y., et al. 2002. Calibration results obtained with Liulin-4 type dosimeters. *Advances in Space Research* 30(4), pp. 917–925.

Dyer, C., Lei, F., Hands, A. and Truscott, P. 2007. Solar particle events in the qinetiq atmospheric radiation model. *IEEE Transactions on Nuclear Science* 54(4), pp. 1071–1075.

Evenson, P., Garcia-Munoz, M., Meyer, P. and Simpson, J.A. 1981. The cosmic ray electron/proton intensity ratio between 1965 and 1979. In: Gif-sur-Yvette, Essonne, France, Commissariat a l'Energie Atomique, pp. 246–249.

FAA 2019. Heliocentric potential [Online]. Available at: https://www.faa.gov/data_research/research/med_humanfacs/aeromedical/radiobiology/heliocentric/ [Accessed: 1 January 2020].

Far West Technology, Inc. 2010. "HAWK" TEPC ENVIRONMENTAL MONITOR MODEL FW-AD1 [Online]. Available at: https://www.fwt.com/detector/fw-ad1ds.htm [Accessed: 1 January 2020].

Firoz, K.A., Cho, K.S., Hwang, J., et al. 2010. Characteristics of ground-level enhancement-associated solar flares, coronal mass ejections, and solar energetic particles. *Journal of Geophysical Research* 115(A9).

Forbush, S.E. 1993. Solar influences on cosmic rays. In: Van Allen, J. A. ed. *Cosmic rays, the sun and geomagnetism: the works of scott E. forbush*. Washington, D. C.: American Geophysical Union, pp. 237–250.

Forbush, S.E., Stinchcomb, T.B. and Schein, M.B. 1993. The extraordinary increase of cosmic-ray intensity on November 19, 1949. In: Van Allen, J. A. ed. *Cosmic rays, the sun and geomagnetism: the works of scott E. forbush*. Washington, D. C.: American Geophysical Union, pp. 177–180.

GNU 2007. GNU General Public License v. 3.0 [Online]. Available at: https://www.gnu.org/licenses/gpl-3.0.en.html [Accessed: 8 January 2020].

HAMAMATSU 2011. PIN photodiode S2744-09 [Online]. Available at: https://www.hamamatsu.com/resources/pdf/ssd/s2744-08_etc_kpin1049e.pdf [Accessed: 9 December 2019].

ICRP 1997. ICRP Publication 75. General Principles for the Radiation Protection of Workers. *Annals of the ICRP* 27(1).

ICRP 2007. ICRP Publication 103, The 2007 Recommendations of the International Commission on Radiological Protection. *Annals of the ICRP*.

ICRU 2010a. Reference Data for the Validation of Doses from Cosmic-Radiation Exposure of Aircraft Crew. ICRU Report 84 (prepared jointly with ICRP). *Journal of the ICRU* 10(1), p. NP.1-NP.

ICRU 2010b. Report 84. *Journal of the ICRU* 10(2), p. NP-NP.

ISO 2015. *ISO 20785-3:2015. Dosimetry for exposures to cosmic radiation in civilian aircraft — Part 3: Measurements at aviation altitudes*.

Kákona, M. 2019. AIRDOS data format [Online]. Available at: https://github.com/ODZ-UJF-AV-CR/AIRDOS01/wiki/AIRDOS-data-format [Accessed: 1 January 2020].

Kákona, M. 2017. AIRDOS data parser [Online]. Available at: https://github.com/ODZ-UJF-AV-CR/AIRDOS-parser [Accessed: 1 January 2020].

Kákona, M. 2018a. AIRDOS Firmware [Online]. Available at: https://github.com/ODZ-UJF-AV-CR/AIRDOS02/tree/AIRDOS02A/sw [Accessed: 1 January 2020].

Kákona, M. 2016. Oscilloscope driver [Online]. Available at: https://github.com/ODZ-UJF-AV-CR/osciloskop/tree/USB [Accessed: 1 January 2020].

Kákona, M. 2018b. PCRD04B [Online]. Available at: https://github.com/MLAB-project/Modules/tree/master/sensors/PCRD04B [Accessed: 1 January 2020].

Kákona, M. and Chroust, J. 2018a. AIRDOS02 [Online]. Available at: https://github.com/ODZ-UJF-AV-CR/AIRDOS01 [Accessed: 1 January 2020].

Kákona, M. and Chroust, J. 2018b. DATALOGGER01A [Online]. Available at: https://github.com/MLAB-project/Modules/tree/master/sensors/DATALOGGER01A [Accessed: 1 January 2020].

Kákona, M. and Chroust, J. 2019a. SPACEDOS 01 [Online]. Available at: https://github.com/ODZ-UJF-AV-CR/SPACEDOS01 [Accessed: 5 January 2020].

Kákona, M. and Chroust, J. 2019b. SPACEDOS 02 [Online]. Available at: https://github.com/UniversalScientificTechnologies/SPACEDOS02 [Accessed: 5 January 2020].

Kákona, M., Chroust, J., Kákona, J., et al. 2017. AIRDOS01 [Online]. Available at: https://github.com/ODZ-UJF-AV-CR/AIRDOS01 [Accessed: 1 January 2020].

Kákona, M., Krist, P. and Štěpán, V. 2018. A method to determine the type of ionising radiation using a semiconductor diode and a circuit for carrying out this method. Patent number: CZ307570.

Kákona, M., Kyselová, D., Ambrožová, I., et al. 2019. CR10 - a public database of cosmic radiation measurements at aviation altitudes of about 10 km. *Radiation Protection Dosimetry*.

Kákona, M., Ploc, O., Kyselová, D., Kubančák, J., Langer, R. and Kudela, K. 2016. Investigation on contribution of neutron monitor data to estimation of aviation doses. *Life Sciences in Space Research* 11, pp. 24–28.

Kákona, M., Štěpán, V., Ambrožová, I., et al. 2019. Comparative measurements of mixed radiation

fields using liulin and AIRDOS dosimeters. In: AIP Conference Proceedings. Author(s), p. 130003.

Keim, R. 2018. Understanding and Implementing Charge Amplifiers for Piezoelectric Sensor Systems [Online]. Available at: https://www.allaboutcircuits.com/technical-articles/understanding-and-implementing-charge-amplifiers-for-piezoelectric-sensor-s/ [Accessed: 1 January 2020].

Knoll, G.F. 2000. Entrance Window or Dead Layer. In: *Radiation Detection and Measurement*. 3rd ed. John Wiley & Sons., Inc., p. 386.

Křížek, F., Ferencei, J., Matlocha, T., et al. 2018. Irradiation setup at the U-120M cyclotron facility. *Nuclear Instruments and Methods in Physics Research Section A: Accelerators, Spectrometers, Detectors and Associated Equipment* 894, pp. 87–95.

Kubančák, J., Kyselová, D., Kovář, I., et al. 2019. Overview of aircrew exposure to cosmic radiation in the czech republic. *Radiation Protection Dosimetry*.

Kudela, K. and Langer, R. 2009. Cosmic ray measurements in High Tatra mountains: 1957–2007. *Advances in Space Research* 44(10), pp. 1166–1172.

Lappetito, L. 2017. Si-PIN Photodiode β Detector [Online]. Available at: http://physicsopenlab.org/2017/04/28/si-pin-photodiode-%CE%B2-detector/ [Accessed: 1 January 2020].

Lillhök, J., Beck, P., Bottollier-Depois, J.F., et al. 2007. A comparison of ambient dose equivalent meters and dose calculations at constant flight conditions. *Radiation Measurements* 42(3), pp. 323–333.

Lindborg, L., Beck, P., Bottolier-Depois, J.F., et al. 2007. Determinations of H(10) and its dose components onboard aircraft. *Radiation Protection Dosimetry* 126(1–4), pp. 577–580.

Lindborg, L., Kyllonen, J.E., Beck, P., et al. 1999. The use of TEPC for reference dosimetry. *Radiation Protection Dosimetry* 86(4), pp. 285–288.

Linear Technology 2006. LTC6244 datasheet.

Mares, V., Maczka, T., Leuthold, G. and Rühm, W. 2009. Air crew dosimetry with a new version of EPCARD. *Radiation Protection Dosimetry* 136(4), pp. 262–266.

Meier, M.M. and Matthiä, D. 2019. Dose assessment of aircrew: the impact of the weighting factors according to ICRP 103. *Journal of Radiological Protection : official journal of the Society for Radiological Protection* 39(3), pp. 698–706.

Meier, M.M., Trompier, F., Ambrozova, I., et al. 2016. CONCORD: comparison of cosmic radiation detectors in the radiation field at aviation altitudes. *Journal of Space Weather and Space Climate* 6, p. A24.

Microchip 2018. ATmega164A/PA/324A/PA/644A/PA/1284/P. (ISBN: 978-1-5224-3637-9).

MLAB 2003. MLAB project [Online]. Available at: https://mlab.cz/ [Accessed: 8 January 2020].

National Nuclear Data Center/Brookhaven National Laboratory 2011. Neutron capture cross section [Online]. Available at: https://en.wikipedia.org/wiki/Neutron_capture#/media/File:Chart_of_Nuclides_-_Thermal_neutron_capture_cross_sections.png [Accessed: 1 January 2020].

NMDB 2020. Neutron monitor database [Online]. Available at: http://www.nmdb.eu/ [Accessed: 9 January 2020].

Ploc, O., Ambrozova, I., Kubancak, J., Kovar, I. and Dachev, T.P. 2013. Publicly available database of measurements with the silicon spectrometer Liulin onboard aircraft. *Radiation Measurements* 58, pp. 107–112.

Poluianov, S.V., Usoskin, I.G., Mishev, A.L., Shea, M.A. and Smart, D.F. 2017. GLE and Sub-GLE

Redefinition in the Light of High-Altitude Polar Neutron Monitors. *Solar Physics* 292(11), p. 176.

Processing Foundation 2001. Processing language [Online]. Available at: https://processing.org/ [Accessed: 9 January 2020].

Reitz, G. 1993. Radiation environment in the stratosphere. *Radiation Protection Dosimetry*.

Roesler, S., Heinrich, W. and Schraube, H. 1998. Calculation of radiation fields in the atmosphere and comparison to experimental data. *Radiation Research* 149(1), p. 87.

Romanenko, O., Havranek, V., Mackova, A., et al. 2019. Performance and application of heavy ion nuclear microbeam facility at the Nuclear Physics Institute in Řež, Czech Republic. *The Review of scientific instruments* 90(1), p. 013701.

Silari, M. and Pozzi, F. 2017. The CERN-EU high-energy Reference Field (CERF) facility: applications and latest developments. *EPJ Web of Conferences* 153, p. 03001.

Simpson, J.A. 1983. Elemental and Isotopic Composition of the Galactic Cosmic Rays. *Annual Review of Nuclear and Particle Science* 33(1), pp. 323–382.

Spencer, T. 2004. Improving Resolution for the KATRIN Detector Prototype.

Spieler, H. 2012. Silicon Detectors. *IEEE 2012 Nuclear Science Symposium, Medical Imaging Conference*.

Spurný, F. and Dachev, T. 2003. Long-term monitoring of the onboard aircraft exposure level with a Si-diode based spectrometer. *Advances in Space Research* 32(1), pp. 53–58.

Spurný, F., Ploc, O. and Jadrníčková, I. 2009. Spectrometry of linear energy transfer and dosimetry measurements onboard spacecrafts and aircrafts. *Physics of Particles and Nuclei Letters* 6(1), pp. 70–77.

Spurný, F., Ploc, O., Jadrníčková, I., Turek, K., Dachev, T. and Gelev, M. 2007. Monitoring of onboard aircraft exposure to cosmic radiation: May–December 2005. *Advances in Space Research* 40(11), pp. 1551–1557.

Tobiska, W.K., Atwell, W., Beck, P., et al. 2015. Advances in atmospheric radiation measurements and modeling needed to improve air safety. *Space weather : the international journal of research & applications* 13(4), pp. 202–210.

Tobiska, W.K., Bouwer, D., Smart, D., et al. 2016. Global real-time dose measurements using the Automated Radiation Measurements for Aerospace Safety (ARMAS) system. *Space weather : the international journal of research & applications* 14(11), pp. 1053–1080.

Tomov, R., Venn, R., Owens, A. and Peacock, A. 2008. Development of a portable thermal neutron detector based on a boron rich heterodiode. In: Owen, G. ed. *Optics and Photonics for Counterterrorism and Crime Fighting IV*. SPIE Proceedings. SPIE, p. 71190H.

Uchihori, Y., Kitamura, H., Fujitaka, K., et al. 2002. Analysis of the calibration results obtained with Liulin-4J spectrometer-dosimeter on protons and heavy ions. *Radiation Measurements* 35(2), pp. 127–134.

Vishay 2019. BPW34 [Online]. Available at: https://www.vishay.com/docs/81521/bpw34.pdf [Accessed: 9 December 2019].

Wissmann, F. and Klages, T. 2019. A simple method to monitor the dose rate of secondary cosmic radiation at altitude. *Journal of Radiological Protection : official journal of the Society for Radiological Protection* 39(1), pp. 71–84.

Yamada, S. 1995. Commissioning and performance of the HIMAC medical accelerator. In: *Proceedings Particle Accelerator Conference*. IEEE, pp. 9–13.

Ziegler, J.F. 2010. SRIM [Online]. Available at: http://www.srim.org/index.htm [Accessed: 5 January

2020].

Ziegler, J.F., Ziegler, M.D. and Biersack, J.P. 2010. SRIM – The stopping and range of ions in matter (2010). *Nuclear Instruments and Methods in Physics Research Section B: Beam Interactions with Materials and Atoms* 268(11–12), pp. 1818–1823.

Attachment A

Radiation Protection Dosimetry (2019), pp. 1–5 doi:10.1093/rpd/ncz207

CR10—A PUBLIC DATABASE OF COSMIC RADIATION MEASUREMENTS AT AVIATION ALTITUDES OF ABOUT 10 KM

Martin Kákona[1,2,*], Dagmar Kyselová[1,2], Iva Ambrožová[1], Ján Kubančák[1], Václav Štěpán[1], Ronald Langer[1,3], Karel Kudela[1,3,†] and Ondřej Ploc[1]
[1]Nuclear Physics Institute of the Czech Academy of Sciences, Prague, Czech Republic
[2]Faculty of Nuclear Sciences and Physical Engineering, Czech Technical University in Prague, Prague, Czech Republic
[3]Institute of Experimental Physics, Košice, Slovakia

*Corresponding author: kakona@ujf.cas.cz

[†]Prof. Ing. Karel Kudela, Dr.Sc. unexpectedly passed away on the 20th January 2019

Long-term measurements using silicon radiation spectrometer Liulin on board commercial aircraft have been performed since 2001; results were put into a new database, which covers more than 4500 flights with more than 130 000 measurements. Methodology and tools were developed to normalize the data with respect to latitude and altitude and thus enable comparison with other radiation detectors and with model calculations. This capability is demonstrated using data from the neutron monitor at Lomnický štít. Instead of providing data files for individual measurement period, two software solutions are delivered. First is a web-based user interface for visualizing and downloading arbitrary time window of interest from the database hosted at http://cr10.odz.ujf.cas.cz. The second is a set of interactive Python notebooks available at GitHub. Those implement the calibration, normalization and visualization methods—so the outputs can be tailored to user needs. The software and data are provided under GNU/CC license.

INTRODUCTION

Although the radiation field due to galactic cosmic radiation is rather constant and can be well described by various calculation codes, variations caused by effects such as solar energetic particle events (leading to FD—Forbush decrease or GLE—ground level enhancement) need to be verified experimentally. For that reason, long-term measurements onboard aircraft are essential. The used instruments are carefully calibrated in reference fields and cross-calibrated with other instruments. The long-term performance is checked against count rates delivered from neutron monitor (Lomnický štít—LMKS, http://www.nmdb.eu/). This allows the user to compare the exposure level during different times in the solar cycle and during GLEs. The measured data can also be used to verify model calculations.

Since 2001, NPI (Nuclear Physics Institute of the CAS) performs continuous measurements with Liulin, a silicon diode-based dosemeter[(1)] permanently placed onboard aircraft[(2)]; some of these data were already made available in a previous database[(3)]. However, the data in that database are just data from separate measurement campaigns and access to the data can be done only for given measurement periods.

For a better access and use of the data, a novel user interface was introduced for data selection. This new interface was established as a response to new requests for an improved data evaluation. A user can compare on board dosimetry data measured with NPI Liulin with count rates obtained from the neutron monitor over a selected period. This gives scientists an overview of the available data. For selected time slots, the data can be downloaded. Scripts are provided to allow detailed investigation of that data.

New data from the year 2011 to the beginning of the year 2017 were added. The new CR10 database comprises now more than 130 thousand individual records of energy deposition spectra, absorbed dose rates and calculated ambient dose equivalent rates and navigational data obtained from more than 4000 flights. Calculated ambient dose equivalent rates plotted over the world map and over all the data are shown in Figure 1.

The description of the development of this new online database is described and some examples of its use are shown in this paper.

METHODS

Data Origin

The data published in the CR10 database were measured by three different Liulin mobile dosimetry units (MDUs): Liulin MDU-5[(4)], Liulin MDU-6[(5)] and Liulin MDU-7. Details regarding the measurement periods of these three instruments are listed in Table 1.

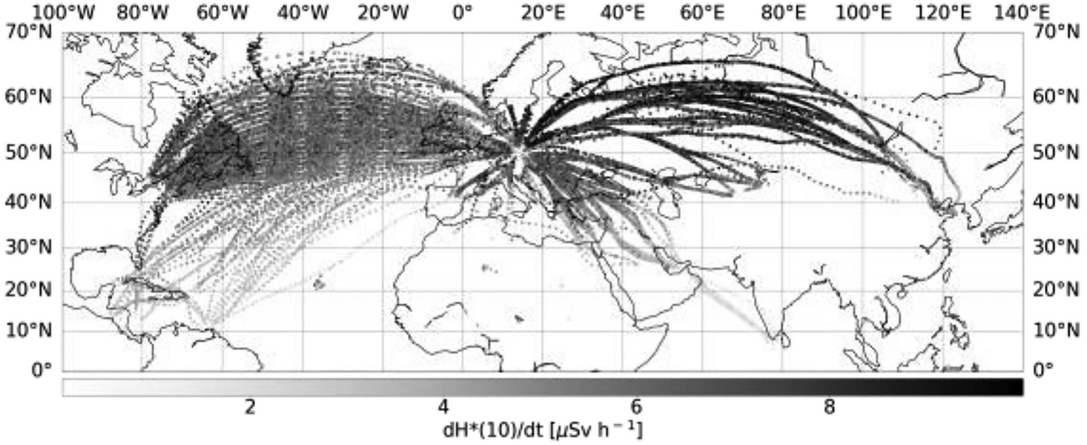

Figure 1. Scatter plot of ambient dose equivalent rates measured aboard aircraft plotted over the world map. This figure contains 10 minute averages for all data published via the CR10 database.

Table 1. Time periods of measurements with different Liulin models.

From	To	Liulin model	Serial no.
2001-03-22	2008-09-22	MDU5	4C
2009-05-19	2013-02-03	MDU6	6C
2013-07-17	2018	MDU7	6C

Measurements with Liulin MDUs have been carried out in collaboration with Czech Airlines during the commercial flights since 2001. The exposures were performed in measurement periods lasting about 3 months each, sometimes followed by a few weeks or months break for a dosemeter maintenance or calibration. More information about the Liulin and its use for measurements onboard aircraft is given elsewhere[3].

Data Visualization

The values of absorbed dose in silicon measured at aircraft altitudes are dependent on geomagnetic coordinates, altitude and solar activity. For displaying the data on a screen, some normalizations are provided. It includes linear approximations of count rates obtained from Liulin measurements in dependence of latitude and altitude as displayed in Figure 2. Note that this correlation is done for geographic not geomagnetic latitude based on data obtained from the airline. In addition, it is assumed that the geomagnetic field is constant during 16 years of the data acquisition. Note that this assumption is used only for purposes of data visualization by the CR10 user interface. When a dataset is selected for downloading, only the raw measured data are provided for a selected time interval.

For Liulin data normalization purposes, the linear least-squares fits are normalized to altitude 40 000 ft and 60° north latitude. It enables us to display the Liulin aircraft data together with the counts of the neutron monitor from the Lomnický štít observatory[6] (the data from Lomnický štít are preliminary and checking for the sensitivity coefficient over 35 years of measurement is in progress). The data are displayed in percent scale. For the neutron monitor data, the percentages are normalized to 100% level reached in September 1986 and represented 1 745 200 counts per hour. For the Liulin data, 100% is 1.55 particles per square centimeter per 1 second.

User Interface and Data Provided

In the web-based application, a user can choose a central day of interest and a number of days around this day. The CR10 plots a graph with a preview of Liulin data and neutron monitor data for a selected time interval.

The displayed selection of data can be exported to a comma-separated values (CSV) file. The downloaded data are composed from raw data from Liulin silicon spectrometer, aircraft telemetry data, a dose rate in silicon, D (Si), and an ambient dose equivalent rate, $H^*(10)$, values calculated by our group[3,7] and effective dose rate, E, calculated by CARI-7 program[8] under ICRP-103 recommendation. The meaning of each column in the CSV file is shown in Table 2.

Database/Application Technical Details

The *pandas*[9] data analyses library was used for data processing. The raw data obtained from the Liulin

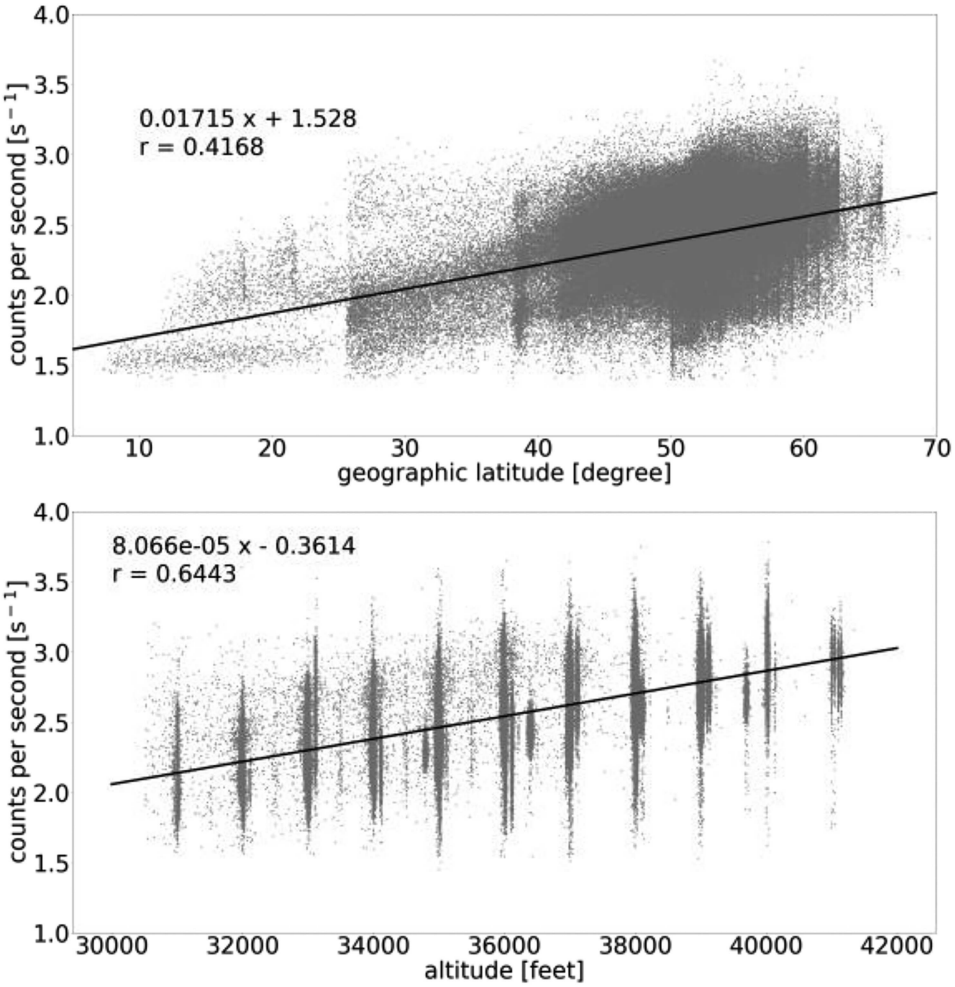

Figure 2. Linear approximations of particle fluxes in dependence on latitude (top) and altitude (bottom). All measurements above altitude 30 500 ft are plotted.

MDUs are stored as one file (AllRunSort.txt) on the server, and those data can be downloaded from the server by CR10 application/database interface.

Separate optimized files with preprocessed data (see section Data Visualization above) can be used for a quick data selection (LSradiation.csv and radiation_avg.csv for Neutron Monitor data and Liulin data, respectively). These files are generated only for internal database/application use, i.e. the user of CR10 does not see these files at http://cr10.odz.ujf.cas.cz.

The provided scripts (written in Python) are used for data selection, visualization and preprocessing (e.g. data filtering and data normalization). After debugging, these scripts were ported using Common Gateway Interface (CGI) technology to a web interface. This approach allows a rapid software development. These scripts/notebooks for the subsequent data processing are available at GitHub[10] and the CR10 database/application source code at GitHub[11], both as an open source.

RESULTS AND DISCUSSION

The CR10 database (http://cr10.odz.ujf.cas.cz) provides long-term dosimetry measurements covering a whole period of the Solar Cycle 24. Figure 3 shows all measurements averaged over quarter of year.

The data followed the same trend except the period around the year 2011. We have no explanation for this discrepancy. Note that these data were obtained with three different dosemeter units (Table 1) which may possess slightly different response functions[3]. Further, the type of aircraft and flight routes were

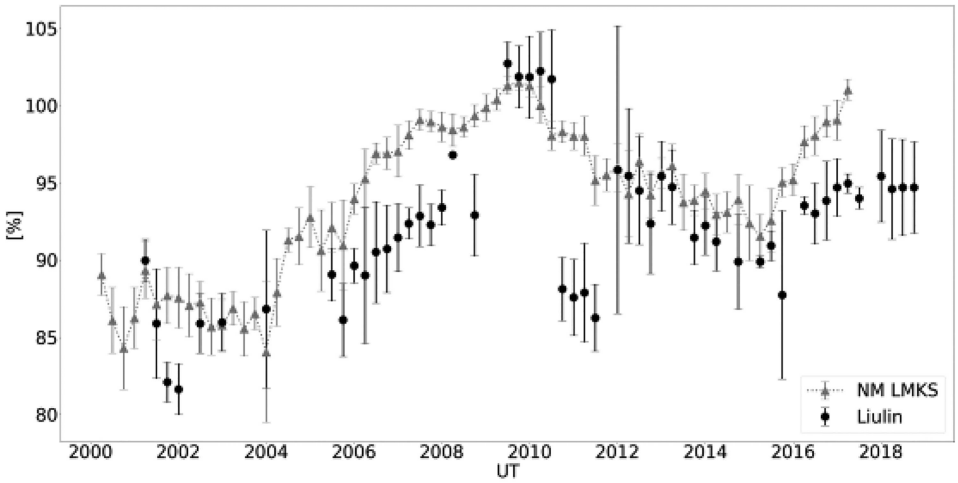

Figure 3. Long-term radiation measurements as an output of CR10 database. Markers show quarterly averaged data with their standard deviations. Circles belong to the Liulin. Triangles show data from the neutron monitor at the Lomnický štít observatory.

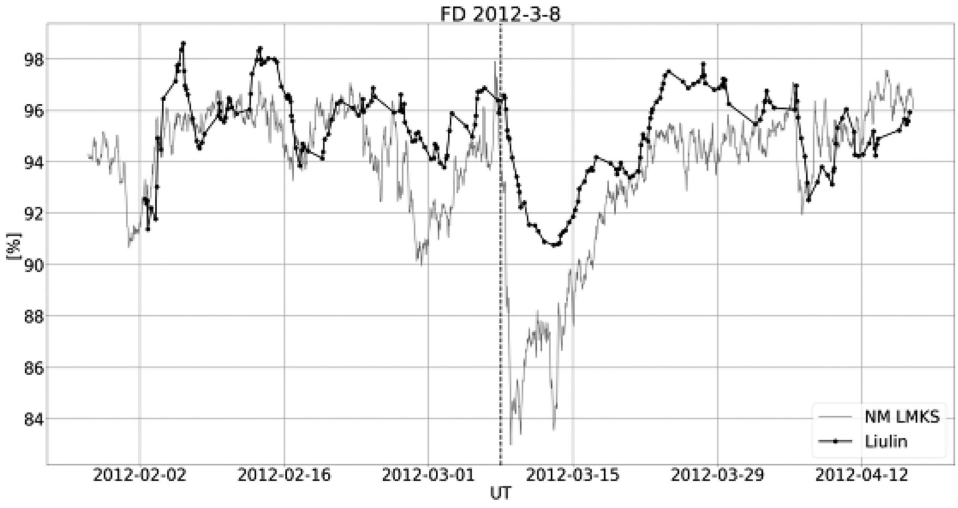

Figure 4. Selected CR10 database output around the Forbush decrease on 8th March 2012.

also changed, and deployment and orientation of the dosemeters on board the aircraft were not always the same during the monitored period. The data evaluation was done based on archival calibration records.

The data in CR10 database were used to discuss a correlation of aircraft measurements with ground-based data[12].

The database enables the user further investigation of disturbances in the cosmic ray flux based on the use of on-board aircraft dosimetry measurements. For this work, there are tools developed by the authors of this article namely the scripts in Python notebooks (display-selection.ipynb)[10]. A second example of data use can be the evaluation of fluctuations in the cosmic ray flux. For example, the mean flux through 10 flights was calculated. Than we looked for a reduction in flux of greater than 5% for more than 12 hours in up to 5 days. With this approach, the FD 2012-03-08 was detected in the CR10 database, as shown in Figure 4. Note that relative units are used for comparison of Liulin and neutron monitor data. Therefore we can compare only the trend but not absolute values.

Table 2. Description of data.

Column name	Example of data	Description
Date	2005-05-08 00:29	Date end time of measured point
Flight	JFKPRG	Code of taking-off and landing airport
lat	43.1	Geodetic latitude in degrees
lon	−72.4	Geodetic longitude in degrees
alt	33019.0	Altitude in feet
D(Si)	1.82	Dose rate absorbed in silicon, $\mathrm{d}D_{\mathrm{Si}}/\mathrm{d}t$, in μGy/h
H	5.98	Ambient dose equivalent rate, $\mathrm{d}H*(10)/\mathrm{d}t$, in μSv/h
E	4.68	Effective dose rate, $\mathrm{d}E/\mathrm{d}t$, according to CARI-7 model in μSv/h
1	0.0	Number of events in the 1-st spectrometer channel per tdelta
2	198.0	Number of events in the 2-nd spectrometer channel per tdelta
3	121.0	Number of events in the 3-rd spectrometer channel per tdelta
...	...	...
256	0.0	Number of events in the 256-th spectrometer channel per tdelta
tdelta	300.0	Integration time (5 min)
Count	761.0	Sum of all events in all channels from the 4-th channel

CONCLUSION

We have developed a new database containing dosimetric measurements aboard aircraft, which allows access for everybody. The database is hosted at http://cr10.odz.ujf.cas.cz. The data from this database are available for detailed analysis of provided particle fluxes in aircraft altitudes, for assessing the radiation exposure of aircraft crew and passengers and for data comparison with other airborne or ground-based cosmic ray radiation measurements. Hopefully, the display of scientific data with graphical interface provided by CR10 database will be used frequently by the scientific community and will encourage future work in this area.

ACKNOWLEDGEMENT

Many thanks to the Czech Airlines company for data acquisition. We cannot forget the pioneering work of Professor František Spurný in the field of dosimetry measurements aboard aircraft. Creation of the CR10 database was funded by European Space Agency through a grant ESA Summer of Code in Space 2015. Maintenance of the CR10 database is supported by OP RDE, MEYS, under the project CRREAT, CZ.02.1.01/0.0/0.0/15_003/0000481.

REFERENCES

1. Dachev, T. P. *et al. Space radiation dosimetry with active detections for the scientific program of the second Bulgarian cosmonaut on board the Mir space station*. Adv. Space Res. **9**, 247–251 (1989).
2. Spurný, F. and Dachev, T. *Long-term monitoring of the onboard aircraft exposure level with a Si-diode based spectrometer*. Adv. Space Res. **32**, 53–58 (2003).
3. Ploc, O., Ambrožová, I., Kubančák, J., Kovář, I. and Dachev, T. P. *Publicly available database of measurements with the silicon spectrometer Liulin onboard aircraft*. Radiat. Meas. **58**, 107–112 (2013).
4. Dachev, T. *et al.* Technical Description of Liulin-4 Type LET Spectrometers (LETS). (Sofia, Bulgaria: Solar–Terrestrial Influences Laboratory, Bulgarian Academy of Science). Available online at http://www.stilrad.stil.bas.bg/publications/Technical%20description%20LETS%20links.pdf (Accessed 20 September 2019)
5. Dachev, T., Dimitrov, P., Tomov, B. and Matviichuk, Y. Technical Description of the Spectrometer-Dosimeter Liulin-6C MDU-6. (Sofia, Bulgaria: Solar–Terrestrial Influences Laboratory, Bulgarian Academy of Science) (2009).
6. Kudela, K. and Langer, R. *Cosmic ray measurements in high Tatra mountains: 1957–2007*. Adv. Space Res. **44**, 1166–1172 (2009).
7. Kyselová, D., Ambrožová, I., Krist, P., Kubančák, J., Uchihori, Y., Kitamura, H. and Ploc, O. *Calibration of modified Liulin detector for cosmic radiation measurements on-board aircraft*. Radiat. Prot. Dosim. **164**, 489–492 (2015).
8. Copeland, K., Friedberg, W., Duke, F., Snyder, L., O'Brien, K., Parker, D., Shea, M. and Smart, D. Computer Program CARI-7. (Oklahoma City, Oklahoma: US Federal Aviation Administration, Civil Aeromedical Institute), Available online at https://www.faa.gov/data_research/research/med_humanfacs/aeromedical/radiobiology/cari7/ (Accessed 1-Oct-2018).
9. The pandas project. Available online at https://pandas.pydata.org (Accessed 20-September-2019).
10. Kákona, M . Scripts for data analysis for Liulin MDU. Available online at https://github.com/ODZ-UJF-AV-CR/liulin (Accessed 1-Dec-2018).
11. Kákona, M . CR10 database. Available online at https://github.com/ODZ-UJF-AV-CR/CR10 (Accessed 1-Dec-2018).
12. Kákona, M., Ploc, O., Kyselová, D., Kubančák, J., Langer, R. and Kudela, K. *Investigation on contribution of neutron monitor data to estimation of aviation doses*. Life Sci. Space Res. **11**, 24–28 (2016).

Attachment B

Life Sciences in Space Research 11 (2016) 24–28

Contents lists available at ScienceDirect

Life Sciences in Space Research

journal homepage: www.elsevier.com/locate/lssr

Investigation on contribution of neutron monitor data to estimation of aviation doses

M. Kákona[a,b], O. Ploc[a], D. Kyselová[a,b], J. Kubančák[a], R. Langer[c], K. Kudela[c,*]

[a] Nuclear Physics Institute of the Czech Academy of Sciences, Department of Radiation Dosimetry, Prague, Czech Republic
[b] Czech Technical University, Faculty of Nuclear Sciences and Physical Engineering, Prague, Czech Republic
[c] Institute of Experimental Physics, Košice, Slovakia

ARTICLE INFO

Article history:
Received 31 August 2016
Revised 7 November 2016
Accepted 8 November 2016

Keywords:
Radiation dose on aircraft
Cosmic rays measured on ground

ABSTRACT

Recently, many efforts have appeared to routinely measure radiation exposure (RE) of aircraft crew due to cosmic rays (CR). On the other hand real-time CR data measured with the ground based neutron monitors (NMs) are collected worldwide and available online. This is an opportunity for comparison of long-term observations of RE at altitudes of about 10 km, where composition and energy spectra of secondary particles differ from those on the ground, with the data from NMs. Our contribution presents examples of such type of comparison.

Analysis of the silicon spectrometer Liulin measurements aboard aircraft is presented over the period May–September 2005 and compared with data from a single NM at middle latitude. While extreme solar driven events observed by NMs have clearly shown an impact on dosimetric characteristics as measured on the airplanes, the transient short time effects in CR of smaller amplitude have been not studied extensively in relation to RE. For the period May–September 2005, when aircraft data become available and several Forbush decreases (FDs) are observed on the ground, a small improvement in the correlation between the dose measured and multiple linear regression fit based on two key parameters (altitude and geomagnetic cut-off rigidity), is obtained, if the CR intensity at a single NM is added into the scheme.

1. Introduction

People on-board aircraft at flight altitudes are exposed to higher doses of radiation than on the ground. The level of cosmic radiation is high enough to gain a need to monitor the effective doses of aircraft crew because they are usually higher than 1 mSv per year (ICRP60). In 1998, it was incorporated in the Czech law that airline companies registered in the Czech Republic are obliged to monitor and store the effective doses of their aircraft crews. The method of routine dosimetry of aircraft crew in the Czech Republic (Malušek et al., 2010) is based on a calculation method using the program CARI-6 (O'Brien et al., 2003). The solar activity is incorporated into the calculation program through the monthly averaged heliocentric potential evaluated from the radiation measurements using neutron monitors. Sudden variations of primary CR flux due to processes in the inner heliosphere as GLE (Ground Level Enhancement) or FD (Forbush decrease) are not taken into account frequently. There is plenty of papers dealing with GLEs and FDs among them several related to radiation dose at airplane altitudes published in recent years (e.g. (Bütikofer and Flückiger, 2011; Mishev et al. 2015)).For a strong GLE or a strong FD the change of the dose on airplanes is reported (e.g. (Spurný and Dachev, 2001; Spurný et al., 2004)). However, the question to what extent the variations of CR on shorter time scales are important for improving the existing models of radiation dose on airplanes, is not extensively studied. Such variations occur due to transitional effects (solar flares, coronal mass ejections (CMEs), particle acceleration at interplanetary plasma discontinuities).

2. Measurements

The database of long-term measurements performed onboard aircraft with the semiconductor spectrometer Liulin (Dachev et al., 2009, 2011) is publically available on internet (CR10 database (Kákona et al., 2016)). Such database includes basic analysis tools for data selection, plotting and downloading and differs from the previously published database (Ploc et al., 2013). The Liulin has been placed in the cabin of Czech Airlines aircraft since March 2001. The database comprises data from several thousand flights and contains more than 190 000 individual records with information on the energy deposition spectra, absorbed dose rates and ambient dose equivalent rates measured with the Liulin together with

* Corresponding author.
E-mail address: kkudela@saske.sk (K. Kudela).

http://dx.doi.org/10.1016/j.lssr.2016.11.001
2214-5524/

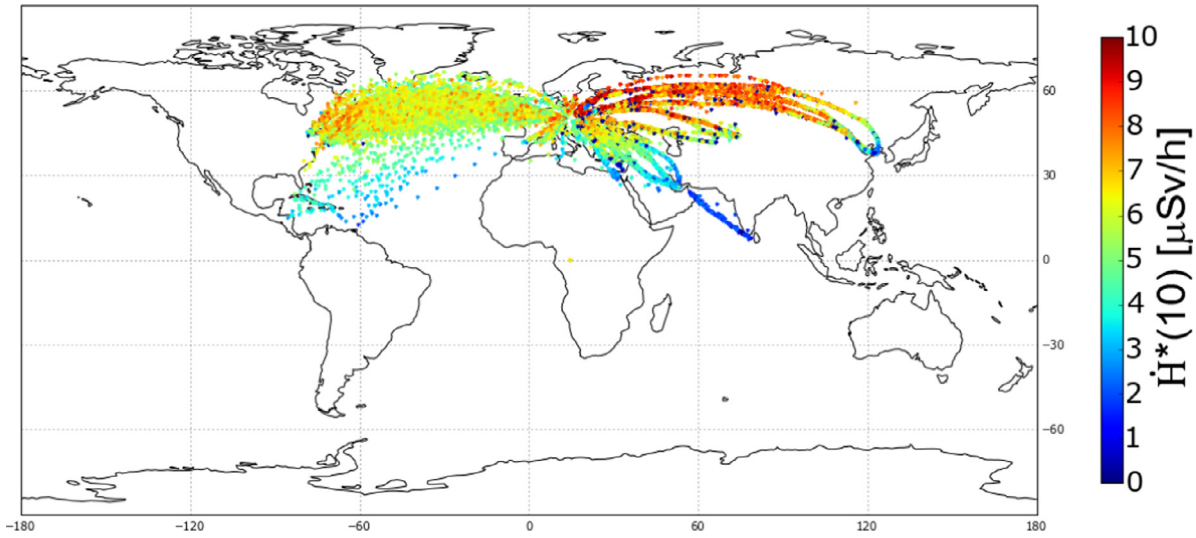

Fig. 1. Scatter plot of dose equivalent rates measured with the Liulin over the map. Figure covers whole period of measurements from 2001 to 2014.

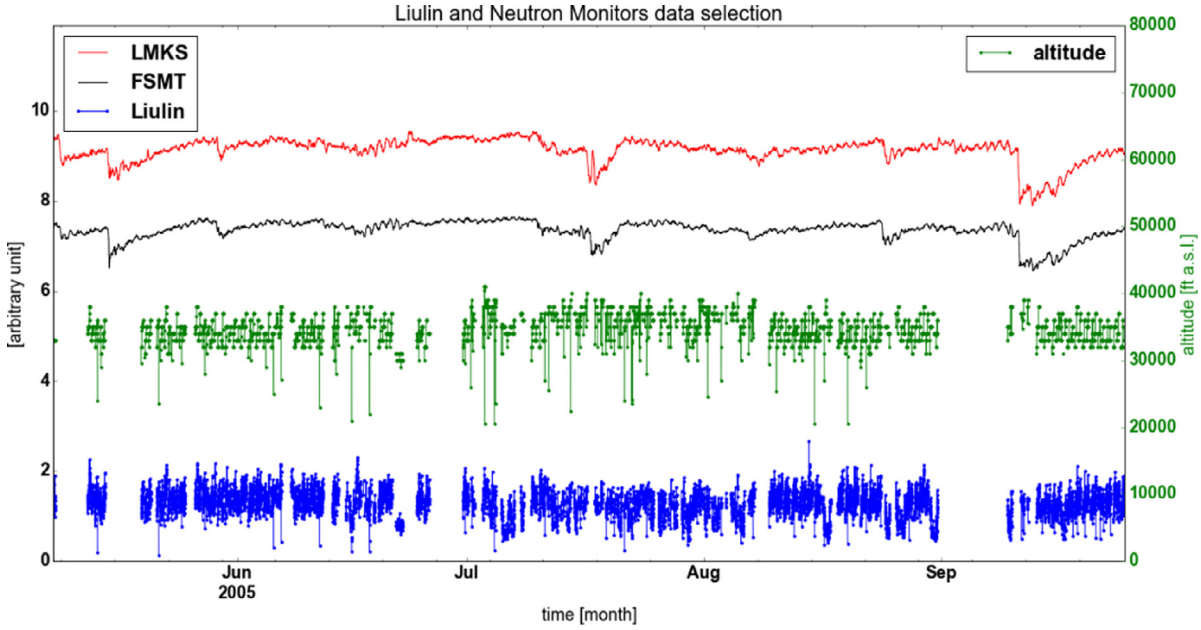

Fig. 2. Sample of data selected for comparison of LIULIN dose rate (blue) observed at various altitudes (green) with the CR recordings at two neutron monitors with different geomagnetic cut-off rigidity Rc, namely Lomnicky stit (LMKS, Rc = 3.8 GV) (Kudela and Langer, 2009) and Fort Smith (FSMT, Rc = 0.3 GV). Data from more NMs can be found at HYPERLINK " http://nmdb.eu. (For interpretation of the references to colour in this figure legend, the reader is referred to the web version of this article.)

the aircraft position data. Ambient dose equivalent rates plotted over the world map are in Fig. 1.

A sample of data was selected from 8th May to 24th September 2005 because the data measured with Liulin were cross-verified by the measurements using passive detectors - thermoluminescent and track-etch detectors (Spurný et al., 2007). The data from the CR10 database and two NMs are plotted in Figs. 2 and 3. The hourly data available from two neutron monitors and 10 min data from Liulin are plotted. Resampling of all data to period 2 h was used with 2 h average for elimination of possible time inaccuracy.

For the analysis a data set comprised of the position and time of dose measurements as well as of normalized values of the count rates at two NMs was constructed. The data set contains the time of the start of measuring interval (T), geographic latitude and longitude (lat, lon), altitude (ALT in ft a.s.l., 1000 m = 3281 ft), the dose rate absorbed in silicon (D_{Si} in μGy/h) calculated by method described in Ploc et al. (2013) and hourly mean of NM count rate at Lomnický štít (LMKS) and at Fort Smith (FSMT) divided by 1000. In addition, the geomagnetic latitude (MAGLAT) has been computed.

3. Results and discussion

As a first step the CARI-6 procedure of calculation was used to obtain estimates (E) of the effective dose rates in the flights. As input for the calculations there are used geographic coordinates, altitude and heliocentric (modulation) potential from the site http://www.faa.gov/data_research/research/med_humanfacs/aeromedical/radiobiology/heliocentric - monthly means. The use of heliocentric potential for aircraft dosimetry is discussed e.g. by O'Brien et al. (2005). The estimate E obtained in such manner has rather high correlation coefficient with the DSi (measured) value. It is illustrated in Fig. 4.

Trying to check usefulness of simplification in estimate of the dose measured by LIULIN during the interval mentioned, we anal-

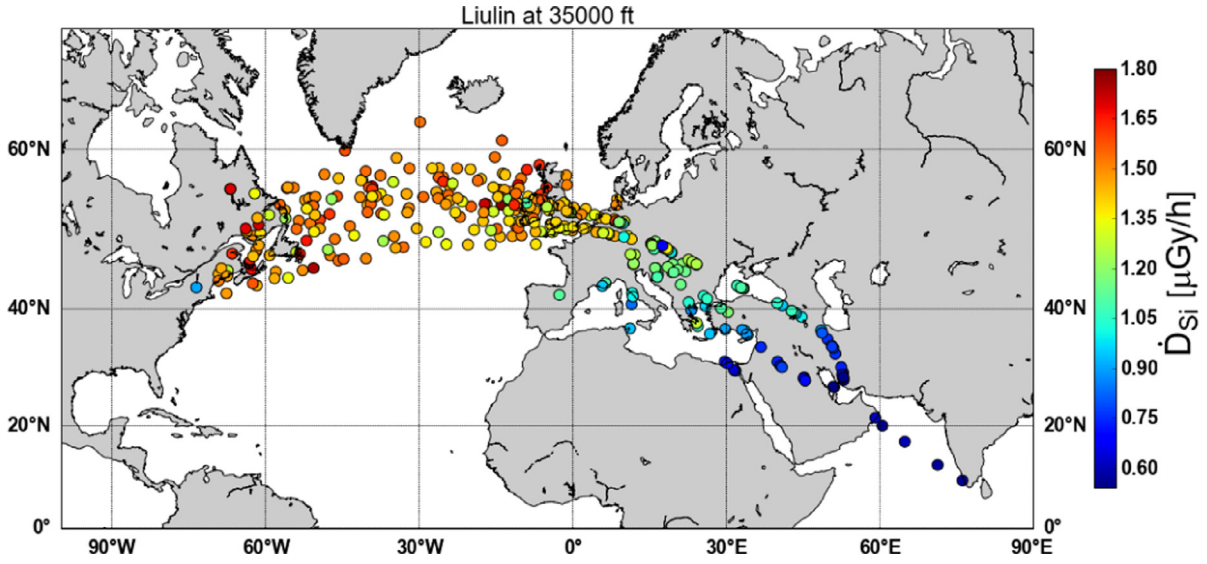

Fig 3. Scatter plot of the measurements selected for this article. Points display dose rate in silicon measured with the Liulin over the map. One point is 1 h average of dose rate. All plotted measurements are taken from flight altitude 35,000 ft (10,668 m).

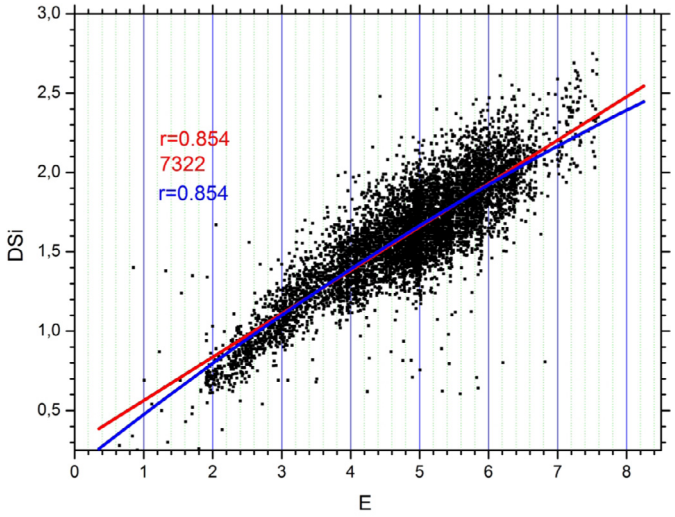

Fig. 4. Measured DSi versus estimated value E for all points in selection of points plotted in Fig. 2. Red and blue are the linear and quadratic approximations. (For interpretation of the references to colour in this figure legend, the reader is referred to the web version of this article.)

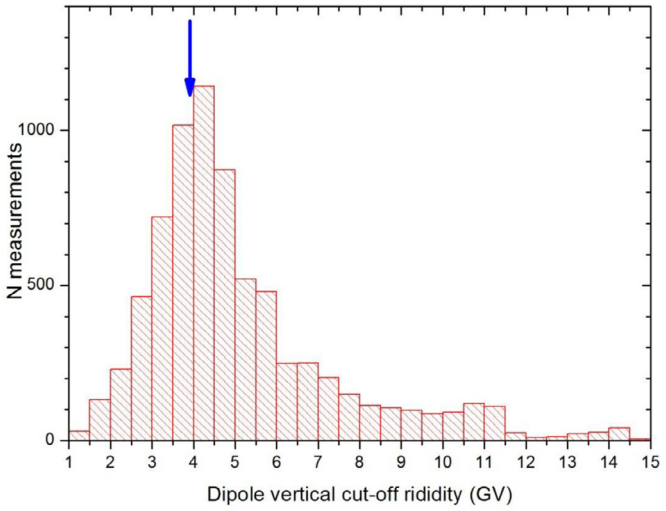

Fig. 5. Histogram of vertical cut-off rigidities corresponding to the sites of measurements of Fig. 2. The arrow indicates nominal cut-off rigidity of Lomnicky stit.

ysed the dependences of DSi on the three key parameters, namely geomagnetic cut-off rigidity, the altitude and variability of the primary CR flux. The cut-off rigidity (vertical, dipolar magnetic field) is proportional to cos4(maglat), where maglat is dipolar magnetic latitude (e.g. formulae 5 in paper by Smart and Shea (2005)). We have computed the geomagnetic dipolar latitude for each position from the geographic coordinates. The geomagnetic latitude was computed using formula (1.17) of the book Ondoh and Marubashi (2001). Latitudinal surveys of CR flux (e.g. recently Gil et al., 2015) in first approach can be taken as a linear function of cut-off rigidity (with the exception of low cut-offs). The altitude dependence of the dose (in the range of covered altitudes) has been taken as a linear one. This approach was accepted after approximation of the scatter plots of the doses measured versus altitude in several functional forms. The logarithmic form (i.e. log(dose) = A + B. altitude) which is closer to the profile plotted e.g. in Fig. 8.2 of the book Davis et al. (2008) did not provide better fit than the linear one. The primary CR approach (in CARI-6 computations taken as monthly means of modulation parameter) was here replaced by the ground based measurement at NM with nominal cut-off rigidity 3.84 GV (Lomnicky stit). Assuming the distribution of cut-off rigidities of the whole set of measurements (Fig. 5) we suppose that hourly values of such measurement are appropriate as a first approximation (linear) of the primary CR and of its variability for the set of measurements.

Using the data set constructed (designated as “DSi measured” in further text), a linear best fit of the dose rate absorbed in silicon measured by Liulin instrument, assuming just multiple linear regression of $\dot{D}$Si dependence on altitude and on Rc in dipolar approximation, has been obtained (designated as “FITDSi” in further text). Fig. 6 indicates it.

There are various models of prediction of radiation exposures (overview e.g. in Bottollier-Depois et al. (2012)) One of the models, namely NAIRAS is using for solar modulation parametrization also data from selected NMs including Lomnicky stit (Mertens et al., 2012). During the period under investigation (~4 months) the modulation potential (Usoskin et al., 2011) is not changing significantly (with the exception of monthly mean of September 2005).

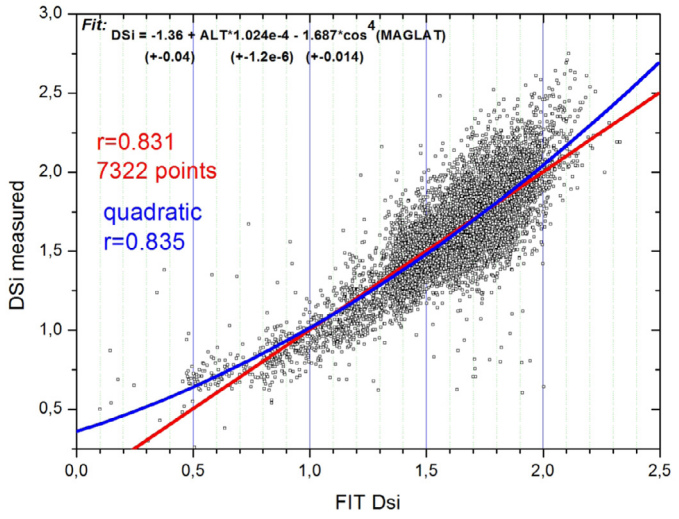

Fig. 6. Scatter plot of DSi measured versus FITDSi (the formulae inside the figure, with the errors of parameters). All points when complete information of the dose and position are used. Linear and quadratic fits of DSi versus FITDSi characterized by Pearson's correlation coefficient is plotted too.

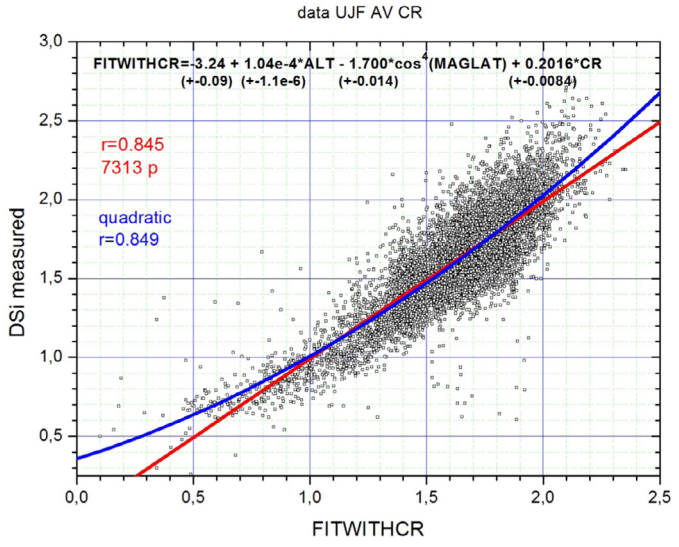

Fig. 7. Scatter plot of the DSi measured versus the fit adding into multiple linear regression (Fig. 6) the NM count rate at Lomnicky stit. FITWITHCR, its optimum form is inside the figure. Linear and quadratic fits of DSi versus FITWITHCR characterized by Pearson's correlation coefficient is plotted too.

The question to what extent the hourly data of pressure corrected count rates by NMs can improve the fit of the dose dependence on altitude and geomagnetic latitude solely, was checked using a single NM data at LMKS. Fig. 7 is indicating such fit.

Checking the quality of the two fits (FITDSi and FITWITHCR) according to correlation coefficients with the measured values of the doses on airplane, the difference is rather a small one ($r = 0.831$ and $r = 0.845$ for the two cases). Number of points is however high (about 7300). Using the approach by Soper (2016) and calculator of statistical difference between two correlations, one obtains $p = 0.0045$. Value $p < 0.05$ indicates that the two correlation coefficients are significantly different from each other. On the other hand one has to be careful about comparisons we are providing here. Fisher test (r-to-z transformation) can be strictly applied only to evaluate significance of the difference between two correlation coefficients, found in two independent samples, which is not the strictly the case here.

4. Summary

The dose rate absorbed in silicon as measured by Liulin on airplanes during interval May–September 2005, characterized by several short time variations of the flux of primary CR due to transient effects of inner heliospheric origin, can be approximated by the multiple linear regression fit with altitude and vertical cut-off rigidity in dipolar field as two independent variables. Addition of one more independent variable (CR flux at a single NM at middle latitudes) affected the fit insignificantly. The simplified linear fit using three key parameters, namely geomagnetic vertical cut-off rigidity, altitude and hourly measurement of a NM representing approximately the variability of primary CR along the measurement paths, provide (for the interval selected) an approach of almost similar quality than that based on CARI-6 calculations using monthly means of modulation potential. Similar type of analyses, if done for various intervals, measurements of dose rate by different type of detectors, and including more ground based CR measurements by NMs at various positions, may be of interest in checking validity of models of radiation doses constructed. For such comparison the collaboration between cosmic ray physicists, experts in experimental dosimetry and designers of the models of radiation within the atmosphere, is important.

Acknowledgement

This work was supported by the Slovak Research and Development Agancy under the contract No. APVV-15-0194. Support by a project of bilateral collaboration between The Czech Academy of Sciences and Slovak Academy of Sciences (SAV-AV ČR 15-19) is acknowledged. Neutron monitors of the Bartol Research Institute (data from Ft. Smith used here) are supported by the National Science Foundation. We are much obliged to the Czech Airlines, namely to Bořek Kolář, Jan Rusek, Ondřej Štursa, Jan Starý and Jan Kment. Thanks to them we could install our cosmic ray detector Liulin on board the aircraft.

References

Bottollier-Depois, J.-F., et al., 2012. Comparison of codes assessing radiation exposure of aircraft crew due to galactic cosmic radiation. Directorate - General for Energy Directorate D — Nuclear Safety & Fuel Cycle Unit D4 — Radiation Protection Dosimetry available at https://ec.europa.eu/energy/sites/ener/files/documents/173.pdf.

Bütikofer, R., Flückiger, E.-O., 2011. Radiation doses along selected flight profiles during two extreme solar cosmic ray events. Astrophys. Space Sci. Trans. 7, 105–109.

Dachev, T., Dimitrov, P., Tomov, B., Matviichuk, Y., 2009. Technical Description of the Spectrometer-Dosimeter Liulin-6C MDU-6. Solar–Terrestrial Influences Laboratory, Bulgarian Academy of Science, Sofia, Bulgaria.

Dachev, T., Spurný, F., Ploc, O., 2011. "Characterization of the radiation environment by Liulin-type spectrometers". Radiat. Prot. Dosim. 144 (1-4), 680–683.

Davis, J.R., Johnson, R.J., Stepanek, I., Fogarty, J.A., 2008. Fundamentals of Aerospace Medicine. Walters Kluwer.

Gil, A., Usoskin, I.G., Kovaltsov, G.A., Mishev, A.L., Corti, C., Bindi, V., Sep. 2015. Can we properly model the neutron monitor count rate? J. Geophys. Res. 120 (9), 7172–7178. doi:10.1002/2015JA021654.

ICRP 60, 1991. Recommendations of the international commission on radiological protection. Ann. ICRP 21 (1-3).

Kákona, M., Kyselová, D., Ambrožová, I., Kubančák, J., Langer, R., Kudela, K., Ploc, O., 2016. CR10 - the public database of cosmic radiation measurements at aviation altitudes of about 10 km. Submited to Radiat. Meas.

Kudela, K., Langer, R., 2009. Cosmic ray measurements in high Tatra mountains: 1957–2007. Adv. Space Res. 44 (10), 1166–1172.

Malušek, A., et al., 2010. Routine individual monitoring of aircraft crew exposure; Czech experience and results 1998–2008. Radiat. Prot. Dosim. ncq337.

Mertens, Ch.J., et al., 2012. Atmospheric ionizing radiation from galactic and solar cosmic rays. Current Topics in Ionizing Radiation Research. INTECH Open Access, Publisher doi:10.5772/32664.

Mishev, A.L., et al., 2015. Computation of dose rate at flight altitudes during ground level enhancements no. 69, 70 and 71. Adv. Space Res. 55 (1), 354–362.

O'Brien, K., et al., 2003. World-wide radiation dosage calculations for air crew members. Adv. Space Res. 31 (4), 835–840.

O'Brien, K., Felsberger, E., Kindl, P., 2005. Application of the heliocentric potential to aircraft dosimetry. Radiat. Prot. Dosim. 116 (1-4 Pt 2), 336–342.
Ondoh, T., Marubashi, K. (Eds.), 2001, Science of Space Environment. Ohmsha Ltd, Japan.
Ploc, O., et al., 2013. Publicly available database of measurements with the silicon spectrometer Liulin onboard aircraft. Radiat. Meas. 58, 107–112.
Smart, D.F., Shea, M.A., 2005. A review of geomagnetic cutoff rigidities for earth-orbiting spacecraft. Adv. Space Res. 36, 2012–2020.
Soper, D.S., 2016. Significance of the difference between two correlations calculator. Software. Available from http://www.danielsoper.com/statcalc.
Spurný, F., Dachev, T., 2001. Measurements in an aircraft during an intense solar flare, ground level event 60, on the 15th of April 2001. Radiat. Prot. Dosim. 97 (3) 297-297.
Spurný, F., Kudela, K., Dachev, T., 2004. Airplane radiation dose decrease during a strong Forbush decrease. Space Weather 2 (5). doi:10.1029/2004SW000074.
Spurný, F., Ploc, O., Jadrníčková, I., Turek, K., Dachev, T., Gelev, M., 2007. Monitoring of onboard aircraft exposure to cosmic radiation: May–December 2005. Adv. Space Res. 40 (11), 1551–1557.
Usoskin, I.G., Bazilevskaya, G.A., Kovaltsov, G.A., 2011. Solar modulation parameter for cosmic rays since 1936 reconstructed from ground-based neutron monitors and ionization chambers. J. Geophys. Res. 116 (A2). doi:10.1029/2010JA016105.

Attachment C

Comparative measurements of mixed radiation fields using liulin and AIRDOS dosimeters

Cite as: AIP Conference Proceedings **2075**, 130003 (2019); https://doi.org/10.1063/1.5091288
Published Online: 26 February 2019

Martin Kákona, Václav Štěpán, Iva Ambrožová, Todor Arsov, Jan Chroust, Jakub Kákona, Ivo Kalapov, Pavel Krist, Martina Lužová, Nina Nikolova, Dagmar Peksová, Ondřej Ploc, Marek Sommer, Jakub Šlegl, and Christo Angelov

Comparative Measurements of Mixed Radiation Fields Using Liulin and AIRDOS Dosimeters

Martin Kákona[1,2,a)], Václav Štěpán[1], Iva Ambrožová[1], Todor Arsov[4], Jan Chroust[5], Jakub Kákona[3], Ivo Kalapov[4], Pavel Krist[1], Martina Lužová[1,2], Nina Nikolova[4], Dagmar Peksová[1,2], Ondřej Ploc[1], Marek Sommer[1,2], Jakub Šlegl[1,2] and Christo Angelov[4]

[1]*Nuclear Physics Institute, Czech Academy of Sciences (NPI CAS), Prague, Czech Republic*
[2]*Faculty of Nuclear Sciences and Technical Engineering, Czech Technical University in Prague, Czech Republic*
[3]*Faculty of Electrical Engineering, Czech Technical University in Prague, Czech Republic*
[4]*Institute for Nuclear Research and Nuclear Energy, Bulgarian Academy of Sciences (INRNE BAS), Sofia, Bulgaria*
[5]*Universal Scientific Technologies (UST), Soběslav, Czech Republic*

[a)]Corresponding author: kakona@ujf.cas.cz

Abstract. Cosmic rays represent not only a significant health risk to the crew of spacecraft and aircraft but also a fundamental phenomenon of basic research on the origin and composition of the universe. High-energy atmospheric physics is a newly opened research domain which focuses on research of terrestrial gamma-ray flashes that can measurably contribute to the aircraft-crew irradiation according to the preliminary computer simulations. High-mountain observatories are suitable places for both the continual monitoring of cosmic radiation and the detection of ionizing radiation generated by lightning. Liulin Mobile Dosimetry Unit (MDU) is a silicon diode based radiation dosimeter developed by the team of Tsvetan Dachev at the Bulgarian Academy of Sciences, initially for the MIR space station. It is widely used as an instrument for radiation monitoring on board aircraft, on high altitude observatories as well as for example for ion fragmentation studies. The AIRDOS dosimeter is an open source device for measurement in low intensity mixed ionising radiation fields. In its aircraft version, it houses silicon PIN diode as a radiation detector, an electronics for conversion of the signal to the pulse-height spectra, Global Positioning System (GPS) module, memory card and batteries for one-month monitoring. The hardware design of AIRDOS is built on the Open Hardware modular platform MLAB, the firmware is written in Open Software platform Processing. Full documentation is freely available. Two AIRDOS devices have been installed at Basic Enviromental Observtory (BEO) Moussala in December 2017, complementing the radiation and environment monitoring instruments already available, including the Liulin MDU. Preliminary results of comparative measurements of radiation environment at BEO Moussala using the AIRDOS units and Liulin MDU will be presented. The results from BEO Moussala will be compared with data acquired on board aircraft.

INTRODUCTION

Cosmic rays represent not only a significant health risk to the crew of spacecraft and aircraft but also a fundamental phenomenon of basic research on the origin and composition of the universe. Near ground and at aviation altitudes, two major component of cosmic rays can contribute to the exposure—galactic cosmic radiation (GCR) and solar energetic particles (SEP). Moreover, also other radiation like terrestrial gamma-ray flashes can measurably contribute to the aircraft-crew irradiation according to computer simulations [1, 2].

Semiconductor detector Liulin has been used at both Nuclear Physics Institute of the Czech Academy of Sciences (NPI CAS) and Bulgarian Academy of Sciences (BAS) for measurements onboard aircraft [3, 4, 5, 6, 7, 8, 9] and at high mountain observatories [10, 11]. A new open source silicon-diode based spectrometer has been developed by NPI in collaboration with the Universal Scientific Technologies (UST) company in order to continue and extend the long-term measurements onboard aircraft, up to now performed by the Liulin devices. Precise calibration and tests of stability of this new device are required.

10th Jubilee International Conference of the Balkan Physical Union
AIP Conf. Proc. 2075, 130003-1–130003-6; https://doi.org/10.1063/1.5091288
Published by AIP Publishing. 978-0-7354-1803-5/$30.00

Several simultaneous measurements with Liulin and AIRDOS devices had been performed in accelerator fields and onboard commercial aircraft. By nature, these experiments are short-term, and the radiation fields have specific properties. Accelerator beams are pulsed, with particles delivered in bunches over time. Long distance aircraft flights provide natural radiation environment, with properties changing in time, depending on the trajectory of the aircraft and space weather. The availability of space and time on such flights is limited.

Basic Environmental Observatory (BEO) Moussala of Institute for Nuclear Research and Nuclear Energy (INRNE) BAS [12] is located at the highest peak of Balkan peninsula, at 2925 m a.s.l. and is host to a number of atmospheric and radiation monitoring devices, including the node of Space Environmental Viewing and Analysis Network (SEVAN) [13] and a Liulin-6MB deposited energy spectrometer. Thanks to the altitude, location and well-described environment it is well suited for long-term comparative measurements needed for verification of the AIRDOS device.

DEVICES AND METHODS

Liulin

Liulin is a silicon diode based 256–channel deposited energy spectrometer developed by the team of Tsvetan Dachev at the Bulgarian Academy of Sciences, initially for the deployment at the MIR space station during the 1988 flight of second Bulgarian cosmonaut Aleksandr Panayotov Aleksandrov [14]. The device has since been used for radiation monitoring onboard aircraft, at high altitude observatories [15, 11] as well as for ion fragmentation studies [16]. While the added sensors and connection options were adapted for the targeted use cases, the core sensor and detector electronics remained compatible [17].

In September 2006 the Liulin 6MB has been deployed on BEO Moussala. The 6MB variant is an externally powered compact device with Ethernet port enabling File Transfere Protocol (FTP) and Hypertext Transfer Protocol (HTTP) services for data access (see Figure 1). Data acquired during 2006 were thoroughly compared with other on-site devices [10].

AIRDOS

The long-term measurements onboard commercial aircraft were routinely performed using a single Liulin device at a time. To observe the radiation environment at commercial aircraft flight levels in parallel at multiple locations, a number of detectors is needed. Together with the need for customised and fully documented hardware, this prompted the development of AIRDOS, an open source silicon-diode based spectrometer, generally targeted for use in low intensity mixed radiation fields.

The initial "A" version of AIRDOS developed in collaboration with the Universal Scientific Technologies (`http://ust.cz`) is built on the open hardware modular platform MLAB (`http://mlab.cz`) and programmed using the open software Processing (`https://processing.org`) software platform. Modular hardware design enables easy modifications and rapid development.

In its aircraft version, the AIRDOS A houses Hamamatsu S2744-09 silicon PIN diode as the radiation detector, electronics for conversion of the signal to the pulse-height spectra, Global Positioning System (GPS) module, Secure Digital memory card (SD Card) and batteries for one-month monitoring. Full documentation is freely available at `https://github.com/ODZ-UJF-AV-CR/AIRDOS`.

Two AIRDOS devices have been installed at BEO Moussala in December 2017. The mountain observatory variant "M" includes ARM-based GNU/Linux computer for data processing and upload, and an external power source instead of lithium batteries. Furthermore, the energy range of this variant is reduced in order to provide more information on the lower part of the energy spectrum.

Energy calibration

AIRDOS

Energetic calibration of the AIRDOS A variant was done at the NPI CAS U-120 M cyclotron in Řež, Czech Republic, using 35 MeV protons attenuated by aluminium degraders, and using alpha particles emitted by ^{239}Pu, ^{241}Am and ^{252}Cf sources. Resulting spectrograms are shown in Figure 2. Graph legend lists the energies of protons and alpha particles just before they enter the sensor window. The energy range of AIRDOS A devices is approximately from 200 keV to 12.4 MeV, the channel width is 49.4 keV.

FIGURE 1. Liulin 6MB (left) and two AIRDOS units (right) installed at BEO Moussala

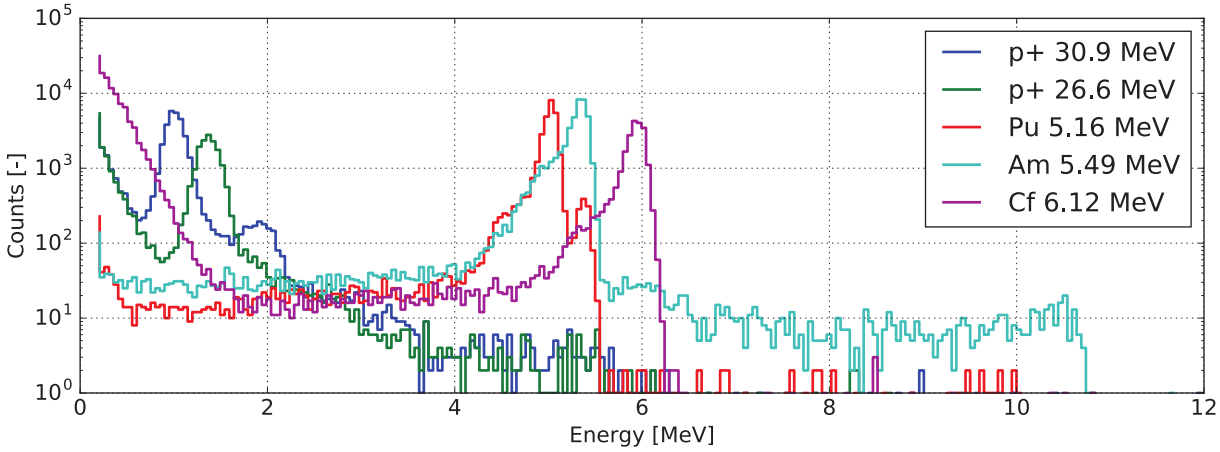

FIGURE 2. Energy response of the AIRDOS dosimeter after calibration.

AIRDOS M devices deployed at the BEO Moussala have been calibrated using alpha particles from ^{241}Am radionuclide source. The channel width has been estimated to 16.9 keV, resulting in energy range of 4.5 MeV.

Liulin

Energetic calibration and energy range for the Liulin-4 device were studied by Dachev *et al.* [18, 19]. Energetic range is from 40 keV to 21 MeV; the proposed calibration equation for energy in channel is E_i[keV] = 81.4 · C − 40.7. For MDU1 and MDU2 Liulin units, the calibration was also performed at National Institute of Radiological Sciences Heavy Ion Medical Accelerator in Chiba (NIRS HIMAC) by Kyselová *et al.* [9] and using alpha particles from radionuclide emitters. The resulting channel width was lower, with 74.2 ± 0.7 and 78.6 ± 0.5 keV for the two units. For alpha calibration, the diode has been replaced by a variant without the resin cover, S2744-09.

Liulin-4 type MDU14 has been used in the measurements onboard aircraft presented below. For this unit, the calibration has been performed at the NIRS HIMAC accelerator in January 2018 using the He 150 MeV beam. The channel width is 69.2 keV. Since the response in the first two channels is close to zero, we only consider energies above 250 keV for Liulin — the same as the noise threshold for the AIRDOS device.

Both devices employ the same sensor, therefore as the first step, the energy spectra and total deposited energy can be computed and compared. As discussed in [8], the total deposited energy can be computed using Equation 1, where ε_i is mean energy of the channel i and N_i is the number of events registered in channel i.

$$\varepsilon = \sum_{i=1}^{256} \varepsilon_i N_i \,. \tag{1}$$

RESULTS

Onboard aircraft

Simultaneous measurements with Liulin and AIRDOS devices have been performed during a number of commercial flights. Presented data were recorded using AIRDOS A (T4) and Liulin-4J (MDU14) dosimeters onboard Airbus 350-900, Jan. 21 2018 during the AY74 flight from Tokyo to Helsinki (NRT–HEL). Figure 3 shows the altitude recorded by GPS, total number of counts registered and the number of counts for $\varepsilon \in \langle 0.25, 12.7 \rangle$ MeV. The 250 keV were chosen as the noise threshold.

Data from 5:00 to 12:00 h have been used to compare the energy spectra, see Figure 4. During this time the aircraft was flying at above 10000 m, at semi-constant latitude over Russia. Counts per channel were scaled by channel widths of the respective detectors to reflect their different energy range. To show the influence of channel width on the energy spectra, results for two calibration options are shown—for the datasheet 81.4 keV channel width and for the 69.2 keV derived from measurements at HIMAC.

Deposited energy ε has been calculated using Equation 1, for $\varepsilon_i \in \langle 0.25, 12.7 \rangle$ MeV and 69.2 keV channel width. Value recorded by Liulin is 11336.9 MeV (in 17382 events), 9.4% higher than the 10360.6 MeV (in 20523 events) recorded by AIRDOS.

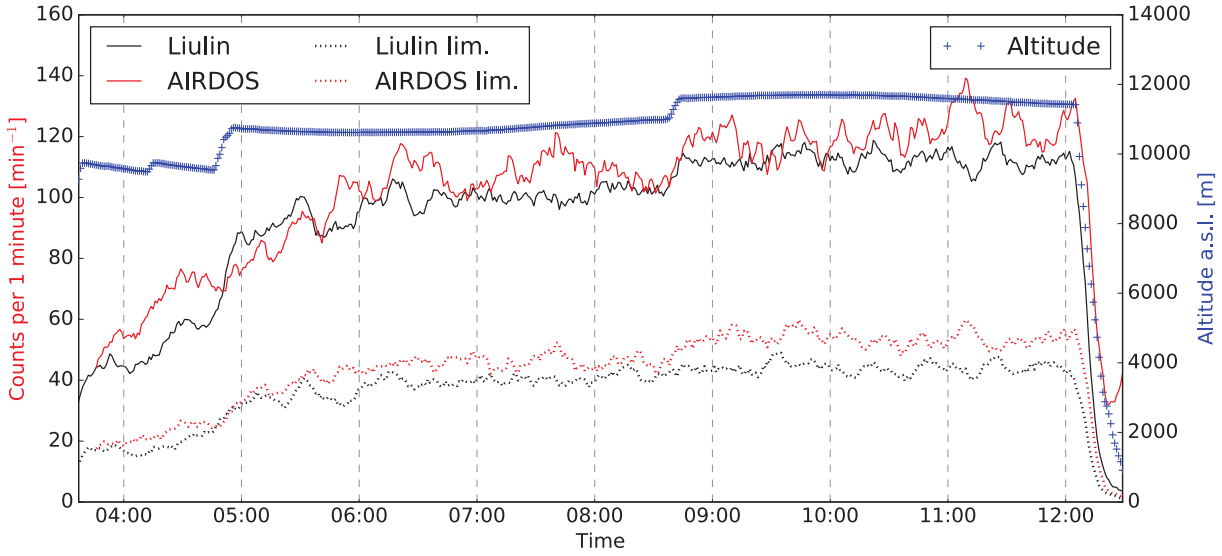

FIGURE 3. Altitude and number of ionising particles registered by AIRDOS and Liulin devices onboard aircraft. Total and limited ($\varepsilon \in \langle 0.25, 12.7 \rangle$ MeV) counts are shown.

BEO Moussala

Liulin-6MB and two AIRDOS M units were operating at the BEO Moussala from December 2017 to August 2018. Energy spectra from data captured for first four months of 2018 were analyzed in the same way as the onboard aircraft measurements and are presented in Figure 4.

Deposited energy ε has been calculated for $\varepsilon_i \in \langle 0.3, 4.5 \rangle$ MeV. Value recorded by Liulin is 215987.2 MeV (in 478068 events), 14.2% higher than the 189164.7 MeV (in 408882 events) recorded by AIRDOS.

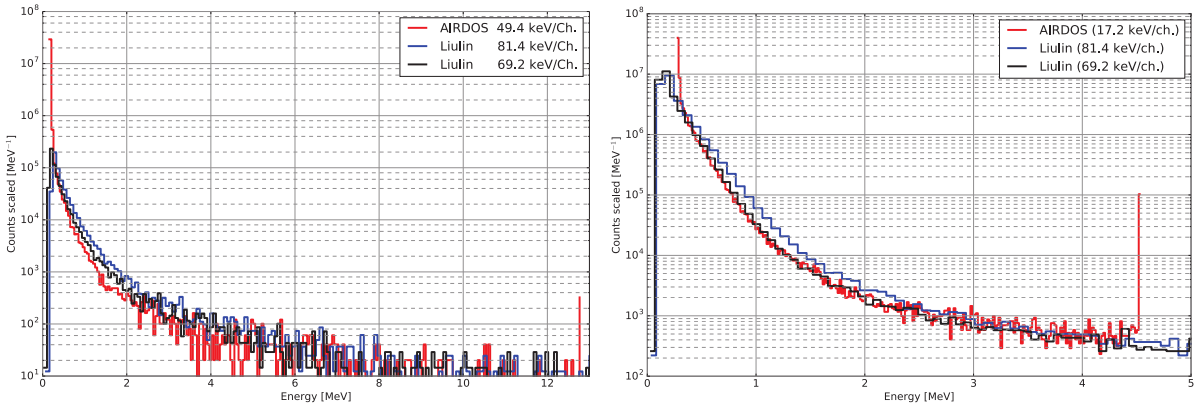

FIGURE 4. Left: Deposited energy spectra measured by Liulin-4 and AIRDOS A during 7 h flight. **Right:** Deposited energy spectra measured by Liulin-6MB and AIRDOS M deployed at the BEO Moussala. In both subfigures, the counts are scaled by channel widths of the respective detectors. Displayed energy range is restricted to AIRDOS detector range.

DISCUSSION

Key factors influencing the presented results are the precision of the energy calibration, choice of noise threshold, dead time of the devices and to a limited extent also the impact of channel width, due to the log-log nature of the recorded spectra.

Significant part of the total deposited energy comes from low energy events. In case of the measurements onboard aircraft, events in first three considered channels for AIRDOS ($233.3 \leq \varepsilon \leq 381.7$ keV) contributed 34.4% of the deposited energy. As noted by Dachev *et al.* [18], moving the spectrum one channel left or right can result in a ±40% difference in dose. This highlights the need for precise assessment both of the channel width and the mean energy of the first channel. Methods should be sought for improvement of the calibration namely in the low energy region.

Two methods were used for calibration of the dosimeters. Calibration using protons and alpha particles relies on knowledge of the thickness of the depleted region of the Si diode. Calibration using ^{241}Am is influenced by thickness of its entrance window. Since AIRDOS currently uses 3 V bias voltage for the sensor diode, both values should be verified.

AIRDOS devices use single controller design in order to minimize energy consumption and design complexity. Dead time is introduced by waiting to SD Card and communication with the GPS module. Correction should be introduced for this factor.

Inherently, a further error is introduced due to different channel widths used by Liulin and AIRDOS and the log-log nature of the energy spectra. Energy spectra from Figure 4 has been used to estimate this error. The data for $\varepsilon \in \langle 0.25, 3 \rangle$ MeV were transformed and fitted as $\log_{10}(N_i/w) = \log_{10}(a + bi)$, where w is the assumed channel width in MeV, resulting in $N_i/w = 2443 \cdot \exp(-2.89i)$ for AIRDOS data. Should the channel width of the AIRDOS be that of Liulin, the expected deposited energy ε would be higher by 4.75 %.

CONCLUSIONS

Presented results confirm suitability of radiation environment at high altitude mountain observatories for long-term comparative measurements using devices intended for low-flux mixed radiation fields, namely such as that on board commercial aircraft.

The experiments provided guidance for further development and improvements both of the calibration and data processing methodology.

Agreement between data recorded by Liulin and AIRDOS devices both in-flight and during long-term measurement at the BEO Moussala is reasonable, given the constraints discussed above.

ACKNOWLEDGEMENTS

We would like to express our thanks to Satoshi Kodaira and the QST/NIRS for all the help at HIMAC. This work was done in frame of the Joint research project "Dosimetry of radiation events in the atmosphere" between Czech Academy of Sciences and the Bulgarian Academy od Sciences and supported by the European Regional Development Fund—Project CRREAT (CZ.02.1.01/0.0/0.0/15_003/0000481), the MEYS project No. LM2015056, the ACTRIS-2 IA in H2020 (2015–2019) and the grant of the National Science Fund of Republic of Bulgaria under project No. DN 04/1, 13.12.2016: "Study of the combined effect of the natural radioactivity background, the UV radiation, the climate changes and the cosmic rays on model groups of plant and animal organisms in mountain ecosystems" (2017–2019).

REFERENCES

[1] J. R. Dwyer, D. M. Smith, M. A. Uman, Z. Saleh, B. Grefenstette, B. Hazelton, and H. K. Rassoul, Journal of Geophysical Research **115**, p. D09206 (2010).
[2] A. Drozdov and A. Grigoriev, Journal of Physics: Conference Series **409**, p. 012246 (2013).
[3] F. Spurný and T. Dachev, Radiation protection dosimetry **100**, 525–528 (2002).
[4] O. Ploc and F. Spurný, Nuclear Instruments and Methods in Physics Research Section A: Accelerators, Spectrometers, Detectors and Associated Equipment **580**, 671–674 (2007), doi:10.1016/j.nima.2007.05.107.
[5] F. Spurny and T. P. Dachev, Acta Geophysica **57**, 125–140 (2009).
[6] A. Malusek, O. Ploc, I. Kovar, K. Brabcova, and F. Spurny, Radiation Protection Dosimetry **144**, 684–687 (2011).
[7] O. Ploc, K. Pachnerova Brabcova, F. Spurny, A. Malusek, and T. Dachev, Radiation Protection Dosimetry **144**, 611–614 (2011).
[8] O. Ploc, I. Ambrozova, J. Kubancak, I. Kovar, and T. P. Dachev, Radiation Measurements **58**, 107–112 (2013).
[9] D. Kyselová, I. Ambrožová, P. Krist, J. Kubančák, Y. Uchihori, H. Kitamura, and O. Ploc, Radiation protection dosimetry **164**, 489–492 (2015).
[10] A. Mishev and E. Hristova, Journal of Environmental Radioactivity **113**, 77–82 (2012).
[11] J. Kubančák, I. Ambrožová, R. Bütikofer, K. Kudela, R. Langer, M. Davídková, O. Ploc, and A. Malušek, Journal of Instrumentation **9**, P07018–P07018 (2014).
[12] C. Angelov, I. Angelov, A. Antonov, *et al.*, "BEO Moussala – a site for integrated environmental studies – first results." in *In: Proc. of Global Change, Environment, Sustainable Development of the Society and High Mountain Observatories Network Conference 21–25 March 2007 Gyulechitsa Bulgaria* (2007), pp. 9–23.
[13] D. Roša, C. Angelov, K. Arakelyan, T. Arsov, K. Avakyan, A. Chilingarian, S. Chilingaryan, A. Hovhannissyan, T. Hovhannisyan, G. Hovsepyan, *et al.*, Central European Astrophysical Bulletin **34**, 115–122 (2010).
[14] T. Dachev, Y. Matviichuk, J. Semkova, R. Koleva, B. Boichev, P. Baynov, N. Kanchev, P. Lakov, Y. Ivanov, P. Tomo, V. Petrov, V. Redko, V. Kojarinov, and R. Tykva, Advances in Space Research **9**, 247–251 (1989).
[15] T. Dachev, Advances in Space Research **44**, 1441–1449 (2009).
[16] O. Ploc, T. Dachev, Y. Uchihori, H. Kitamura, and L. Sihver, "Fragmentation from heavy ion beams in HIMAC BIO room calculated with PHITS and measured with Liulin," in *Aerospace Conference, 2017 IEEE* (IEEE, 2017), pp. 1–10.
[17] T. Dachev, P. Dimitrov, B. Tomov, Y. Matviichuk, F. Spurny, O. Ploc, K. Brabcova, and I. Jadrnickova, Radiation Protection Dosimetry **144**, 675–679 (2011).
[18] T. Dachev, B. Tomov, Y. Matviichuk, P. Dimitrov, J. Lemaire, G. Gregoire, M. Cyamukungu, H. Schmitz, K. Fujitaka, Y. Uchihori, H. Kitamura, G. Reitz, R. Beaujean, V. Petrov, V. Shurshakov, V. Benghin, and F. Spurny, Advances in Space Research **30**, 917–925 (2002).
[19] T. Dachev, P. Dimitrov, B. Tomov, and Y. Matviichuk, "Technical description of Liulin-4 type let spectrometers (LETS)," .

Attachment D

AIRDOS data format

This description of data format is for format version G2.

Example of output:

```
$AIRDOS,G2,d2d1e0d,1290c00806a20090f457a000a00000f0
$CANDY,499,5743,99,18149,3270,17,6,6,3,0,1,0,0,1,0,2,0,0,0,0,0,0,0,0,0,0,0,0,
0,0,0,0,0,0,0,0,0,0,0,0,0,0,0,0,0,0,0,1,0,0,0,0,0,0,0,0,0,0,0,0,0,0,0,0,0,0,0
,0,0,0,0,0,0,0,0,0,0,0,0,0,0,0,0,0,0,0,0,0,0,0,0,0,0,0,0,0,0,0,0,0,0,0,0,0,0,
0,0,0,0,0,0,0,0,0,0,0,0,0,0,0,0,0,0,0,0,0,0,0,0,0,0,0,0,0,0,0,0,0,0,0,0,0,0,0
,0,0,0,0,0,0,0,0,0,0,0,0,0,0,0,0,0,0,0,0,0,0,0,0,0,0,0,0,0,0,0,0,0,0,0,0,0,0,
0,0,0,0,0,0,0,0,0,0,0,0,0,0,0,0,0,0,0,0,0,0,0,0,0,0,0,0,0,0,0,0,0,0,0,0,0,0,0
,0,0,0,0,0,0,0,0,0,0,0,0,0,0,0,0,0,0,0,0,0,0,0,0,0,0,0,0,0,0,0,0,0,24445,20,2
55
$GPVTG,18.58,T,,M,485.858,N,899.809,K,A*0C
$GPGGA,153859.00,5721.19196,N,01655.45164,E,1,05,3.68,11520.5,M,30.0,M,,*54
$GPGSA,A,3,23,09,19,17,01,,,,,,,,4.57,3.68,2.71*0A
$GPGSV,2,1,08,01,19,161,16,06,,,41,09,32,224,42,14,08,054,19*47
$GPGSV,2,2,08,17,23,251,41,19,29,267,43,23,67,198,34,31,28,049,23*71
$GPGLL,5721.19196,N,01655.45164,E,153859.00,A,A*68
$GPRMC,153900.00,A,5721.31916,N,01655.52972,E,486.373,18.62,010919,,,A*51
$GPVTG,18.62,T,,M,486.373,N,900.763,K,A*06
$GPGGA,153900.00,5721.31916,N,01655.52972,E,1,05,3.68,11523.3,M,30.0,M,,*5F
$GPGSA,A,3,23,09,19,17,01,,,,,,,,4.57,3.68,2.71*0A
$TIME,5759
```

$AIRDOS - power-on initial message

```
$AIRDOS,<data format version>,<git hash>,<s.n.>
```

There is a message with initial protocol information.

Value	Length	Type	Note
$AIRDOS	7 B	Char	Header

data format version	1 - 10 B	Char	Version of data format
git hash	4 B	Hex	Git hash tag of source file
s.n.	16 B	Hex	Serial number of this specific piece of hardware

$CANDY - dosimeter data

```
$CANDY, <measurement No.> , <uptime>, <1-st ch.>, <2-nd ch.>, <3-rd ch.>,...,
<filter suppressions>, <flux>, <position of the 1-st channel>
```

There is a message with measured data.

Value	Range	type	Note
$CANDY	6 B	Char	Header
measurement No.	0..65535	Dec	Sequential number
uptime	0..4294967295	Dec	Time in seconds from power-on
1-st ch.	0..65535	Dec	Number of events in 1-st ch.
2-nd ch.	0..65535	Dec	Number of events in 2-nd ch.
...	...		
256-th ch.	0..65535	Dec	Number of events in 256-th ch.
filter suppressions	0..65535	Dec	Number of ussage of digital filter for double peak suppression

flux	0..65535	Dec	Flux calculated for channels above noise
position of the 1-st channel	0..511	Dec	Offset of ADC

$GPRMC, $GPGGA, $GPVTG,... - NMEA messages

Please see NMEA documentation.

$TIME - time from power-on

`$TIME,<seconds>`

There is a message with run time in seconds for purpose of time synchronisation with real time obtained from NMEA messages.

Value	Length	Type	Note
$TIME	5 B	Char	Header
seconds	0..4294967295	Dec	time in seconds from power-on

Attachment E

```
#define DEBUG // Please comment it if you are not debugging
String githash = "d2d1e0d";
String FWversion = "G3";

/*
  AIRDOS02A (RTC, GPS)

3 month endurance with LS 33600 = 7.6 mA
ISP
---
PD0     RX
PD1     TX
RESET#  through 50M capacitor to RST#
SDcard
------
DAT3   SS   4 B4
CMD    MOSI 5 B5
DAT0   MISO 6 B6
CLK    SCK  7 B7
ANALOG
------
+      A0  PA0
-      A1  PA1
RESET  0   PB0
LED
---
LED_red  23  PC7         // LED for Dasa
                     Mighty 1284p
                      +---\/---+
            (D 0) PB0 1|        |40 PA0 (AI 0 / D24)
            (D 1) PB1 2|        |39 PA1 (AI 1 / D25)
       INT2 (D 2) PB2 3|        |38 PA2 (AI 2 / D26)
        PWM (D 3) PB3 4|        |37 PA3 (AI 3 / D27)
     PWM/SS (D 4) PB4 5|        |36 PA4 (AI 4 / D28)
       MOSI (D 5) PB5 6|        |35 PA5 (AI 5 / D29)
  PWM/MISO (D 6) PB6 7|        |34 PA6 (AI 6 / D30)
   PWM/SCK (D 7) PB7 8|        |33 PA7 (AI 7 / D31)
                  RST 9|        |32 AREF
                  VCC 10|        |31 GND
                  GND 11|        |30 AVCC
                XTAL2 12|        |29 PC7 (D 23)
                XTAL1 13|        |28 PC6 (D 22)
       RX0 (D 8) PD0 14|        |27 PC5 (D 21) TDI
       TX0 (D 9) PD1 15|        |26 PC4 (D 20) TDO
RX1/INT0 (D 10) PD2 16|        |25 PC3 (D 19) TMS
TX1/INT1 (D 11) PD3 17|        |24 PC2 (D 18) TCK
     PWM (D 12) PD4 18|        |23 PC1 (D 17) SDA
     PWM (D 13) PD5 19|        |22 PC0 (D 16) SCL
     PWM (D 14) PD6 20|        |21 PD7 (D 15) PWM
                      +--------+
*/

/*
// Compiled with: Arduino 1.8.9
// MightyCore 2.0.2 https://mcudude.github.io/MightyCore/package_MCUdude_MightyCore_index.json
Fix old bug in Mighty SD library
~/.arduino15/packages/MightyCore/hardware/avr/2.0.2/libraries/SD/src/SD.cpp:
boolean SDClass::begin(uint32_t clock, uint8_t csPin) {
  if(root.isOpen()) root.close();
*/

#include <SD.h>             // Revised version from MightyCore
#include "wiring_private.h"
#include <Wire.h>
#include "src/RTCx/RTCx.h"  // Modified version icluded
```

```
66
67  #define LED_red   23   // PC7
68  #define RESET     0    // PB0
69  #define GPSpower  26   // PA2
70  #define SDpower1  1    // PB1
71  #define SDpower2  2    // PB2
72  #define SDpower3  3    // PB3
73  #define SS        4    // PB4
74  #define MOSI      5    // PB5
75  #define MISO      6    // PB6
76  #define SCK       7    // PB7
77  #define INT       20   // PC4
78
79  #define CHANNELS 512   // number of channels in buffer for histogram,
    including negative numbers
80  #define GPSerror 70000 // number of cycles for waitig for GPS in case of GPS
    error
81  #define GPSdelay 5    // number of measurements between obtaining GPS position
82  #define GPSthreshold 3*GPSdelay  // ionising radiation flux threshold for
    obtaining GPS position
83
84  uint16_t count = 0;
85  uint32_t serialhash = 0;
86  uint16_t offset, base_offset;
87  uint8_t lo, hi;
88  uint16_t u_sensor, maximum;
89  struct RTCx::tm tm;
90
91  // Read Analog Differential without gain (read datashet of ATMega1280 and
    ATMega2560 for refference)
92  // Use analogReadDiff(NUM)
93  //   NUM  | POS PIN            | NEG PIN           |   GAIN
94  //  0 | A0      | A1      | 1x
95  //  1 | A1      | A1      | 1x
96  //  2 | A2      | A1      | 1x
97  //  3 | A3      | A1      | 1x
98  //  4 | A4      | A1      | 1x
99  //  5 | A5      | A1      | 1x
100 //  6 | A6      | A1      | 1x
101 //  7 | A7      | A1      | 1x
102 //  8 | A8      | A9      | 1x
103 //  9 | A9      | A9      | 1x
104 //  10  | A10     | A9      | 1x
105 //  11  | A11     | A9      | 1x
106 //  12  | A12     | A9      | 1x
107 //  13  | A13     | A9      | 1x
108 //  14  | A14     | A9      | 1x
109 //  15  | A15     | A9      | 1x
110 #define PIN 0
111 uint8_t analog_reference = INTERNAL2V56; // DEFAULT, INTERNAL, INTERNAL1V1,
    INTERNAL2V56, or EXTERNAL
112
113 void setup()
114 {
115
116   // Open serial communications
117   Serial.begin(9600);
118   Serial1.begin(9600);
119
120   Serial.println("#Cvak...");
121
122   ADMUX = (analog_reference << 6) | ((PIN | 0x10) & 0x1F);
123
124   ADCSRB = 0;               // Switching ADC to Free Running mode
125   sbi(ADCSRA, ADATE);       // ADC autotrigger enable (mandatory for free
    running mode)
```

```
126     sbi(ADCSRA, ADSC);        // ADC start the first conversions
127     sbi(ADCSRA, 2);           // 0x100 = clock divided by 16, 62.5 kHz, 208 us
      for 13 cycles of one AD conversion, 24 us fo 1.5 cycle for sample-hold
128     cbi(ADCSRA, 1);
129     cbi(ADCSRA, 0);
130
131     pinMode(RESET, OUTPUT);   // reset for peak detetor
132
133     //pinMode(SDpower1, OUTPUT);  // SDcard interface
134     //pinMode(SDpower2, OUTPUT);
135     //pinMode(SDpower3, OUTPUT);
136     //pinMode(SS, OUTPUT);
137     //pinMode(MOSI, INPUT);
138     //pinMode(MISO, INPUT);
139     //pinMode(SCK, OUTPUT);
140
141     DDRB = 0b10011110;
142     PORTB = 0b00000000;  // SDcard Power OFF
143
144     DDRA = 0b11111100;
145     PORTA = 0b00000000;  // SDcard Power OFF
146     DDRC = 0b11101100;
147     PORTC = 0b00000000;  // SDcard Power OFF
148     DDRD = 0b11111100;
149     PORTD = 0b00000000;  // SDcard Power OFF
150
151     pinMode(LED_red, OUTPUT);
152     digitalWrite(LED_red, LOW);
153     digitalWrite(RESET, LOW);
154
155     //!!! Wire.setClock(100000);
156
157     for(int i=0; i<5; i++)
158     {
159       delay(50);
160       digitalWrite(LED_red, HIGH);  // Blink for Dasa
161       delay(50);
162       digitalWrite(LED_red, LOW);
163     }
164
165     Serial.println("#Hmmm...");
166
167     // make a string for device identification output
168     String dataString = "$AIRDOS," + FWversion + "," + githash + ","; // FW
      version and Git hash
169
170     Wire.beginTransmission(0x58);                    // request SN from EEPROM
171     Wire.write((int)0x08); // MSB
172     Wire.write((int)0x00); // LSB
173     Wire.endTransmission();
174     Wire.requestFrom((uint8_t)0x58, (uint8_t)16);
175     for (int8_t reg=0; reg<16; reg++)
176     {
177       uint8_t serialbyte = Wire.read(); // receive a byte
178       if (serialbyte<0x10) dataString += "0";
179       dataString += String(serialbyte,HEX);
180       serialhash += serialbyte;
181     }
182
183     {
184       DDRB = 0b10111110;
185       PORTB = 0b00001111;  // SDcard Power ON
186
187       // make sure that the default chip select pin is set to output
188       // see if the card is present and can be initialized:
189       if (!SD.begin(SS))
```

```
190       {
191         Serial.println("#Card failed, or not present");
192         // don't do anything more:
193         return;
194       }
195
196       // open the file. note that only one file can be open at a time,
197       // so you have to close this one before opening another.
198       File dataFile = SD.open("datalog.txt", FILE_WRITE);
199
200       // if the file is available, write to it:
201       if (dataFile)
202       {
203         dataFile.println(dataString);  // write to SDcard (800 ms)
204         dataFile.close();
205
206         digitalWrite(LED_red, HIGH);  // Blink for Dasa
207         Serial.println(dataString);  // print SN to terminal
208         digitalWrite(LED_red, LOW);
209       }
210       // if the file isn't open, pop up an error:
211       else
212       {
213         Serial.println("#error opening datalog.txt");
214       }
215
216       DDRB = 0b10011110;
217       PORTB = 0b00000001;  // SDcard Power OFF
218     }
219
220     // measurement of ADC offset
221     ADMUX = (analog_reference << 6) | 0b10001; // Select +A1,-A1 for offset
    correction
222     delay(200);
223     ADCSRB = 0;               // Switching ADC to Free Running mode
224     sbi(ADCSRA, ADATE);       // ADC autotrigger enable (mandatory for free
    running mode)
225     sbi(ADCSRA, ADSC);        // ADC start the first conversions
226     sbi(ADCSRA, 2);           // 0x100 = clock divided by 16, 62.5 kHz, 208 us
    for 13 cycles of one AD conversion, 24 us fo 1.5 cycle for sample-hold
227     cbi(ADCSRA, 1);
228     cbi(ADCSRA, 0);
229     sbi(ADCSRA, ADIF);                  // reset interrupt flag from ADC
230     while (bit_is_clear(ADCSRA, ADIF)); // wait for the first conversion
231     sbi(ADCSRA, ADIF);                  // reset interrupt flag from ADC
232     lo = ADCL;
233     hi = ADCH;
234     ADMUX = (analog_reference << 6) | 0b10000; // Select +A0,-A1 for measurement
235     ADCSRB = 0;               // Switching ADC to Free Running mode
236     sbi(ADCSRA, ADATE);       // ADC autotrigger enable (mandatory for free
    running mode)
237     sbi(ADCSRA, ADSC);        // ADC start the first conversions
238     sbi(ADCSRA, 2);           // 0x100 = clock divided by 16, 62.5 kHz, 208 us
    for 13 cycles of one AD conversion, 24 us fo 1.5 cycle for sample-hold
239     cbi(ADCSRA, 1);
240     cbi(ADCSRA, 0);
241     // combine the two bytes
242     u_sensor = (hi << 7) | (lo >> 1);
243     // manage negative values
244     if (u_sensor <= (CHANNELS / 2) - 1 ) {
245       u_sensor += (CHANNELS / 2);
246     } else {
247       u_sensor -= (CHANNELS / 2);
248     }
249     base_offset = 256; //u_sensor;
250
```

```
251     // Initiates RTC
252     rtc.autoprobe();
253     rtc.resetClock();
254   }
255
256
257   void loop()
258   {
259     uint16_t histogram[CHANNELS];
260     uint32_t flux;
261
262     uint32_t flux_long = 0;
263
264     for(int i=0; i<(GPSdelay); i++)  // measurements between GPS aquisition
265     {
266       for(int n=0; n<CHANNELS; n++)
267       {
268         histogram[n]=0;
269       }
270
271       // measurement of ADC offset
272       ADMUX = (analog_reference << 6) | 0b10001; // Select +A1,-A1 for offset
      correction
273       delay(50);
274       ADCSRB = 0;               // Switching ADC to Free Running mode
275       sbi(ADCSRA, ADATE);       // ADC autotrigger enable (mandatory for free
      running mode)
276       sbi(ADCSRA, ADSC);        // ADC start the first conversions
277       sbi(ADCSRA, 2);           // 0x100 = clock divided by 16, 62.5 kHz, 208
      us for 13 cycles of one AD conversion, 24 us fo 1.5 cycle for sample-hold
278       cbi(ADCSRA, 1);
279       cbi(ADCSRA, 0);
280       sbi(ADCSRA, ADIF);                  // reset interrupt flag from ADC
281       while (bit_is_clear(ADCSRA, ADIF)); // wait for the first conversion
282       sbi(ADCSRA, ADIF);                  // reset interrupt flag from ADC
283       lo = ADCL;
284       hi = ADCH;
285       ADMUX = (analog_reference << 6) | 0b10000; // Select +A0,-A1 for
      measurement
286       ADCSRB = 0;               // Switching ADC to Free Running mode
287       sbi(ADCSRA, ADATE);       // ADC autotrigger enable (mandatory for free
      running mode)
288       sbi(ADCSRA, ADSC);        // ADC start the first conversions
289       sbi(ADCSRA, 2);           // 0x100 = clock divided by 16, 62.5 kHz, 208
      us for 13 cycles of one AD conversion, 24 us fo 1.5 cycle for sample-hold
290       cbi(ADCSRA, 1);
291       cbi(ADCSRA, 0);
292       // combine the two bytes
293       u_sensor = (hi << 7) | (lo >> 1);
294       // manage negative values
295       if (u_sensor <= (CHANNELS/2)-1 ) {u_sensor += (CHANNELS/2);} else
      {u_sensor -= (CHANNELS/2);}
296       offset = u_sensor;
297
298       PORTB = 1;                          // Set reset output for peak detector
      to H
299       sbi(ADCSRA, ADIF);                  // reset interrupt flag from ADC
300       while (bit_is_clear(ADCSRA, ADIF)); // wait for the first dummy
      conversion
301       DDRB = 0b10011111;                  // Reset peak detector
302       delayMicroseconds(100);             // guaranteed reset
303       DDRB = 0b10011110;
304
305       sbi(ADCSRA, ADIF);        // reset interrupt flag from ADC
306
307       uint16_t suppress = 0;
```

```
308
309       while (bit_is_clear(ADCSRA, ADIF)); // wait for dummy conversion
310       DDRB = 0b10011111;                  // Reset peak detector
311       asm("NOP");                         // cca 6 us for 2k2 resistor and 1k
      capacitor in peak detector
312       asm("NOP");
313       asm("NOP");
314       asm("NOP");
315       asm("NOP");
316       DDRB = 0b10011110;
317       sbi(ADCSRA, ADIF);                  // reset interrupt flag from ADC
318
319       // dosimeter integration
320       for (uint16_t i=0; i<46000; i++)    // cca 10 s
321       {
322         while (bit_is_clear(ADCSRA, ADIF)); // wait for end of conversion
323         //delayMicroseconds(24);            // 24 us wait for 1.5 cycle of 62.5
      kHz ADC clock for sample/hold for next conversion
324         asm("NOP");                         // cca 8 us after loop
325         asm("NOP");
326         asm("NOP");
327         asm("NOP");
328         asm("NOP");
329         asm("NOP");
330
331         DDRB = 0b10011111;                  // Reset peak detector
332         asm("NOP");                         // cca 7 us for 2k2 resistor and
      100n capacitor in peak detector
333         asm("NOP");
334         asm("NOP");
335         asm("NOP");
336         asm("NOP");
337         DDRB = 0b10011110;
338         sbi(ADCSRA, ADIF);                  // reset interrupt flag from ADC
339
340         // we have to read ADCL first; doing so locks both ADCL
341         // and ADCH until ADCH is read.  reading ADCL second would
342         // cause the results of each conversion to be discarded,
343         // as ADCL and ADCH would be locked when it completed.
344         lo = ADCL;
345         hi = ADCH;
346
347         // combine the two bytes
348         u_sensor = (hi << 7) | (lo >> 1);
349
350         // manage negative values
351         if (u_sensor <= (CHANNELS/2)-1 ) {u_sensor += (CHANNELS/2);} else
      {u_sensor -= (CHANNELS/2);}
352
353         if (u_sensor > maximum) // filter double detection for pulses between
      two samples
354         {
355           maximum = u_sensor;
356           suppress++;
357         }
358         else
359         {
360           histogram[maximum]++;
361           maximum = 0;
362         }
363       }
364
365       // Data out
366       flux = 0;
367       {
368         rtc.readClock(tm);
```

```
369         RTCx::time_t t = RTCx::mktime(&tm);
370
371         // make a string for assembling the data to log:
372         String dataString = "";
373
374         // make a string for assembling the data to log:
375         dataString += "$CANDY,";
376
377         dataString += String(count);
378         dataString += ",";
379
380         dataString += String(t-946684800);
381         dataString += ",";
382
383         uint16_t noise = base_offset+4; // first channel for flux calculation
384         #define RANGE 252
385
386         for(int n=base_offset; n<(base_offset+RANGE); n++)
387         {
388           dataString += String(histogram[n]);
389           //dataString += "\t";
390           dataString += ",";
391           //if (n==NOISE) dataString += "*,";
392         }
393
394         for(int n=noise; n<(base_offset+RANGE); n++)
395         {
396           flux += histogram[n];
397         }
398
399         dataString += String(suppress);
400         dataString += ",";
401         dataString += String(flux);
402         dataString += ",";
403         dataString += String(offset);
404
405         count++;
406
407         flux_long = flux_long + flux;
408
409        //if (flux > GPSthreshold)
410        {
411           DDRB = 0b10111110;
412           PORTB = 0b00001111;  // SDcard Power ON
413
414           // make sure that the default chip select pin is set to output
415           // see if the card is present and can be initialized:
416           if (!SD.begin(SS))
417           {
418             Serial.println("#Card failed, or not present");
419             // don't do anything more:
420             return;
421           }
422
423           // open the file. note that only one file can be open at a time,
424           // so you have to close this one before opening another.
425           File dataFile = SD.open("datalog.txt", FILE_WRITE);
426
427           // if the file is available, write to it:
428           if (dataFile)
429           {
430             //digitalWrite(LED_red, HIGH);  // Blink for Dasa
431             dataFile.println(dataString);  // write to SDcard (800 ms)
432             //digitalWrite(LED_red, LOW);
433             dataFile.close();
434           }
```

```
435           // if the file isn't open, pop up an error:
436           else
437           {
438             Serial.println("#error opening datalog.txt");
439           }
440 
441           DDRB = 0b10011110;
442           PORTB = 0b00000001;  // SDcard Power OFF
443         }
444 
445   #ifdef DEBUG
446   #else
447         dataString.remove(75);
448   #endif
449 
450         digitalWrite(LED_red, HIGH);  // Blink for Dasa
451         Serial.println(dataString);   // print to terminal (additional 700 ms
      in DEBUG mode)
452         digitalWrite(LED_red, LOW);
453       }
454     }
455 
456     // GPS **********************
457     if (flux_long > GPSthreshold)
458   //  if (false)
459     {
460         // make a string for assembling the data to log:
461         String dataString = "";
462 
463   #define MSG_NO 10    // number of logged NMEA messages
464 
465       digitalWrite(GPSpower, HIGH); // GPS Power ON
466       delay(100);
467       {
468         // Switch off Galileo and GLONASS; UBX-CFG-GNSS (6)+4+8*7+(2)=68
      configuration bytes
469         const char cmd[68]={0xB5, 0x62, 0x06, 0x3E, 0x3C, 0x00, 0x00, 0x20,
      0x20, 0x07, 0x00, 0x08, 0x10, 0x00, 0x01, 0x00, 0x01, 0x01, 0x01, 0x01, 0x03,
      0x00, 0x01, 0x00, 0x01, 0x01, 0x02, 0x04, 0x08, 0x00, 0x00, 0x00, 0x01, 0x01,
      0x03, 0x08, 0x10, 0x00, 0x00, 0x00, 0x01, 0x01, 0x04, 0x00, 0x08, 0x00, 0x00,
      0x00, 0x01, 0x03, 0x05, 0x00, 0x03, 0x00, 0x00, 0x00, 0x01, 0x05, 0x06, 0x08,
      0x0E, 0x00, 0x00, 0x00, 0x01, 0x01, 0x53, 0x1F};
470         for (int n=0;n<(68);n++) Serial1.write(cmd[n]);
471       }
472       {
473         // airborne <2g; UBX-CFG-NAV5 (6)+36+(2)=44 configuration bytes
474         const char cmd[44]={0xB5, 0x62 ,0x06 ,0x24 ,0x24 ,0x00 ,0xFF ,0xFF ,
      0x07 ,0x03 ,0x00 ,0x00 ,0x00 ,0x00 ,0x10 ,0x27 , 0x00 ,0x00 ,0x05 ,0x00 ,
      0xFA ,0x00 ,0xFA ,0x00 ,0x64 ,0x00 ,0x5E ,0x01 ,0x00 ,0x3C ,0x00 ,0x00 ,
      0x00 ,0x00 ,0x00 ,0x00 ,0x00 ,0x00 ,0x00 ,0x00 ,0x00 ,0x00 ,0x85 ,0x2A};
475         for (int n=0;n<(44);n++) Serial1.write(cmd[n]);
476       }
477       {
478         // switch to UTC time; UBX-CFG-RATE (6)+6+(2)=14 configuration bytes
479         const char cmd[14]={0xB5 ,0x62 ,0x06 ,0x08 ,0x06 ,0x00 ,0xE8 ,0x03 ,
      0x01 ,0x00 ,0x00 ,0x00 ,0x00 ,0x37};
480         for (int n=0;n<(14);n++) Serial1.write(cmd[n]);
481       }
482       // flush serial buffer
483       while (Serial1.available()) Serial1.read();
484 
485       boolean flag = false;
486       char incomingByte;
487       int messages = 0;
488       uint32_t nomessages = 0;
489 
```

```
490       while(true)
491       {
492         if (Serial1.available())
493         {
494           // read the incoming byte:
495           incomingByte = Serial1.read();
496           nomessages = 0;
497 
498           if (incomingByte == '$') {messages++;}; // Prevent endless waiting
499           if (messages > 300) break; // more than 26 s
500 
501           if (flag && (incomingByte == '*')) break;
502           flag = false;
503 
504           if (incomingByte == 'A') flag = true;   // Waiting for FIX
505         }
506         else
507         {
508           nomessages++;
509           if (nomessages > GPSerror) break; // preventing of forever waiting
510         }
511       }
512 
513       // make a string for assembling the NMEA to log:
514       dataString = "";
515 
516       flag = false;
517       messages = 0;
518       nomessages = 0;
519       while(true)
520       {
521         if (Serial1.available())
522         {
523           // read the incoming byte:
524           incomingByte = Serial1.read();
525           nomessages = 0;
526 
527           if (incomingByte == '$') {flag = true; messages++;};
528           if (messages > MSG_NO)
529           {
530             rtc.readClock(tm);
531             RTCx::time_t t = RTCx::mktime(&tm);
532 
533             dataString += "$TIME,";
534             dataString += String(t-946684800);  // RTC Time of the last GPS
    NMEA Message
535 
536             break;
537           }
538 
539           // say what you got:
540           if (flag && (messages<=MSG_NO)) dataString+=incomingByte;
541         }
542         else
543         {
544           nomessages++;
545           if (nomessages > GPSerror) break; // preventing of forever waiting
546         }
547       }
548       digitalWrite(GPSpower, LOW); // GPS Power OFF
549 
550       {
551           DDRB = 0b10111110;
552           PORTB = 0b00001111;  // SDcard Power ON
553 
554           // make sure that the default chip select pin is set to output
```

```
555           // see if the card is present and can be initialized:
556           if (!SD.begin(SS))
557           {
558             Serial.println("#Card failed, or not present");
559             // don't do anything more:
560             return;
561           }
562 
563           // open the file. note that only one file can be open at a time,
564           // so you have to close this one before opening another.
565           File dataFile = SD.open("datalog.txt", FILE_WRITE);
566 
567           // if the file is available, write to it:
568           if (dataFile)
569           {
570             digitalWrite(LED_red, HIGH);  // Blink for Dasa
571             dataFile.println(dataString);  // write to SDcard (800 ms)
572             digitalWrite(LED_red, LOW);
573             dataFile.close();
574           }
575           // if the file isn't open, pop up an error:
576           else
577           {
578             Serial.println("#error opening datalog.txt");
579           }
580 
581           DDRB = 0b10011110;
582           PORTB = 0b00000001;  // SDcard Power OFF
583       }
584   #ifdef DEBUG
585       Serial.println(dataString);  // print to terminal (additional 700 ms)
586   #endif
587     }
588   }
```

Attachment F

AIRDOS G data processing

In [3]:

```
import pandas as pd
import numpy as np
from datetime import datetime, timedelta
from IPython.display import Image as ImageDisp
from pandas import DataFrame
import string
import os
import glob
import matplotlib.pyplot as plt
import glob
```

In [4]:

```
%pylab inline --no-import-all
```

```
Populating the interactive namespace from numpy and matplotlib
```

Read Logfile

In [22]:

```
#fto = './data/malaga/16/DATALOG.TXT' #  File to Open
fto = './data/malaga/21/DATALOG.TXT' #  File to Open
#fto = './data/malaga/98/DATALOG.TXT' #  File to Open
#fto = './data/malaga/F0/DATALOG.TXT' #  File to Open

print (fto)

l=[]
l.extend(range(0,258))
df = pd.read_table(fto, sep=',', header=None, names=l, comment='*',engine='pytho
n' )

df.drop(df[df[0]=='$STROKE'].index, inplace=True)
df.drop(df[df[0]=='$GPTXT'].index, inplace=True)
#df.drop(r[r[0]=='$GPRMC'].index, inplace=True)
df.drop(df[df[0]=='$GPVTG'].index, inplace=True)
df.drop(df[df[0]=='$GPGLL'].index, inplace=True)
df.drop(df[df[0]=='$GPGSA'].index, inplace=True)
df.drop(df[df[0]=='$GPGSV'].index, inplace=True)
#df.drop(df[df[0]=='$CANDY'].index, inplace=True)

sn = df.loc[df[0]=='$AIRDOS'][3]
print (sn[0])
```

```
./data/malaga/21/DATALOG.TXT
1290c00806a200912457a000a0000021
```

Derive measurement runs in to separate files

In [19]:

```
run = 0

runs = []
LatDD = np.nan
LatD = np.nan
LatM = np.nan
LonDD = np.nan
LonD = np.nan
LonM = np.nan
LatHem = ''
LonHem = ''

for i,r in df.iterrows():
    if (r[0] == '$AIRDOS'):
        run = run + 1
        date = np.nan #pd.to_datetime('210317000000.00', format='%d%m%y%H%M%S.%
f')
        time = 0
        timedelta = 0
        altitude = np.nan
        Lat = np.nan
        Lon = np.nan
        speed = np.nan
        flag = 0
        flagrun = 0
        print (run, end='')

    if (r[0] == '$GPRMC'):
        date = pd.to_datetime(str(r[9])+str(r[1]), format='%d%m%y%H%M%S.%f',erro
rs='coerce')
        timedelta = time
        speed = r[7]
        LatHem = r.astype(str)[4]
        LonHem = r.astype(str)[6]
        if (LatHem=='S'):     # Conferr DDMM.MM to DD.DD
            LatS = -1
        else:
            LatS = 1
        if (LonHem=='W'):
            LonS = -1
        else:
            LonS = 1
        Lat = float(r[3])
        LatD = np.trunc(Lat/100)
        LatM = ((Lat/100) - LatD) * 100
        LatDD = LatD + LatM/60.0
        LatDD = LatDD * LatS
        Lon = float(r[5])
        LonD = np.trunc(Lon/100)
        LonM = ((Lon/100) - LonD) * 100
        LonDD = LonD + LonM/60.0
        LonDD = LonDD * LonS
        flag = 1

    if (r[0] == '$GPGGA'):
        altitude = r[9]

    df.at[i,'date'] = date
    df.at[i,'altitude'] = altitude
```

```
    df.at[i,'speed'] = speed

    if (r[0] == '$CANDY'):
        time = pd.to_numeric(r[2])  # read seconds from power on
        if (flag == 1):
            timedelta = time
            if (flagrun == 0):
                runs.append([run,date,timedelta])
                flagrun = 1
            flag = 0
        date_line = date + pd.to_timedelta(time - timedelta, unit='s')
        df.at[i,'date'] = date_line
        df.at[i,'run'] = run
        df.at[i,'lat'] = LatDD
        df.at[i,'lon'] = LonDD
        df.at[i,'latD'] = LatD
        df.at[i,'lonD'] = LonD
        df.at[i,'latM'] = LatM
        df.at[i,'lonM'] = LonM
        df.at[i,'latHem'] = LatHem
        df.at[i,'lonHem'] = LonHem


FROM = pd.to_datetime('2019-11-27 00:00:00')
TO = pd.to_datetime('2019-11-29 01:10:00')
#FROM = pd.to_datetime('2019-11-28 18:55:00')
#TO = pd.to_datetime('2019-11-29 01:00:00')
#PRG-AGP
#FROM = pd.to_datetime('2019-11-28 18:55:00')
#TO = pd.to_datetime('2019-11-28 20:55:00')
#AGP-PRG
#FROM = pd.to_datetime('2019-11-28 23:00:00')
#TO = pd.to_datetime('2019-11-29 00:30:00')


dfo = df.copy()
dfo = dfo.loc[(dfo['date']>FROM)&(dfo['date']<TO)]

#01/2002, FL-27
#DEG MIN N/S DEG MIN E/W FEET TIME(MIN)
dfdeg = df[['latD','latM','latHem','lonD','lonM','lonHem','altitude','run','dat
e']].copy()
dfdeg['altitude'] *= 3.28084
dfdeg['minute'] = 0
dfo['minute'] = 0
dfdeg = dfdeg.loc[(dfdeg['date']>FROM)&(dfdeg['date']<TO)]
#dfdeg.reset_index(inplace=True)

dfo.drop(dfo[dfo[0]=='$GPRMC'].index, inplace=True)
dfo.drop(dfo[dfo[0]=='$GPGGA'].index, inplace=True)
dfo.drop(dfo[dfo[0]=='$AIRDOS'].index, inplace=True)
dfdeg.drop(dfo[dfo[0]=='$GPRMC'].index, inplace=True)
dfdeg.drop(dfo[dfo[0]=='$GPGGA'].index, inplace=True)
dfdeg.drop(dfo[dfo[0]=='$AIRDOS'].index, inplace=True)

print ()

for f in glob.iglob("./output/*.csv"): # delete all output files
    print ('Deleting', f)
    os.remove(f)
```

```
dfo.set_index('date', inplace = True)

#01/2002, FL-27
#DEG MIN N/S DEG MIN E/W FEET TIME(MIN)

for x in runs:
    filename = './output/' + str(x[1] + pd.to_timedelta(-x[2], unit='s')) + '_'
+ str(sn[0])

    # Disimetric values
    dfo.loc[dfo['run'] == x[0],'minute'] = (pd.to_timedelta(dfo.loc[dfo['run'] =
= x[0]].index-(x[1] + pd.to_timedelta(-x[2], unit='s')))).astype('timedelta64
[m]').fillna(0).astype(int)
    dfo.loc[dfo['run'] == x[0]].to_csv(filename + '.csv')

    # zeroing minutes for CARI
    zerominutes = np.round((pd.to_timedelta(dfdeg.iloc[0,8]-(x[1] + pd.to_timede
lta(-x[2], unit='s')))).total_seconds()/60,0)

    # Telemetry for CARI 7
    with open(filename + '.DEG', 'w') as f:
        f.write('01/2002, FL-27\r\n')
        f.write('DEG MIN N/S DEG MIN E/W FEET TIME(MIN)\r\n')
    with open('ble.DEG', 'w') as f:
        f.write('11/2019, FL-27\r\n')
        f.write('DEG MIN N/S DEG MIN E/W FEET TIME(MIN)\r\n')
    #dfdeg.loc[dfdeg['run'] == x[0],'minute'] = (pd.to_timedelta(-dfdeg.iloc[0,
8]+dfdeg['date']-(x[1] + pd.to_timedelta(-x[2], unit='s')))).astype('timedelta64
[m]').fillna(0).astype(int)-119
    dfdeg.loc[dfdeg['run'] == x[0],'minute'] = (pd.to_timedelta(dfdeg['date']-(x
[1] + pd.to_timedelta(-x[2], unit='s')))).astype('timedelta64[m]').fillna(0).ast
ype(int)-zerominutes
    dfdeg.loc[dfdeg['run'] == x[0],['latD','latM', 'latHem', 'lonD', 'lonM', 'lo
nHem', 'altitude', 'minute']].dropna().drop_duplicates(subset='minute', keep='fi
rst').to_csv('ble.DEG', mode='a', index=False, header=False, line_terminator='\r
\n')

print('End')
```

```
1
Deleting ./output/2019-11-28 16:55:11_1290c00806a20091702fa000a00000
16.csv
End
```

In [15]:

```
matplotlib.rcParams.update({'font.size': 15})

NOISE_LEVEL= 8
LAST_CHANNEL=254
WINDOW = 20

for f in glob.iglob("./output/*.csv"): # generator, search immediate subdirector
ies
    plt.figure(figsize=(15,5))
    plt.tight_layout()
    xx = pd.read_csv(f)
    xx['date'] = pd.to_datetime(xx['date'])
    #xx.set_index('date', inplace = True)
    #xx = xx.loc['2019-11-27 00:00:00':'2019-11-29 01:30:00']

    s = f.split('/')
    plt.title(s[len(s)-1] + ' (rolling mean ' + str(WINDOW) + ')')

    # Deposited energy
    e = pd.DataFrame()
    e['Ch']=range(0,256)
    e['ener'] = e.index * 0.038 + 0.105
    xx['ener'] = (np.asarray(xx.iloc[:,8:256]) * np.asarray(e.loc[3:250,'ener'
])).sum(axis=1)


    # size of the chip (20 mm · 10 mm),
    # the thickness of the depletion layer (0.3 mm),
    # and the density of silicon (2.33 g cm^3)
    # 0.1398e-3 kg
    xx['dsi'] = ((1e6 * (1.602e-19 * xx['ener'] * 1e6)/0.1398e-3)/10.4) * 3600 *
2.71 # in uGy/h

    xx['flux'] = xx.iloc[:,range(NOISE_LEVEL,LAST_CHANNEL)].sum(axis=1)

    xx['fluxmean'] = xx['flux'].rolling(WINDOW).mean()
    xx['dsimean'] = xx['dsi'].rolling(WINDOW).mean()

    #plt.plot(xx['minute'], xx['flux'], c='gray', linestyle='', marker='.')
    plt.plot(xx['minute'], xx['dsi'], c='gray', linestyle='', marker='.', label=
'AIRDOS')
    plt.plot(xx['minute'],xx['dsimean'],c='red', drawstyle='steps-mid', label='A
IRDOS avg')
    #plt.plot(xx.iloc[:,'minute'],xx['fluxmean']c='red')
    #plt.plot(xx.loc[:,'minute'],xx.iloc[:,NOISE_LEVEL],c='tan',label= str(NOISE
_LEVEL) + '. Ch' ,zorder=1)

    # CARI 7
    f = './data/ble.DAT' #  File to Open
    df = pd.read_csv(f, engine='python', header=None, delim_whitespace=True, ski
prows=2, skipfooter=3 )
    plt.plot(df.loc[(df[3]>95)&(df[4]>2),3],df.loc[(df[3]>95)&(df[4]>2),4], c='b
lue', markersize=7, marker='.', linestyle='none', label='CARI 7')

    plt.ylim([0,10])
    #plt.yscale('log')

    plt.xlabel('Time [minutes]')
    plt.ylabel(r'dH*(10)/dt or dE/dt [$\mu$Sv/h]', color='red')
```

```
    plt.legend(loc=2)

    '''
    ax = plt.twinx()

    plt.ylim([0,14000])
    plt.plot(xx['minute'], xx['altitude'], c='b', label='alt', marker='.', linew
idth='2', linestyle='none', drawstyle='steps-mid')
    plt.ylabel('altitude a.s.l. [m]', color='blue')
    '''
    plt.grid(b=True, which='major', color='grey', linestyle='-')
    plt.grid(b=True, which='minor', color='grey', linestyle='-')
    plt.legend()
```

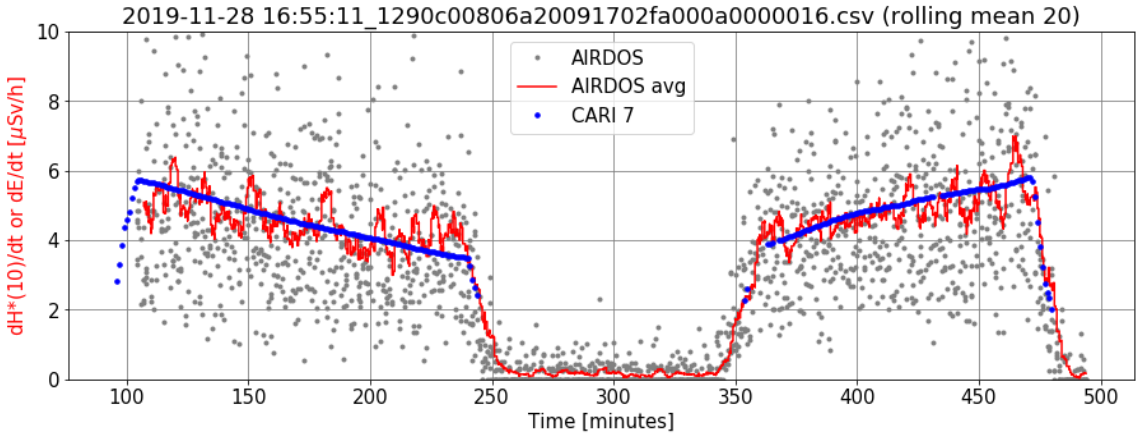

Plot Flux

In [20]:

```
matplotlib.rcParams.update({'font.size': 15})

NOISE_LEVEL= 8
LAST_CHANNEL=254
WINDOW = 10

for f in glob.iglob("./output/*.csv"): # generator, search immediate subdirector
ies
    try:
        plt.figure(figsize=(15,5))
        plt.tight_layout()
        xx = pd.read_csv(f)
        xx['date'] = pd.to_datetime(xx['date'])
        xx.set_index('date', inplace = True)
        #xx = xx.loc['2019-11-27 00:00:00':'2019-11-29 01:30:00']


        xx['flux'] = xx.iloc[:,range(NOISE_LEVEL,LAST_CHANNEL)].sum(axis=1)

        xx['fluxmean'] = xx['flux'].rolling(WINDOW).mean()

        xx['flux'].plot(c='gray', linestyle='', marker='.')
        xx['fluxmean'].plot(c='red')
        xx.iloc[:,NOISE_LEVEL].plot(c='tan',label= str(NOISE_LEVEL) + '. Ch' ,zo
rder=1)

        s = f.split('/')
        plt.title(s[len(s)-1] + ' (rolling mean ' + str(WINDOW) + ')')
        #plt.ylim([0,20])
        plt.xlabel('UT')
        plt.ylabel('Counts per 10 seconds [-]', color='red')
        plt.legend(loc=2)

        ax = plt.twinx()

        plt.ylim([0,14000])
        xx['altitude'].plot(c='b', label='alt', marker='.', linewidth='2', lines
tyle='none', drawstyle='steps-mid')
        plt.ylabel('altitude a.s.l. [m]', color='blue')

        plt.grid(b=True, which='major', color='grey', linestyle='-')
        plt.grid(b=True, which='minor', color='grey', linestyle='-')
        plt.legend()
    except:
        pass
```

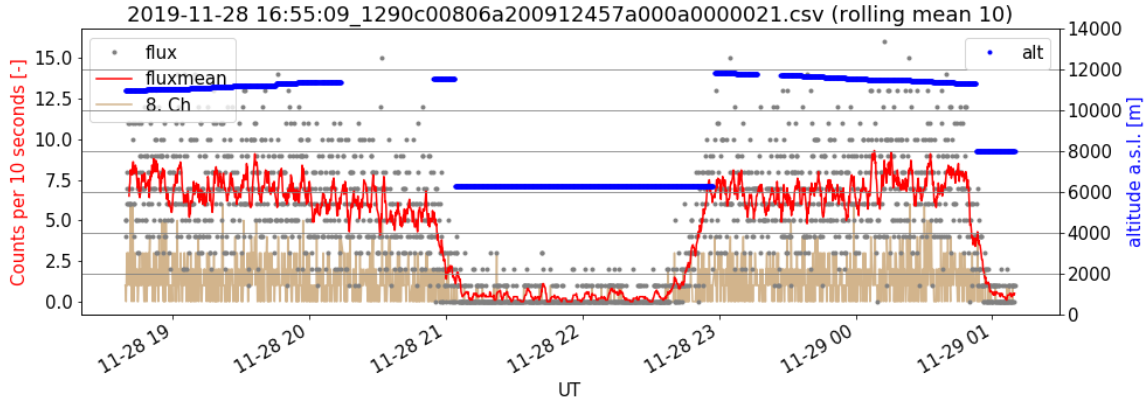

CARI 7

In [717]:

```
f = './ble.DAT' #  File to Open
df = pd.read_csv(f, engine='python', header=None, delim_whitespace=True, skiprow
s=2, skipfooter=3 )
```

In [718]:

```
plt.plot(df[3],df[4], c='red')
plt.twinx()
plt.plot(df[3],df[2], c='blue')
```

Out[718]:

```
[<matplotlib.lines.Line2D at 0x7f52296488d0>]
```

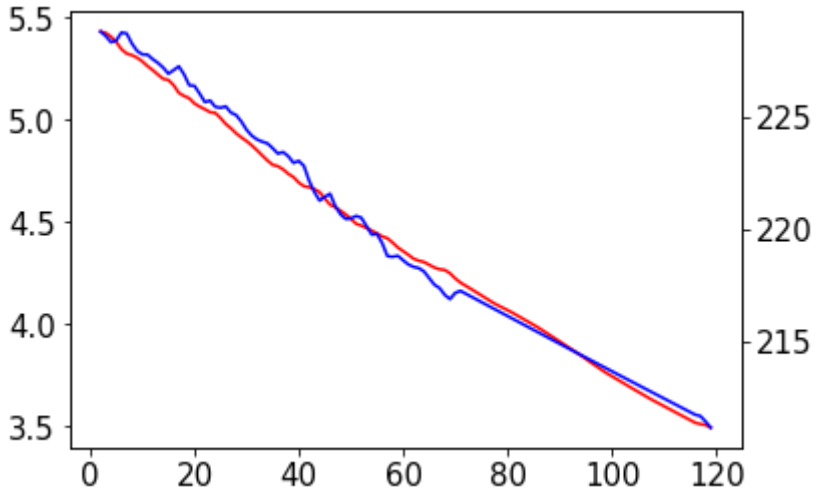

Plot Energy Spectra

In [8]:

```
FROM_ENERGY = 0.2
TO_ENERGY = 9.0

l = np.array([[29+4, 1],[208+4,1]]) # Calibration
r = np.array([1.23, 8.122])
coef = np.linalg.solve(l,r)
print (coef[0], coef[1])

# force calibration coeficients
#coef[0]=0.038
#coef[1]=0.105

for f in glob.iglob("./output/*.csv"): # generator, search immediate subdirectories
    try:
        LOW_ENERGY = 5

        df = pd.read_csv(f)
        df['date'] = pd.to_datetime(df['date'])
        df.set_index('date', inplace = True)

        # Uncomment this if you are interested in a specific time interval
        #xx = df.loc['2019-01-24 05:00:00':'2019-01-24 13:00:00']
        xx = df
        ener1 = xx.iloc[:,LOW_ENERGY:255].sum()
        e = pd.DataFrame()
        e['1'] = ener1
        e['index'] = pd.to_numeric(ener1.index)
        e['x'] = (e['index']) * coef[0] + coef[1]
        e['deposit'] = e['1'] * e['x']
        depener = e.loc[(e['x']>=FROM_ENERGY)&(e['x']<=TO_ENERGY),'deposit'].sum() # MeV

        dose = 1e6*(1.602e-19 * depener*1e6)/0.1398e-3

        # size of the chip (20 mm · 10 mm),
        # the thickness of the depletion layer (0.3 mm),
        # and the density of silicon (2.33 g cm^3)
        # 0.1398e-3 kg
        #dose = ((1e6 * (1.602e-19 * depener * 1e6)/0.1398e-3)/10.4) * 3600 * 2.71 # in uGy/h


        if (depener > 0):
            plt.figure(figsize=(15,8))
            plt.tight_layout()
            s = f.split('/')
            plt.title(s[len(s)-1])
            plt.yscale('log')
            #plt.ylim([0.9,1e8])

            plt.plot(e['x'],e['1'], c='r', lw=3, drawstyle='steps-post', label='AIRDOS')

            plt.text(6, 50000, r'$\epsilon$ = ' + str(round(depener*1.1,1)) + ' [MeV]', fontsize=18, color='r')
            plt.text(6, 13000, r'D$_S$$_i$ = ' + str(round(dose*1.1*2.71,2)) + r' [$\mu$Gy] / (' + str(FROM_ENERGY) + ',' + str(TO_ENERGY) + ') [MeV]', fontsize=18, color='r')
```

```
            plt.legend()
            plt.xlabel('Energy [MeV]')
            plt.ylabel('Counts [-]')
            plt.grid()
    except:
        pass
```

```
0.03850279329608939 -0.040592178770949686
```

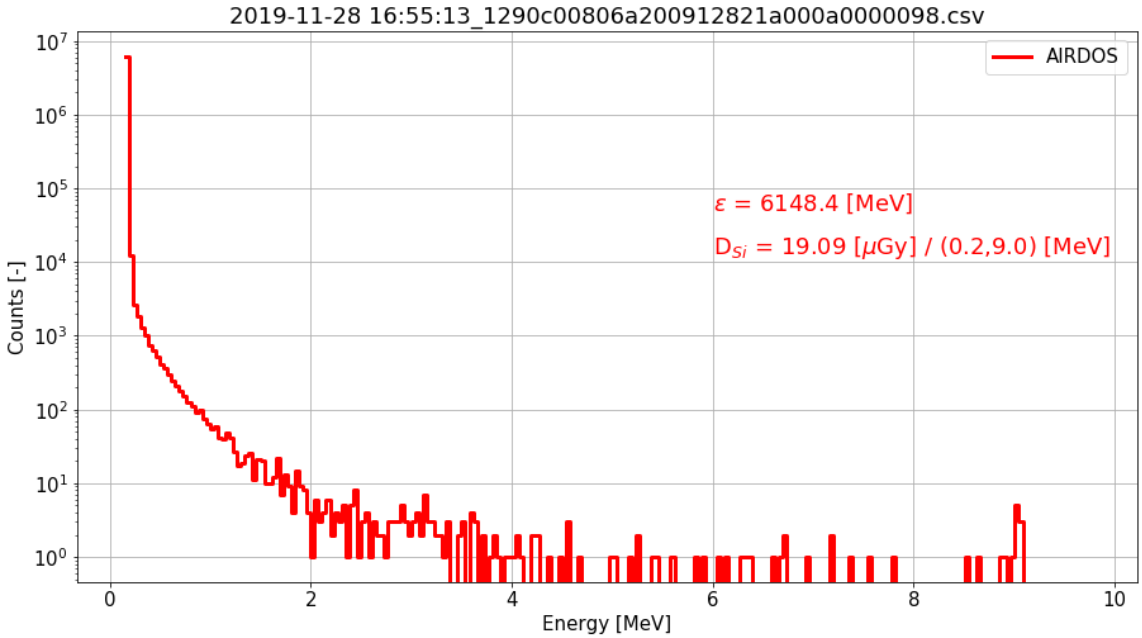

Plot Map

In [7]:

```
import time, calendar, datetime, numpy
from mpl_toolkits.basemap import Basemap
import matplotlib.pyplot as plt
import urllib, os

NOISE_LEVEL= 7
LAST_CHANNEL=254
WINDOW = 10

for f in glob.iglob("./output/*.csv"): # generator, search immediate subdirectories
    try:
        plt.figure(figsize=(15,5))
        plt.tight_layout()
        df6 = pd.read_csv(f)
        df6.dropna(inplace=True)
        df6['lat'] = pd.to_numeric(df6['lat'])
        df6['lon'] = pd.to_numeric(df6['lon'])
        df6['altitude'] = pd.to_numeric(df6['altitude'])

        plt.figure(figsize=(15,15))
        matplotlib.rcParams.update({'font.size': 15})

        # create Basemap instance.
        #m = Basemap(projection='kav7',lon_0=0)
        #m = Basemap(projection='cea',lon_0=0)
        m = Basemap(projection='robin',lon_0=0)
        #m = Basemap(llcrnrlon=-180,llcrnrlat=-80,urcrnrlon=180,urcrnrlat=85,projection='mill')

        x, y = m(df6.lon.tolist(),df6.lat.tolist())
        m.drawmapboundary(fill_color='#99ffff')
        m.fillcontinents(color='#cc9966',lake_color='#99ffff',zorder=0)
        # draw parallels and meridians, but don't bother labelling them.
        m.drawparallels(np.arange(-90.,99.,30.),labels=[1,1,0,0])
        m.drawmeridians(np.arange(-180.,180.,60.),labels=[0,0,1,0])

        im1 = m.scatter(x,y,c=df6.altitude.tolist(),marker='o', cmap='jet')
        cb = m.colorbar(im1,"bottom", size="5%", pad="2%")
        cb.set_label('m a.s.l.')

        s = f.split('/')
        plt.title(s[len(s)-1], pad=50)

        plt.clim(0, 12500)  # limit for color axis
        plt.show()
    except:
        pass
```

<Figure size 1080x360 with 0 Axes>

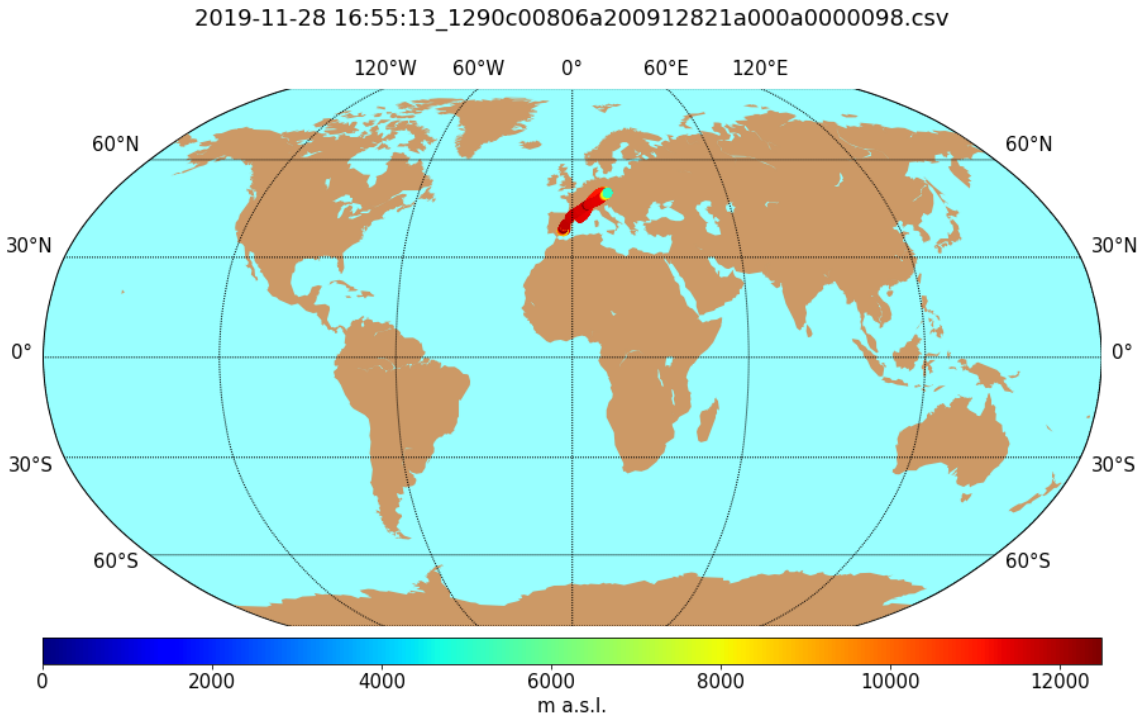

In [21]:

```
import time, calendar, datetime, numpy
from mpl_toolkits.basemap import Basemap
import matplotlib.pyplot as plt
import urllib, os

NOISE_LEVEL= 7
LAST_CHANNEL=254
WINDOW = 10

for f in glob.iglob("./output/*.csv"): # generator, search immediate subdirectories
    try:
        plt.figure(figsize=(15,5))
        plt.tight_layout()
        df6 = pd.read_csv(f)
        df6.dropna(inplace=True)
        df6['lat'] = pd.to_numeric(df6['lat'])
        df6['lon'] = pd.to_numeric(df6['lon'])
        df6['altitude'] = pd.to_numeric(df6['altitude'])

        plt.figure(figsize=(15,15))
        matplotlib.rcParams.update({'font.size': 15})

        # create Basemap instance.
        #m = Basemap(projection='kav7',lon_0=0)
        #m = Basemap(projection='cea',lon_0=0)
        #m = Basemap(projection='robin',lon_0=0)
        #m = Basemap(llcrnrlon=-180,llcrnrlat=-80,urcrnrlon=180,urcrnrlat=85,projection='mill')
        m = Basemap(projection='cyl',lon_0=0, llcrnrlon=-11,llcrnrlat=30,urcrnrlon=18,urcrnrlat=52)

        x, y = m(df6.lon.tolist(),df6.lat.tolist())
        #m.drawmapboundary(fill_color='#99ffff')
        m.fillcontinents(color='#cc9966',lake_color='#99ffff',zorder=0)
        # draw parallels and meridians, but don't bother labelling them.
        m.drawparallels(np.arange(-90.,99.,10.),labels=[1,1,0,0])
        m.drawmeridians(np.arange(-180.,180.,10.),labels=[0,0,1,0])
        m.shadedrelief()

        m.plot(x,y, zorder=2, color='gray', lw=5)
        im1 = m.scatter(x,y,c=df6.altitude.tolist(),marker='o', cmap='jet', zorder=99)

        cb = m.colorbar(im1,"bottom", size="5%", pad="2%")
        cb.set_label('Altitude above sea level [m]')

        s = f.split('/')
        plt.title(s[len(s)-1], pad=50)

        plt.clim(0, 12500)  # limit for color axis
        plt.show()
    except:
        pass
```

<Figure size 1080x360 with 0 Axes>